

# APPLICATION OF DIC IN SOLID MECHANICS

Vishwajeet S. Bhise

A Dissertation Submitted to  
Indian Institute of Technology Hyderabad  
In Partial Fulfillment of the Requirements for  
The Degree of Master of Technology



भारतीय प्रौद्योगिकी संस्थान हैदराबाद  
Indian Institute of Technology Hyderabad

Department of Mechanical Engineering

July, 2013

## Declaration

I declare that this written submission represents my ideas in my own words, and where others' ideas or words have been included, I have adequately cited and referenced the original sources. I also declare that I have adhered to all principles of academic honesty and integrity and have not misrepresented or fabricated or falsified any idea/data/fact/source in my submission. I understand that any violation of the above will be a cause for disciplinary action by the Institute and can also evoke penal action from the sources that have thus not been properly cited, or from whom proper permission has not been taken when needed.



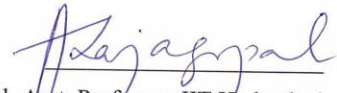
---

Vishwajeet S. Bhise

ME11M03

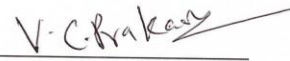
## Approval Sheet

This thesis entitled APPLICATION OF DIC IN SOLID MECHANICS by Vishwajeet S. Bhise is approved for the degree of Master of Technology from IIT Hyderabad.



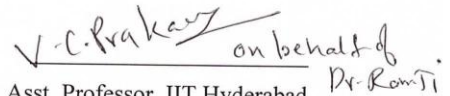
Dr. Amirtham Rajagopal, Asst. Professor, IIT Hyderabad

Examiner



Dr. Chandrika Prakash Vyasarayani, Asst. Professor, IIT Hyderabad

Examiner



Dr. M. Ramji, Asst. Professor, IIT Hyderabad

Adviser

Dr. Mahendrakumar Madhavan, Asst. Professor, IIT Hyderabad

Chairman

## **Acknowledgements**

I am indebted to a number of people for their help, knowledge and support throughout this entire process. First I would like to thank my thesis advisor Dr. M. Ramji for his excellent guidance, consistent encouragement and inspiration and motivation throughout my work. I wish to express a deep sense of gratitude towards him.

I would like to acknowledge Mr. RGR Prasath (Guru Sir) for his constant support and many useful suggestions regarding experimentation. I would like to thank Ph. D scholar Mr. Mohammad Kashfuddoja for his help and suggestions regarding the finite element analysis and composite fabrication. I am very thankful to my friends at engineering optics lab, Jabir, Naresh and Pratap for their cooperation in my experimental work. I am also thankful to Mr. K. Sathyanarayana, Project Engineer In-charge, Central Workshop for his encouragement. I would also like to thank Mr. A. Praveen Kumar, Mr. S. Jagadeesan and all the other staff of Central Workshop for their cooperation in specimen preparation.

I am very thankful to all my friends in IIT Hyderabad for their help and support during the completion of my post-graduation.

I am obliged to my parents, Sh. Shivajirao Bhise and Smt. Alka Bhise for their blessings, love and support. I will not forget to say thanks a lot to my sister, Vishwanjali and brother, Indrajit for their faith and believe in me. I would like to say special thanks to several peoples, who have knowingly unknowingly helped me in the completion of this work.

*Dedicated to*

*My Parents*

## **Abstract**

During service life, composite structures are susceptible to damage which reduces their structural integrity. For improved service life, the damage needs to be repaired. In case of low velocity impact damage adhesively bonded patch repair has shown to be cost effective and most efficient in extending service life of damaged parts. The repair performance is mainly influenced by patch stacking sequence, patch shape, patch thickness, overlap length and adhesive strength. In the first phase of work, a 3D finite element based study is carried out using mechanics based approach to optimize the patch dimensions and stacking sequence so that the performance of repaired structure can be improved. Also, a genetic algorithm based approach in-conjunction with finite element analysis is implemented for arriving at an optimized patch and adhesive dimensions. Experimental study is then carried out with optimized geometry using non-contact optical based technique namely digital image correlation (DIC). The mechanics of double and single sided repair are discussed in detail and strain field from DIC have been compared with finite element (FE) estimates.

In the second phase of work, a numerical based study is carried out to simulate debonding of inclusions from the surrounding matrix in the presence of a matrix crack. The single edge notched (SEN) panel, edge slant cracked (ESC) panel having a circular inclusion ahead of the crack and single edge cracked panel with two eccentrically positioned circular inclusions ahead of the crack subjected to tensile load is being studied in the present work. An element stiffness degradation method in-conjunction with maximum radial stress criteria is used in numerical study to investigate the effect of debonding on SIF. The finite element model is initially validated using results obtained from whole field experimental technique namely digital image correlation (DIC). The effects of parameters such as the inclusion diameter, distance between the crack tip and edge of the inclusion and Young's modulus ratio between the inclusion and the matrix on the SIF are studied. The experimentally obtained results are compared with finite element (FE) estimates and they are found to be in good agreement.

## Nomenclature

SCF	Stress Concentration Factor
SIF	Stress Intensity Factor
FEA	Finite Element Analysis
DIC	Digital Image Correlation
$u, u_x$	Horizontal component of displacement
$v, u_y$	Vertical component of displacement
$J$	$J$ -integral value

# Contents

Declaration.....	ii
Approval Sheet .....	<b>Error! Bookmark not defined.</b>
Acknowledgements.....	iv
Abstract.....	vi
Nomenclature.....	vii
List of Figures.....	1
List of Tables .....	5
<b>1 Introduction and Literature Review .....</b>	<b>6</b>
1.1 Introduction .....	6
1.1.1 Composite material: an overview .....	6
1.1.2 Repair study on damaged CFRP laminates .....	7
1.1.3 Crack inclusion interaction study .....	10
1.2 Literature review.....	10
1.2.1 Repair study on damaged CFRP laminates .....	10
1.2.2 Crack inclusion interaction study .....	12
1.3 Experimental study involving DIC .....	15
1.4 Scope and motivation .....	15
1.5 Thesis layout.....	17
<b>2 Optimization of Composite Patch .....</b>	<b>18</b>
2.1 Introduction .....	18
2.2 Problem description.....	18
2.3 Numerical Study .....	20
2.3.1 Finite element modeling of circular cutout panel .....	20
2.3.2 Finite element modeling of circular patched panel.....	20
2.4 Patch design study .....	21
2.4.1 Mechanics based design approach.....	21
2.4.2 Optimization using GA based approach.....	22
2.5 Experimental Study .....	24
2.5.1 Specimen fabrication .....	24
2.5.2 Experimental setup and procedure .....	25
2.6 Results and Discussion .....	26
2.6.1 Numerical results.....	26
2.6.2 Experimental results .....	36



2.6.3 Comparison of whole field strain obtained from DIC and FEA.....	39
2.7 Closure.....	43
<b>3 Study of Matrix Crack Interaction on Inclusion Using DIC and FEA.....</b>	<b>44</b>
3.1 Introduction .....	44
3.2 Problem description .....	46
3.3 Multi-parameter displacement field equations .....	47
3.4 Over-deterministic nonlinear least squares approach .....	48
3.5 Specimen preparation and experimental procedure.....	50
3.5.1 Crack inclusion specimen preparation.....	50
3.5.2 Material characterization specimen preparation.....	53
3.5.3 Experimental procedure.....	53
3.6 Numerical computations of SIF's .....	55
3.6.1 SIF evaluation methodology using $J$ -integral approach.....	55
3.6.2 Finite element modeling .....	56
3.6.3 Interfacial layer debonding process.....	58
3.7 SIF estimation using DIC .....	60
3.8 Results and Discussion .....	71
3.8.1 Material characterisation using 3D-DIC.....	71
3.8.2 Crack inclusion interaction study .....	73
3.8.3 Parametric study .....	75
3.9 Closure.....	76
<b>4 Conclusion and Recommendations for Future Work .....</b>	<b>78</b>

# List of Figures

Fig. 1.1 Percentage of material used in the Boeing 787 [2] .....	7
Fig. 1.2 Application of patch repair on damaged fuselage of an aircraft [5] .....	8
Fig. 1.3 Schematic of (a) Repaired specimen (b) Single sided repair (c) Double sided repair	9
Fig. 1.4 Displacement field for SEN specimen with inclusion obtained from DIC (a) $u$ - displacement contour map and (b) $v$ -displacement contour map .....	14
Fig. 1.5 Experimental setup comprising of MTS equipment along with 3D DIC system ....	16
Fig. 1.6 Schematic diagram of deformation process with subsets in deformed and undeformed state .....	16
Fig. 2.1 Geometry of the specimen (a) front and side view of circular cutout panel. (b) side view of single sided repair (c) side view of double sided repair (All dimensions are in mm) .....	19
Fig. 2.2 Finite element model of open cutout and repaired panel (a) meshed configuration of the cutout panel (b) 2-D model of patch (c) section view of double sided repair (d) single sided repair .....	20
Fig. 2.3 Flowchart of optimization using genetic algorithm in-conjunction with FEA .....	23
Fig. 2.4 Specimen fabrication process .....	25
Fig. 2.5 Experimental setup comprising of MTS equipment along with 3D DIC system ....	26
Fig. 2.6 Longitudinal stress ( $\sigma_{xx}$ ) versus number of elements along the hole periphery for mesh convergence study .....	27
Fig. 2.7 Comparative plot of analytically obtain longitudinal stress versus finite element values along the net-section of circular cutout panel .....	28
Fig. 2.8 Whole field stress contour plots of various components in externally bonded double sided repair from 3D FEA (a) longitudinal stress ( $\sigma_{xx}$ ) in repaired panel (b) peel stress ( $\sigma_{zz}$ ) in adhesive (c) longitudinal stress ( $\sigma_{xx}$ ) in patch .....	29
Fig. 2.9 Variation of SCF in Zone A and B of panel with varying patch thickness.....	31
Fig. 2.10 Variation of SCF and normalized shear stress with different patch thickness (adhesive thickness 0.15 mm) (patch diameter 40 mm).....	31
Fig. 2.11 Variation of stress SCF and normalized shear stress with adhesive thickness for double sided repair (patch diameter 40 mm).....	32
Fig. 2.12 Variation of shear stress ( $\tau_{xz}$ ) along the longitudinal axis repaired with different adhesive thickness.....	32
Fig. 2.13 Variation of SCF and normalized shear stress with varying patch diameter .....	33
Fig. 2.14 Variation of normalized shear stress ( $\tau_{xz}$ ) along the longitudinal axis for different patch diameter .....	33

Fig. 2.15 Convergence plot for GA algorithm .....	35
Fig. 2.16 Whole field strain ( $\epsilon_{xx}$ ) distribution of a circular cutout panel under tensile load..	37
Fig. 2.17 Whole field strain ( $\epsilon_{xx}$ ) distribution of a single sided repair panel under tensile load .....	37
Fig. 2.18 Whole field strain ( $\epsilon_{xx}$ ) distribution of a double sided repair panel under tensile load.....	38
Fig. 2.19 Failure mechanism in [45/-45/0/90]s panel under tensile load (a) open cutout panel (b) single sided repaired panel (c) double sided repaired panel .....	39
Fig. 2.20 Comparison of whole field strain contour obtained from DIC and FEA for open cutout panel under tensile load of 10 kN (a) DIC (b) FEA (ADS) (c) FEA (AS) - $\epsilon_{xx}$ plot (d) DIC (e) FEA (ADS) (f) FEA (AS) - $\epsilon_{xy}$ plot (ADS – adjusted scale of FEA with DIC scale, AS - Actual scale of FEA plot) .....	40
Fig. 2.21 Comparative line plot of $\epsilon_{xx}$ between DIC and FEA along the net-section of open cutout panel.....	40
Fig. 2.22 Comparison of whole field strain contour obtained from DIC and FEA for single sided repair panel under tensile load of 10 kN (a) DIC (b) FEA (ADS) (c) FEA (AS) - $\epsilon_{xx}$ plot (d) DIC (e) FEA (ADS) (f) FEA (AS) - $\epsilon_{xy}$ plot (ADS – adjusted scale of FEA with DIC scale, AS - Actual scale of FEA plot) .....	41
Fig. 2.23 Comparison of whole field strain contour obtained from DIC and FEA for double sided repair panel under tensile load of 10 kN (a) DIC (b) FEA (ADS) (c) FEA (AS) - $\epsilon_{xx}$ plot (d) DIC (e) FEA (ADS) (f) FEA (AS) - $\epsilon_{xy}$ plot (AS – adjusted scale of FEA with DIC scale, AS - Actual scale of FEA plot) .....	42
Fig. 3.1 General steps involved in the determination of mixed-mode SIF's using DIC .....	46
Fig. 3.2 Specimen geometries for various specimen configurations (all dimensions are in mm) (a) SEN with single inclusion (b) ESC with single inclusion (c) SEN with two eccentric inclusions .....	47
Fig. 3.3 Mould used for preparing crack inclusion specimens.....	51
Fig. 3.4 Crack inclusion interaction Specimens with speckle (a) SEN with single inclusion (b) SEN with double inclusion.....	51
Fig. 3.5 (a) ESC with single inclusion full specimen (b) Zoomed speckle near crack inclusion.....	52
Fig. 3.6 Specimen geometry for tensile test according to ASTM D638 .....	52
Fig. 3.7 Experimental setup comprising of MTS equipment along with 3D DIC system ....	54
Fig. 3.8 Experimental setup for ESC with single inclusion specimen .....	54
Fig. 3.9 Nodes nearer to crack tip (a) two coincident nodes near the crack tip before loading (b) two nearest nodes near the crack tip after loading.....	56

Fig. 3.10 Finite element model of SEN with single inclusion specimen (a) Front view of half symmetry model with boundary conditions (b) Zoomed view of interfacial debonding layer between glass and epoxy [47] .....	57
Fig. 3.11 Finite element model of ESC with single inclusion specimen (a) Front view of full model with boundary conditions (b) Meshing around crack tip .....	58
Fig. 3.12 Flow diagram for interfacial layer debonding using ANSYS APDL .....	59
Fig. 3.13 showing the results of data analysis for SEN with single inclusion specimen (a) region of interest with subsets used for correlation (b) $u$ -displacement contour map (c) $v$ -displacement contour map (subset size: $15 \times 15$ ) .....	60
Fig. 3.14 showing the results of data analysis with subset size: $15 \times 15$ (a) $u$ -displacement contour map (b) $v$ -displacement contour maps for ESC with single inclusion specimen ...	61
Fig. 3.15 showing the results of data analysis for SEN with double inclusion specimen (a) $u$ -displacement contour map (b) $v$ -displacement contour map (subset size: $17 \times 17$ ).....	61
Fig. 3.16 Theoretically reconstructed displacement field for SEN with single inclusion specimen for various parameters with data points echoed back indicated by red marker points (all displacement values are in mm) .....	63
Fig. 3.17 Graph showing variation of $K_I$ as a function of number of parameters.....	64
Fig. 3.18 Graph of (a) convergence error and (b) co-ordinates of the crack-tip location vs. number of parameters.....	65
Fig. 3.19 Displacement field obtained from finite element analysis showing $v$ -displacement in the crack inclusion region (a) before debonding of inclusion (b) after debonding of inclusion .....	65
Fig. 3.20 Theoretically reconstructed displacement field for ESC with single inclusion specimen for 12-parameter solution (all displacement values are in mm) .....	66
Fig. 3.21 Graph showing variation of mixed mode SIF's as a function of parameters (a) $K_I$ (b) $K_{II}$ .....	67
Fig. 3.22 Graph of (a) convergence error and (b) co-ordinates of the crack-tip location vs. number of parameters.....	68
Fig. 3.23 Theoretically reconstructed displacement field for SEN with two eccentric inclusion specimen for various parameters (all displacement values are in mm) .....	69
Fig. 3.24 Graph showing variation of $K_I$ as a function of number of parameters .....	70
Fig. 3.25 Graph of (a) convergence error and (b) co-ordinates of the crack-tip location vs. number of parameters.....	71
Fig. 3.26 Material characterization using DIC (a) Specimen with extensometer and ROI (b) $u$ -displacement contour map (c) $v$ -displacement contour map.....	72
Fig. 3.27 Stress strain curve obtained from DIC.....	72
Fig. 3.28 Poisson's ratio obtained from DIC .....	73

Fig. 3.29 Variation of SIF with load obtained from DIC for ESC with inclusion specimen	74
Fig. 3.30 Variation of stress intensity factor (S.I.F) with varying distance from crack tip to edge of inclusion diameter (inclusion diameter 6 mm, young's modulus 2.5 GPa and Poisson's ratio 0.35)	75
Fig. 3.31 Variation of stress intensity factor (S.I.F) with varying inclusion diameter (distance from crack tip to edge of inclusion 6.5 mm, young's modulus 2.5 GPa and Poisson's ratio 0.35)	75
Fig. 3.32 Variation of stress intensity factor (S.I.F) with varying Young's modulus of inclusion (inclusion diameter 6 mm and Poisson's ratio 0.35)	76
Fig. 3.33 Variation of stress intensity factor (S.I.F) with varying Poisson's ratio of inclusion (inclusion diameter 6 mm and young's modulus 2.5 GPa)	76

## List of Tables

Table 2.1 Material properties of CFRP laminate and adhesive.....	21
Table 2.2 SCF and normalized shear stress values obtained for models different patch stacking sequences .....	30
Table 2.3 SCF comparison between open cutout, single sided and double sided repair model .....	34
Table 2.4 Parameters used in the GA optimization scheme .....	35
Table 2.5 Optimized repair parameters from genetic algorithm .....	36
Table 2.6 Maximum, mean and standard deviation in maximum load for open cutout and repaired specimen.....	43
Table 3.1 Speckle density for different configurations of crack inclusion interaction specimens .....	54
Table 3.2 Material properties of epoxy (resin CY230 and hardener HY951).....	73
Table 3.3 Comparison of SIF value obtained from FEA and DIC.....	74

# Chapter 1

## Introduction and Literature Review

### 1.1 Introduction

#### 1.1.1 Composite Materials: An Overview

A composite is any material made up of two or more different material phases on microscopic/macroscale, utilizes beneficial mechanical and thermal characteristics of individual phases to get the desired overall behaviour [1]. Usually, composite materials will consist of two separate components, the matrix and the filler. The matrix is the component that holds the filler together to form the bulk of the material. The filler is the material that has been impregnated in the matrix to add its advantage to the (strength) composite. These fillers can be in the form of long fibers, whiskers or particles of different size and shape. Composite materials are classified into three broad categories according to the filler material [1]: particulate composites, laminated composites and fibrous composites. Particulate composites are the materials which consist of matrix and particles of different size and shape. Laminated composite is a material that uses the filler material in the form of sheets instead of round particles or fibers. Fiber reinforced composite materials are those in which fibers of significant strength and stiffness are embedded in a matrix. The common fiber reinforced plastics generally contain fibers such as carbon, boron or glass oriented in either unidirectional or multidirectional architecture and bonded together by a polymer such as epoxy, polyester, etc. Composite material especially carbon fiber reinforced polymer (CFRP) has seen a remarkable increase and extensive usage in aerospace, automobile, civil and sports equipment industries in recent years because of their high specific strength, high stiffness, improved corrosion resistance and larger fatigue life. Now days in aircraft structures, content of composite materials has increased dramatically and it is now more than 50% as shown in Fig. 1.1 [2]. New commercial aircraft like Boeing 787 and Airbus 350 are the first commercial aircrafts with composite in fuselage structure [3]. The composite materials have an orthotropic nature which leads to complex mechanical behavior from those of conventional isotropic materials. These materials are very brittle in nature and while in use catastrophic structural failure may occur and it may lead to loss of life. Therefore, it is of great importance to study the failure mechanism in fiber reinforced composites.

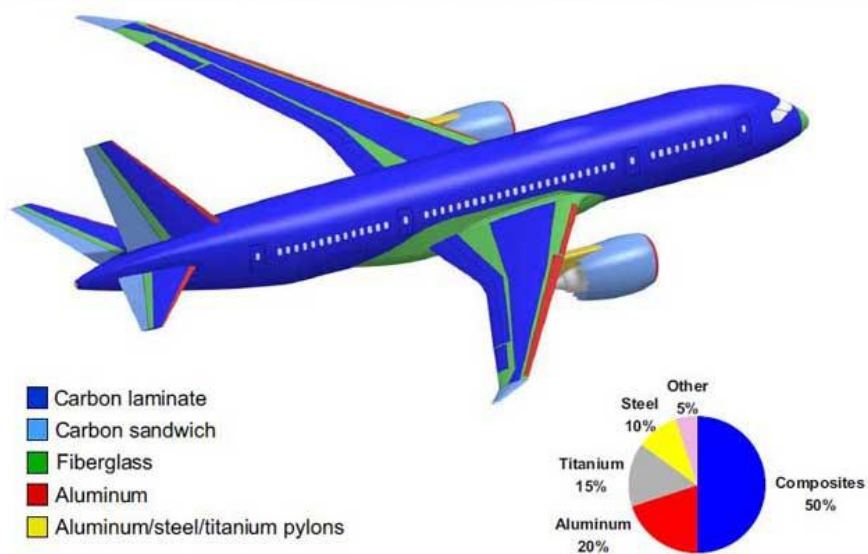


Fig. 1.1 Percentage of material used in the Boeing 787 [2]

### 1.1.2 Repair Study on Damaged CFRP Laminates

During the service life composite structures are prone to damages due to accidental impact, bird strike, fatigue loading and aggressive environment. The damage in composite materials is in the form of matrix crack, fiber breakage, debonding, and delamination in the structure. It is well known fact that the presence of the damage such as crack, holes etc. in these composite structures and components reduces their strength and structural life considerably and is mainly responsible for initiation of fracture. But due to high cost of composite structures/retrofitting, it is not feasible to replace the structure and it needs to be repaired for continuous usage by improving their structural integrity. These repairs can possibly be achieved either by using mechanical fasteners or adhesively bonded patches. In case of mechanical fastener high stresses arise at the fastener holes resulting in significant stress concentration factor (SCF) thereby making it more damage prone compared to bonded patch repair. In contrast, adhesively bonded repair offer smooth load transfer from panel to patch as large load transfer area is available making it much stiffer than mechanical joint. Adhesively bonded repairs are highly cost effective and proven method for enhancing the structural integrity by reducing the stress concentration in the damaged area. They also provide very high level of bond durability under various operating conditions. From application point of view, two kinds of adhesively bonded repair are employed in composite repair. First is the scarf type bonded repair and second one is the externally bonded patch repair. In case of scarf joint, surface is machined in the parent laminate and replacement plies with adhesive are



cured into place. This repair technique is often applied where surface smoothness is essential since aerodynamic disturbance is minimized by using scarf repair. The scarf repair application procedure requires taper around the repair area to obtain the correct scarf angle, identify ply boundaries and complete removal of the damage. This repair will provide the highest joint efficiency among all the repair techniques. However there are certain disadvantages that have to be considered before the implementation of a scarf repair such as the design procedure. First of all the manufacturing of a scarf repair requires a higher level of expertise than the external patch and it results to the removal of excessive amount of undamaged material for the achievement of a scarf angle that will reduce the stiffness and strength of the structure. The application procedure of external patches is relatively simpler than the scarf approach and can be accomplished faster. The external patch approach is usually considered as a temporary repair solution in order to keep an airplane in serviceable condition or it can serve as a permanent repair in lightly loaded and relatively thin structures. The external patches transfer the load over and around the damage and reduce the localized stress concentration at the damage area. With this technique, the damaged material is removed by cutting a hole, cleaned and applied with filler and adhesive material before the patches are attached. Repair of aircraft aluminum structures using composite patch has been initiated by Baker et al [4] in the early 1970s mainly in order to enhance fatigue life of cracked components. The external patch approach is usually considered as the temporary repair solution in order to keep an airplane in serviceable condition or it can serve as a permanent repair in lightly loaded structures. This repair methodology has been used on aircraft and ship structures, and on wind turbine blades.

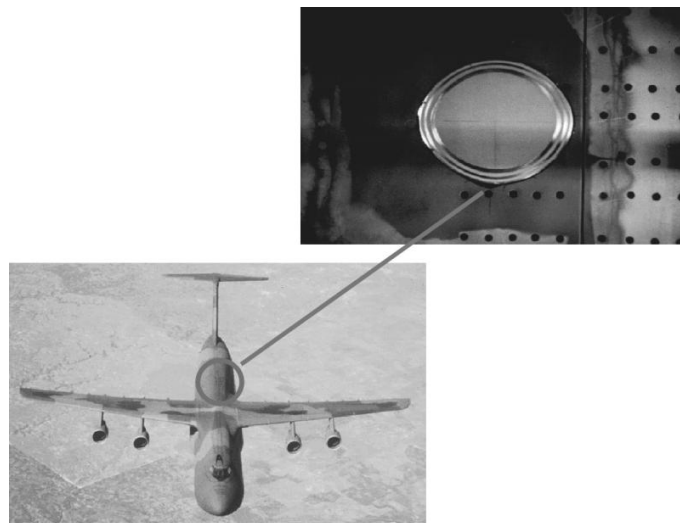


Fig. 1.2 Application of patch repair on damaged fuselage of an aircraft [5]

From technological aspects composite repair is categorized as active and passive repair. In past two decades, the performance of the repaired structures is analysed by employing passive patch work methodology. In recent years, attention has been paid by the researchers to explore active patch repair by incorporating smart materials [6]. In active patch repair, the smart patches made of piezoelectric actuators are used which can enable the active restoration of strength and stiffness of repaired structure by introducing a local moment/force in opposite sense thereby reducing the stress intensity factor SIF [7]. However from geometrical point of view, two different methodologies are adopted to repair the damaged panel. First kind is the composite patch bonded on to one side of the panel over the damaged area called single sided or unsymmetrical repair and the second kind is the patch bonded on to both sides of the panel called as double sided repair or symmetrical repair.

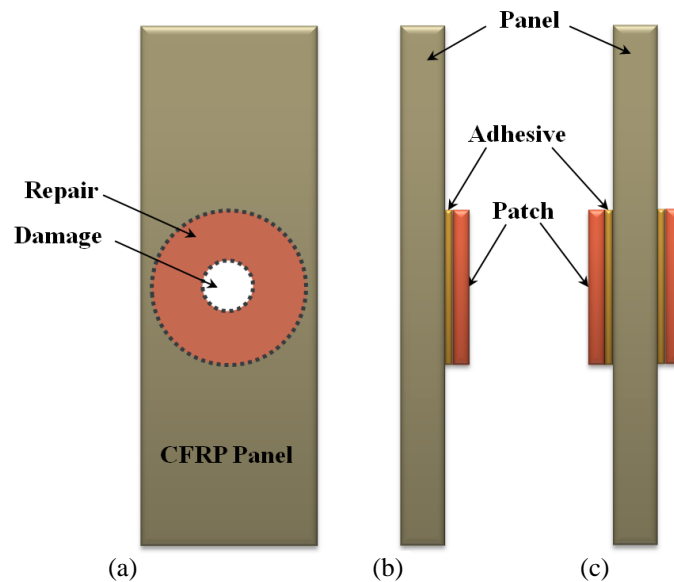


Fig. 1.3 Schematic of (a) Repaired specimen (b) Single sided repair (c) Double sided repair

In case of single sided repair, bending stress in addition to in-plane stress is present and this bending increases the stress levels at unrepaired surface. Double sided repair ensures that there is only in-plane loading and therefore it is preferred over single sided repair. Also in case of double sided patch repair both faces of the panel must be available for patching. But only in very few instances it is possible. However in most of practical applications only one face of the structure to be repaired is available (e.g. repairs on wings and fuselage of aircraft). The performance of externally bonded patch repair depends on various parameters like patch stacking sequence, patch shape, patch thickness, overlap length and adhesive thickness. To improve the performance of repaired structure these parameters needs to be optimized. Over

the last two decades, researchers have performed both experimental and numerical studies to understand the mechanics of adhesively bonded repair on aluminum panels [8-14]. But not much work exists in the literature in the area of optimization of composite patch repair applied to damaged CFRP laminates.

### **1.1.3 Crack Inclusion Interaction Study**

The increasing use of composites in the design of structural parts requires fundamental understanding of its behavior for various kind of loads. Since they are made of fibres and matrix study of matrix crack interacting with an inclusion will be a fundamental work to study. It is well-known facts that fracture in composite materials have compound behaviour since regions of stress concentration such as fibers, whiskers and particles are intrinsically present in these materials. The causes for the presence of cracks or crack like defects are virtually impossible to avoid in composite materials due to defects like voids, porosity, ply drops and delamination are inherently present in these materials. The cracks can be induced during service life due to fatigue loading and harsh environment. An understanding of fracture mechanisms in these materials can be studied using a problem of matrix crack interacting with an inclusion. The crack inclusion interaction problem can be solved using analytical, numerical and experimental methods. Some of the problems are solved using analytical approach but more complex problem requires numerical method. The numerical methods require precise knowledge about the boundary conditions and loading and these results need to be compared with experimental one for finite element model validation. The experimental methods are particularly well suited for crack inclusion interaction problem due to it gives better understanding of fracture mechanisms in composite materials and accurate results. A detailed review of application of experimental techniques (photoelasticity and moiré interferometry) to crack inclusion interaction problem is available in literature. But not much more work exists in the literature related to the experimental technique namely DIC applied to mixed mode crack inclusion interaction problem. Thus, DIC have been considered in this work for the estimation of SIF's for mode I and mixed mode crack inclusion interaction specimens subjected to tensile load.

## **1.2 Literature Review**

### **1.2.1 Repair Study on Damaged CFRP Laminates**

Externally bonded composite patches have proved to be an effective method of repairing cracks and damages in aircraft structures. The pioneered of this technology is aeronautical

and maritime research laboratory of the Royal Australian air force under the direction of Backer et al. [4] in the early 1970s. They have carried out repair study on cracked aluminium components mainly in order to enhance fatigue life of cracked components. Till date, lot of experiment and numerical studies have been done in area of composite repair on cracked aluminium panels to understand the mechanics and to improve the fatigue life [6-14]. Over the last two decades, researchers have performed experimental and numerical analysis to study the performance of externally bonded repair on damaged CFRP panels subjected to compressive/tensile load. Scott et al. [15] have carried out the experimental analysis to determine the compressive strength of damaged plates. They concluded that the plug repair of damaged plate does not influence the compressive strength of repaired panel. Soutis et al. [16] have carried out an experimental study to monitor the damage process in the adhesively bonded repair structures subjected to compressive load. They have also used the finite element analysis (FEA) to investigate the optimum patch overlap length and patch thickness. Hu and Soutis [17, 18] have conducted experimental and numerical study for prediction of compressive strength of CFRP laminates repaired using external patches. Using analytical and numerical approach they have deduced the optimum patch diameter.

Campilho et al. [19] have conducted the experimental and numerical study to investigate the tensile behaviour of single and double lap repairs for different overlap lengths and patch thicknesses. They found that the overlap length has more influence on repair strength. Tsai and Morton [20] have conducted experimental, numerical and analytical study to analyze the stress distribution and mechanics of double lap joint composite plates with different stacking sequences subjected to tensile load. They have thoroughly investigated the mechanics of joints using moiré's interferometry and presented an analytical approach based on one-dimensional closed-form solution. Mathias et al. [21] have carried out an experimental study on the mechanical behavior of composite patches bonded onto aluminum specimens subjected to tensile loading. They have obtained the displacement field on the patch surface using grid method. Zehnder and Ermanni [22] have carried out numerical based analysis for arriving at an optimum patch shape in case of single sided repair. Pencheng et al. [23] have performed both experimental and finite element analysis of patch repaired CFRP laminates subjected to tensile load. Initially, FEA based study is carried out to design the patch and to study the stress/strain distribution in the repaired panel. They observed that damage initiated from longitudinal edges of the circular patches and also at the transverse edge of the hole. They have concluded that optimized repair system can restore more than 90% of virgin panel strength. Caminero et al. [24] have presented online damage monitoring technique

involving DIC and lamb waves applied to composite patch repair. They have studied strain distribution in repaired as well as unrepaired panel using DIC and FEA. Recently, Kashfuddoja and Ramji [25, 26] have conducted the DIC based experimental study to investigate the whole field strain distribution over damaged and repaired unidirectional CFRP laminates. They observed that the damage propagation is perpendicular to hole edge towards tab end and final failure is due to fiber splitting.

Also in composite repair, researchers have employed genetic algorithm (GA) approach for optimization of patch geometry and layup sequence. Callahan and weeks [27], Ball et al. [28] and Riche and Haftka [29] are the researchers who have adopted GA for the optimization of stacking sequence in laminated composite plate. Sivakumar et al. [30] have performed the optimization of composite laminate having open cutout using GA. They have used variable metric and complex search methods and concluded that GA is the best tool to optimize the composite laminates. Mathias et al. [31] have carried out GA based analysis for the design optimization of composite patch bonded on aluminum plate containing a circular hole. They have investigated the optimum ply orientations as well as the patch shape. Almeida and Awruch [32] have carried out multiobjective optimization to study the stiffness maximization of a composite shell under pressure load using a genetic algorithm associated with FEA. Many researchers have used different experimental techniques to address the issue of accurate measurement of surface displacement, strain and damage detection in the open cutout and repaired composite specimens. These techniques include resistance strain gauges which provide only point wise measurement as well as whole field non-contact optical techniques based on interferometry or non-interferometry. In case of interferometry technique electronic speckle pattern interferometry [33], moiré interferometry is employed but they are very sensitive to vibration and optics is quite challenging/involved. Also reflection photoelasticity [34] is employed but sample preparation is very tedious. In case of non-interferometry techniques grid method and DIC are used. Amongst them, DIC have become most popular in the field of experimental mechanics because of their relatively easier specimen preparation and simpler optical arrangement. In the present work DIC is used to estimate the whole field displacement/strain field in open cutout as well as on repaired specimen.

### **1.2.2 Crack Inclusion Interaction Study**

The study of crack inclusion interaction has been initiated by Tamate [35] in the early 1960s. He has carried out analytical study to analyze the effect of a circular inclusion of different elastic modulus on the stress state around a crack using Mushkhelishvili's complex variable

approach as well as the SIF variation for different crack inclusion configurations using the numerical approach. He concluded that a circular hole ahead of a crack increases SIF where as an inclusion reduces the same. Atkinson [36] has carried out crack inclusion study under uniaxial and biaxial tension for different crack lengths and elastic properties of the inclusion and matrix. He used singular integral approach numerically to investigate the SIF variations as a function of the distance between the crack tip and inclusion. Erdogan et al. [37] have investigated mixed mode stress intensity factors using Green's function for interaction between an arbitrarily oriented crack and a circular inclusion. Gdoutos [38, 39] conducted analytical study of interaction between a crack and a hole or a rigid inclusion subjected to uniform tension. He found out critical values of the applied stress for crack extension and concluded that in case of a hole fracture strength decreases and in case of inclusion it increases. Hasebe et al. [40] have performed study using mixed boundary value problem for a model of a debonding and a crack occurring from a circular rigid inclusion in an infinite plate subjected to tension. They studied the stress distribution, SIF and stress singular values at a debonded tip. Patton and Santare [41] have studied the interaction of a matrix crack with elliptical inclusions using Muskhelishvili's complex potential functions. They have concluded that as the crack approaches towards the flat side of the inclusion the stress intensity decreases drastically. Bush [42] investigated interaction between a single and multiple inclusions and a matrix crack using boundary element method. He has examined the crack propagation paths and energy release rates (ERR) for crack initiation and growth. O'Toole and Santare [43] have carried out the experimental study using photoelasticity to investigate the SIF of a straight crack near a rigid elliptical inclusion. They have showed that toughening effect is more for a case of major axis of an inclusion is normal to the crack plane. Easley et al. [44] carried out experimental study using moiré interferometry to investigate stress field in a fiber pullout test in the presence of in the presence of nearby matrix cracks.

Savalia et al. [45, 46] conducted experimental and numerical study to investigate the CMOD in three-point bend epoxy specimen with an edge crack and a cylindrical glass inclusion using full-field displacement measurements. They used moiré interferometry to obtain surface deformations in the vicinity of a crack-inclusion pair. Later, the same method is used for inclusion debonding detection by observing asymmetry in displacements around the inclusion. They have also studied the debonding of an inclusion from the surrounding matrix in the presence of a nearby crack tip as well as the effects of different parameters such as the distance between the crack tip and inclusion center, the inclusion diameter and the Young's modulus ratio on the CMOD using FEM. Prasath and Ramji [47] have performed both

experimental and finite element analysis of interaction between matrix crack and glass rod inclusion just ahead of a crack tip subjected to tensile loading. Initially, experimental based study is carried out using digital photoelasticity to investigate the stress intensity factor. They used an over deterministic system of equations by nonlinear least square approach to evaluated the mode-I SIF and the same is compared with finite element analysis. They found a good agreement between the results obtained from digital photoelasticity and FEA.

Veerkar [48] have conducted the photoelasticity and DIC based experimental study to investigate the mixed mode SIF's in the homogeneous material. He developed the algorithm in MATLAB [49] using over-deterministic nonlinear least square approach for the estimation of SIF's using whole field displacement data obtained from the DIC. He has validated the methodology with analytical solutions and the results are found in a good agreement. Many researchers have developed and applied methodologies for estimating SIF's for the matrix crack inclusion interaction problems. These experimental techniques include whole field non-contact optical methods such as photoelasticity [43, 47] and moiré interferometry [45]. Amongst these experimental techniques, digital image correlation (DIC) have become the most popular ones for SIF determination because of their relatively simple specimen preparation, ease of use and requirement of less complicated optics. Thus, DIC have been considered in this work for the estimation of mixed mode SIF's. Figure 1.4 shows the whole field  $u$  and  $v$  displacement contour maps for single edge cracked panel with circular inclusion ahead of the crack subjected to tensile load.

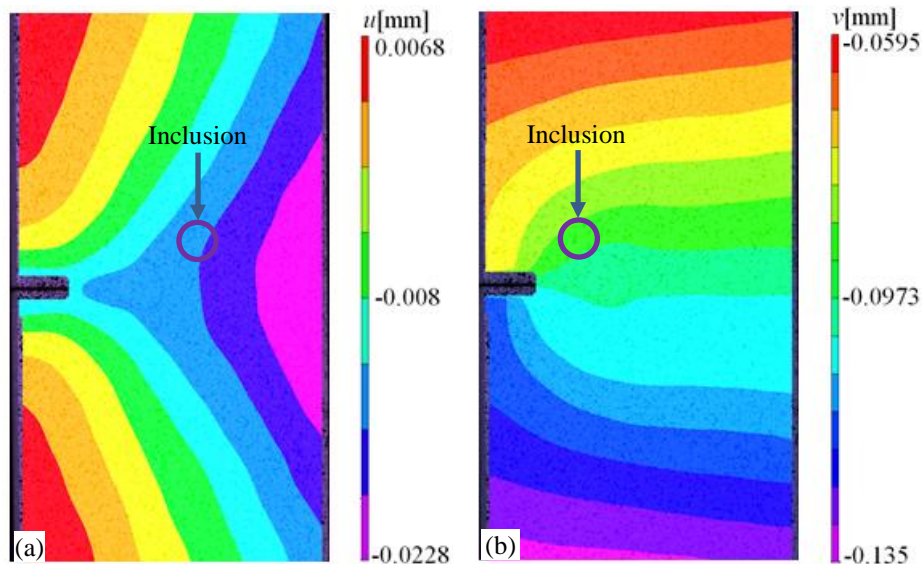


Fig. 1.4 Displacement field for SEN specimen with inclusion obtained from DIC (a)  $u$ -displacement contour map and (b)  $v$ -displacement contour map

### 1.3 Experimental Study Involving DIC

The DIC is a non-interferometry, non-contact, full-field optical technique for measuring both in-plane and out-of-plane displacements of an object surface subjected to loading. In 2D DIC single camera is kept perpendicular to the specimen. It can measure only in plane surface displacement but in most of the practical cases it may not be possible to avoid the out-of-plane deformation. To overcome this fundamental limitation, 3D DIC is used in this study. The 3D DIC setup (see Fig. 1.5) uses a stereo vision system employing two cameras to accurately measure the full three dimensional shape and deformation of a curved or planar object. The principle is based on speckle pattern matching over a subset between the reference and deformed image. A small square subset in reference image is selected and using appropriate correlation function this subset position is found out in deformed image as shown in the Fig. 1.6. A zero-normalized cross-correlation coefficient (ZNCC) is used to evaluate the degree of similarity between the subsets from reference image and the deformed image [50]. A typical cross-correlation function that measures how well two subsets match each other is given below:

$$C(x, y, u, v) = \frac{\sum_{x=-M}^M \sum_{y=-M}^M [f(x, y) - f_m] \times [g(x', y') - g_m]}{\sqrt{\sum_{x=-M}^M \sum_{y=-M}^M [f(x, y) - f_m]^2} \sqrt{\sum_{x=-M}^M \sum_{y=-M}^M [g(x', y') - g_m]^2}} \quad (1.1a)$$

Where,

$$x' = x + u + \frac{\partial u}{\partial x} dx + \frac{\partial u}{\partial y} dy \quad (1.1b)$$

$$y' = y + v + \frac{\partial v}{\partial x} dx + \frac{\partial v}{\partial y} dy \quad (1.1c)$$

where  $f(x,y)$  is the gray level value at point  $(x,y)$  of the reference of the reference image and  $g(x',y')$  is the gray level at point  $(x',y')$  of the deformed image. The parameters  $f_m$  and  $g_m$  indicate the mean gray values of the subsets before and after deformation respectively. Once the maximum of this correlation coefficient is detected then the position of deformed subset is determined. From the deformation, strains are evaluated using numerical differentiation [50].



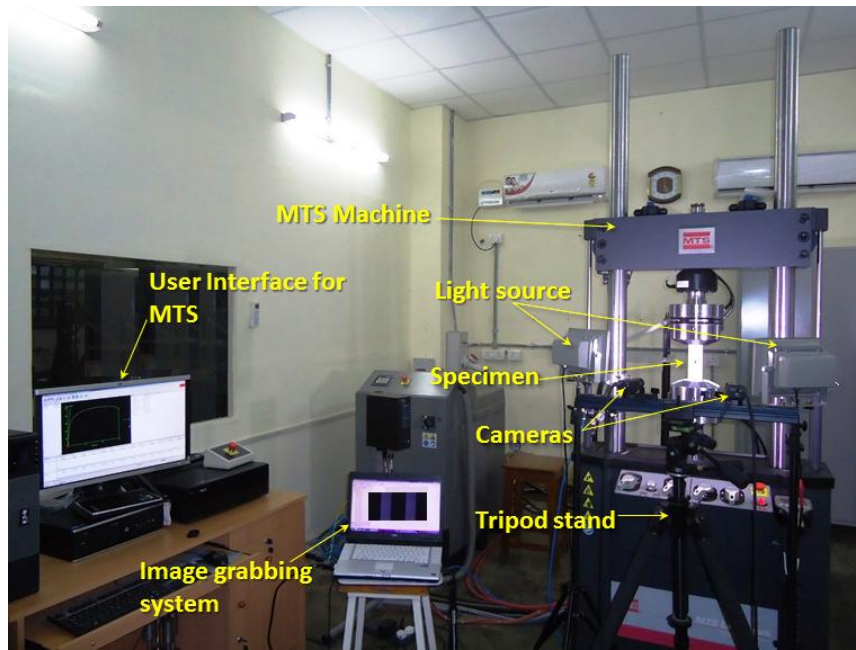


Fig. 1.5 Experimental setup comprising of MTS equipment along with 3D DIC system

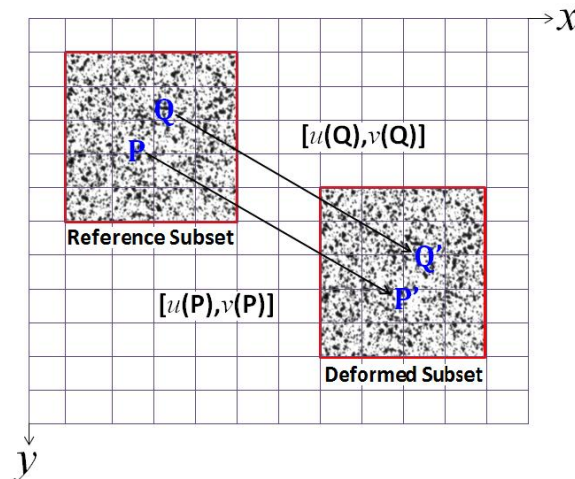


Fig. 1.6 Schematic diagram of deformation process with subsets in deformed and undeformed state

### 1.4 Scope and Motivation

Due to the increased use of the composite materials in aircraft structures, the number of damage occurrence in composite structures is expected to rise as well. The repair of these load-carrying structures must restore strength and stiffness. The repair performance is mainly influenced by patch stacking sequence, patch thickness, overlap length and adhesive thickness. Initially the influence of various patch parameters including adhesive thickness is studied mechanics based approach involving FEA. There is scope for optimizing the

parameters of patch repair parameters for given a quasi-isotropic damaged CFRP panel under tensile loading using GA based approach.

Most of the crack inclusion interaction study has been carried out using analytical method. Only few experimental works exists in the literature. Also most of the study involved mode I specimen and not much work exist for mixed mode crack inclusion interaction. Now days, Optical techniques are extensively used in the area of fracture mechanics for mapping full field displacement, stain and stress components to estimate the SIF's. DIC technique is used in the present work to estimate the SIF's under mode I and mixed mode loading. As well as FEA based study is carried out to simulate their behavior under the same load. The effects of various parameters such as the inclusion diameter, inclusion distance from crack tip and inclusion stiffness on the SIF are studied systematically using FEA.

### **1.5 Thesis Layout**

Chapter 1 deals with the introduction to composite materials, repair study of damaged CFRP laminates and matrix crack inclusion interaction. Also a brief literature review of composite patch repair and crack inclusion interaction problem is presented. Finally, scope and motivation is defined.

Chapter 2 deals with the optimization of composite patch reinforcement on damaged CFRP laminates involving genetic algorithm. Firstly the influence of various repair parameters on repair performance is studied and prioritized. Later, optimization involving GA based approach is carried out in conjunction with FEA to arrive at optimum patch geometry. Also a comparative study between DIC and FEA strain field is done to validate the FEA model.

Chapter 3 considers the estimation of SIF using DIC technique for matrix crack inclusion problem. It describes the methodology, implementation, details of specimen preparation and experimentation. Later FEA based study done to simulate inclusion debonding from the matrix in the presence of a matrix crack. Also a comparative study between experimental and FEA results is made and results obtained from parametric study are discussed.

Chapter 4 deals with the conclusion and recommendation for the future work.

# Chapter 2

## Optimization of composite patch repair

### 2.1 Introduction

In order to extend the life of an aircraft, the damage needs to be repaired. Repair of the structures is feasible only if the size of the damage is small compared to the panel dimensions. These repairs can possibly achieve either by using mechanical fasteners or adhesively bonded patches. Adhesively bonded repairs have now replaced the riveted patches for the various advantages it possess over mechanical fasteners. The adhesively bonded repairs are carried out in two ways; single and double sided repair. In double sided repair, both faces of the damage area are patched and in single sided repair only one side of the panel is patched. For double sided repair, both faces of the panel must be available for patching but in very few instances it is possible. Double sided repair is more preferred to single sided repair as there is no shift of neutral axis in repair panel system thereby avoiding any out plane bending. In most of the practical cases, only one side of the panel is available for repair such as aircraft wings. Composite patch repair is mainly concerned with repairing of the damaged aircraft structure; damaged blades of wind turbine or ship structures. Most of the previous work in literature mainly focuses on the double sided patch repair as compared to single sided patch repair.

In this chapter, both numerical and experimental based study is carried out to understand the mechanics of single and double sided repair on damaged CFRP panel of configuration [45/-45/0/90]<sub>s</sub>. Initially, FEA based study is carried out to study the influence of various patch parameters on repair performance for double sided repair panel. The parameters are patch stacking sequence, patch thickness, adhesive thickness and overlap length. The influence on repair performance are investigated through a mechanics based approach and optimum values are obtained. The stress concentration factor, shear stress in adhesive layer and peel stress at patch overlap edge/hole circumference are considered for arriving at desired patch dimension. Later, a GA based approach in-conjunction with FEA is implemented to arrive at the optimum patch dimension leading to higher repair performance considering the above mentioned parameters.

Finally, experimental study is carried out with these optimized geometry using DIC technique. Whole field surface strain from finite element prediction is compared with the

DIC results for the validation of the finite element model. Experimental results are also compared with the finite element (FE) estimate for qualitative analysis. Also the maximum tensile strength for damaged and repaired panel is determined from the test.

## 2.2 Problem Description

The specimen geometry of open cutout, single sided and double sided repaired panel are shown in Fig. 2.1. The panel is of 250 mm length, 50 mm width, and 2.4 mm thickness. The stacking sequence of panel is  $[45/-45/0/90]_s$ . The average ply thickness is 0.3 mm. The panel has a circular hole of diameter 10 mm at the center for simulating the damaged area. The composite panel and patch is made up of unidirectional carbon fiber. The patch is bonded to the panel using adhesive ARALDITE 2011 adhesive system. Influence of different parameters such as patch thickness ( $t_p$ ), adhesive thickness ( $t_a$ ), patch diameter ( $D_p$ ) and patch layup sequence on repair performance will be studied and later optimized for lower SCF in the panel.

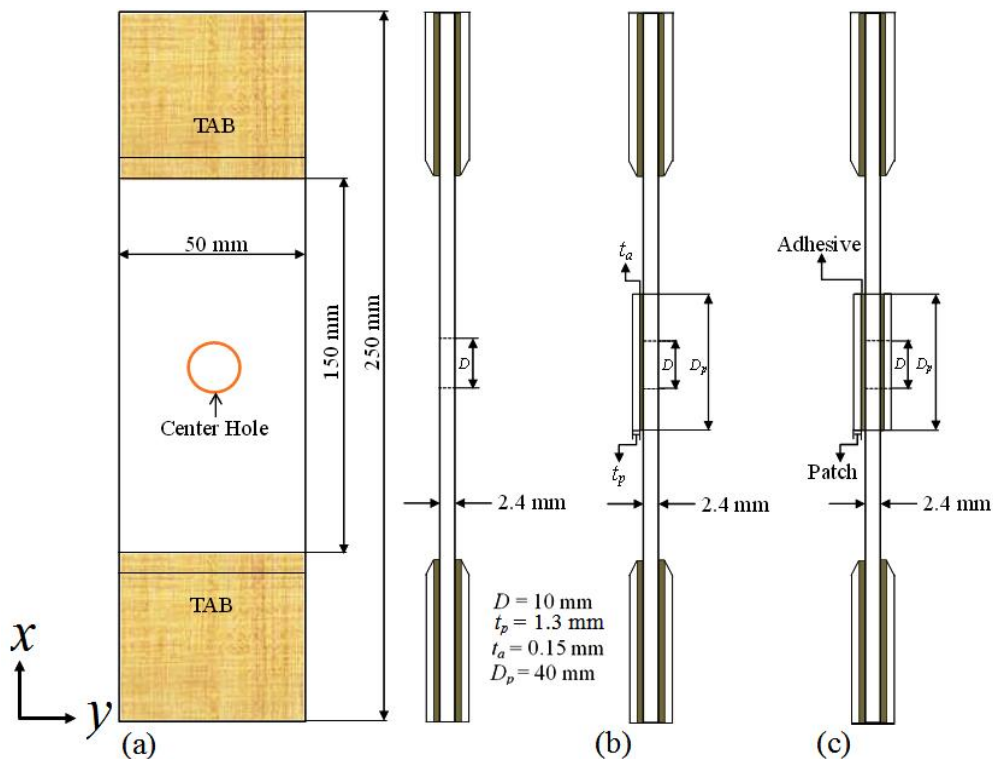


Fig. 2.1 Geometry of the specimen (a) front and side view of circular cutout panel. (b) side view of single sided repair (c) side view of double sided repair (All dimensions are in mm)

## 2.3 Numerical Study

### 2.3.1 Finite Element Modeling of Circular Cutout Panel

The finite element model of the considered geometry is shown in Fig. 2.2. The commercially available finite element package ANSYS 13 is used in the current study. A general finite element code known as Ansys Parametric Design Language (APDL) is written specifically for this study. Initially two dimensional area is created as per the model dimension and meshed with mesh 200 element having 8-nodes. Later, all the areas are extruded in thickness direction to generate volume using sweep mode. The mesh pattern around the hole is kept very fine in order to capture very high stress gradient around it and its size around the hole is 0.1mm. A mesh convergence study has been performed to arrive at number of elements surrounding the hole and it is found to be 96. The mesh around a hole consists of 46080 elements (96 circumferential, 60 radial, 8 elements in thickness direction). The panel, adhesive and patch are modeled with 20-noded solid 186 brick element. In the thickness direction, the panel is meshed with eight elements, adhesive with two elements and patch with four elements. The layer angles are defined by assigning appropriate element coordinate system to both panel and patch elements. Orthotropic material properties are assigned for the panel elements and a tensile load of 10 kN is being applied as a pressure load of 83.33 MPa on the top surface of the panel. The bottom face of the panel is arrested in all directions. The finite element model of open cutout panel is shown in Fig. 2.2(a).

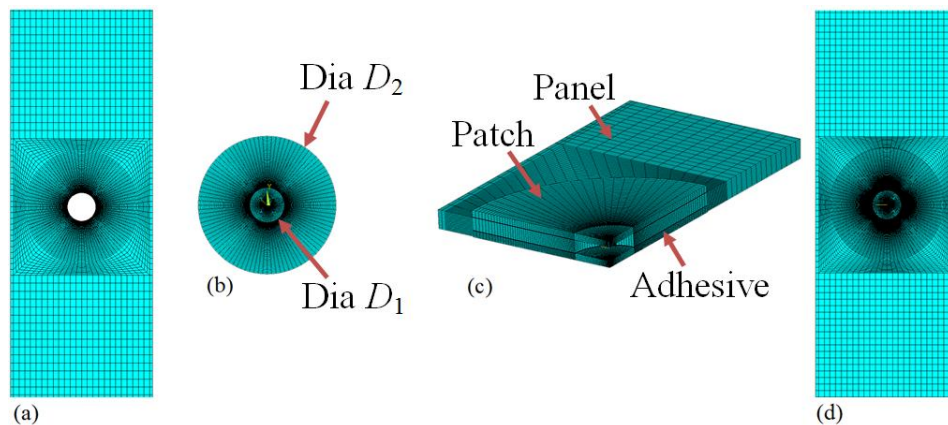


Fig. 2.2 Finite element model of open cutout and repaired panel (a) meshed configuration of the cutout panel (b) 2-D model of patch (c) section view of double sided repair (d) single sided repair

### 2.3.2 Finite Element Modeling of Circular Patched Panel

Initially circular area of diameter  $D_1$  and  $D_2$  are created towards patch generation. Diameter  $D_1$  is same that of hole diameter in panel ( $D_1=10$  mm) and diameter  $D_2$  is varied from 11 mm to 46 mm. The area corresponding to diameter  $D_1$  is meshed using 96 elements in

circumferential direction, 40 elements in radial direction with the spacing ratio of 0.2. Area corresponding to diameter  $D_2$  has element size 0.2 mm in radial direction. An area mesh is generated using element 200 as shown in the Fig. 2.2(b). Later, both the areas are extruded in thickness direction to generate patch and adhesive layer. Finally extruded volumes are meshed with 20-noded solid 186 element through sweep mode. To ensure the perfect bonding between panel/adhesive and patch/adhesive multi point constraint algorithm (MPC) is employed. The section view of double side repair model is shown in Fig. 2.2(c) where as single sided repair model is shown in Fig. 2.2(d). The panel and patch elements are assigned orthotropic properties where as the adhesive layer is isotropic. The shear strength of adhesive is 19.2 MPa, taken from manufacturer's data sheet and material property is from Ref. [51]. The material properties of CFRP laminate are taken from Ref. [26]. They are presented in Table 2.1. The repaired panel is also subjected to the same tensile load for a comparative study.

Table 2.1 Material properties of CFRP laminate and adhesive

<b>Composite (Carbon/Epoxy) Properties</b>	
Longitudinal modulus, $E_{11}$ (GPa)	81.9
Transverse modulus, $E_{22} = E_{33}$ (GPa)	6.15
Shear moduli, $G_{12} = G_{13}$ (GPa)	2.77
Shear modulus, $G_{23}$ (GPa)	2.05
Poisson's ratio ( $\nu_{12} = \nu_{13}$ )	0.34
Poisson's ratio ( $\nu_{23}$ )	0.5
<b>Adhesive (Araldite 2011) Properties</b>	
Young's modulus $E$ (GPa)	1.148
Poisson's ratio ( $\nu$ )	0.4
Shear strength ( $\tau_s$ ) (MPa)	19.2

## 2.4 Patch Design Study

### 2.4.1 Mechanics Based Design Approach

To study the mechanics of composite patch repair, FEA is ideally preferred for its versatility and accuracy. In externally bonded repairs, load is transferred from panel to the patch through the adhesive layer thereby increasing the static strength of damaged panel. The relative stiffness of the reinforcement as compared to the damaged panel determines not only the portion of load transferred but also the level of peak stresses in the adhesive layer and the stress concentration in the repaired panel. The mechanics based design approach is

convenient and also fundamental for studying the influence of various parameters in composite patch repair performance. The parametric study allows us to analyze the effect of patch stacking sequence, patch thickness, overlap length and adhesive thickness on SCF in the panel and also shear and peel stress level in the adhesive layer. In present work, the mechanics of double sided repair on damaged CFRP panel of configuration  $[45/-45/0/90]_s$  is analyzed by varying four different parameters that greatly influences the repair performance. These parameters are patch stacking sequence, patch thickness, overlap length and adhesive thickness. The analysis is done for different patch thickness ranging from 0.3 mm to 2.4 mm. The patch diameters are varied from 12 mm to 46 mm which correspond to the overlap length of 1 mm to 18 mm and adhesive thickness is varied from 0.05 mm to 0.25mm. The objective of this study is to find out the approximate value of these parameters resulting in lower SCF (in panel) and shear stress level in the adhesive layer.

The mechanics based design approach reveals the influence of various parameters on composite patch repair performance. It helps us in understanding the influence of various parameters on the repair performance by individually studying them. Further, it also helps us in arriving at a feasible range of various parameters. It is very difficult to achieve an optimum patch dimension by mechanics based design approach involving various parameters and therefore authors have resorted to regular optimization technique to get an optimum patch dimension corresponding to a minimum SCF. In the next sub-section, genetic algorithm based optimization technique is discussed for obtaining the optimum patch dimension and adhesive thickness.

#### **2.4.2 Optimization using GA Based Approach**

Genetic algorithm is an efficient global search optimization method based on Darwin's theory of evolution and survival of the fittest to produce successively better approximations to a solution [52]. GA is a numerical method to find an optimum solution from a set of possible solutions. The set of possible solutions is called the population. Individual solution in the population is called as a chromosome. At initial generation of genetic algorithm, population of chromosomes is generated randomly and these chromosomes are used as an input parameter to calculate a cost function such as the stress concentration factor in the panel. Later a new set of approximations is created by the process of selecting individuals according to their level of fitness in the problem domain. Over successive generations, the population evolves toward an optimal solution. The reproduction, crossover and mutation are the basic operators of genetic algorithm. In reproduction, the individuals are selected based on their fitness values relative to those of the population. In crossover, two individual

strings are selected randomly from the mating pool for producing a new chromosome from the existing one. In mutation, the mutation operator takes each chromosome in the offspring pool and causes diversity in the population. These three operators are repeated continuously until the optimal solution is obtained. Mostly numerical technique such as Finite element analysis is preferred for generating the initial population for GA based optimization.

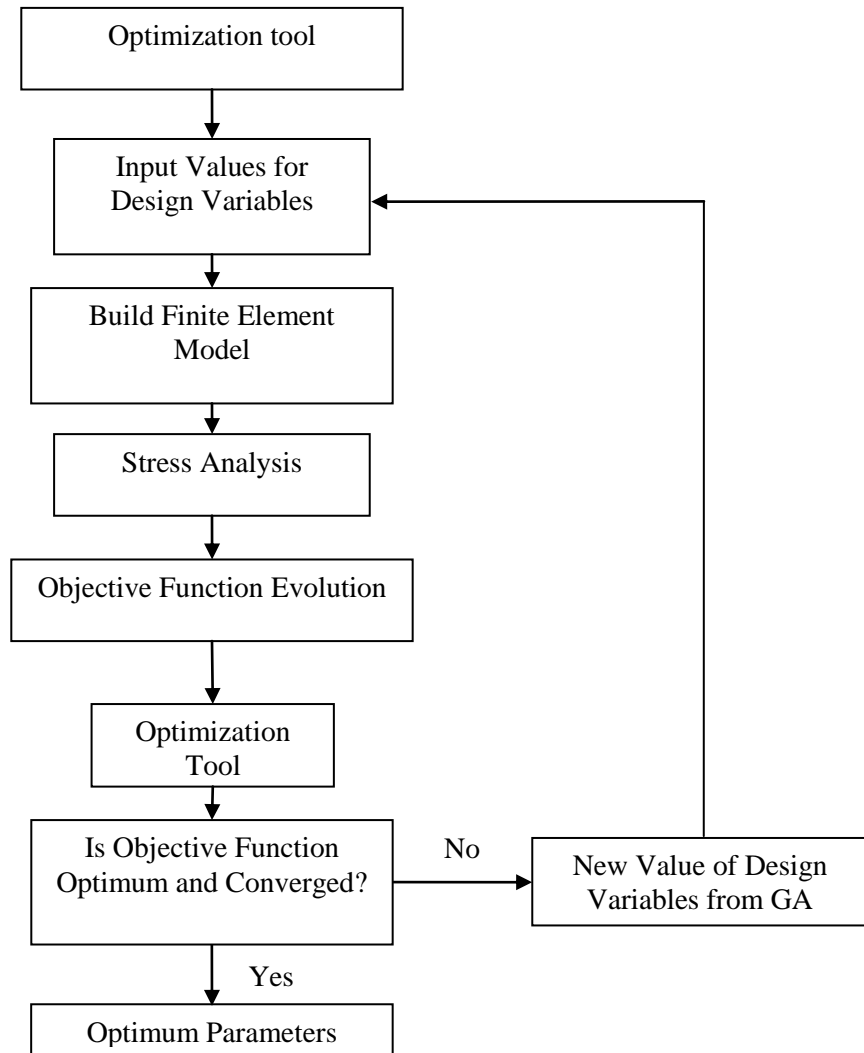


Fig. 2.3 Flowchart of optimization using genetic algorithm in-conjunction with FEA

The optimization problem can be stated as

$$\begin{aligned}
 &\text{Minimize} && f(x) \\
 &\text{Subjected to} && x_i^L \leq x_i \leq x_i^U, \quad i = 1, 2, 3, \dots, n
 \end{aligned}
 \tag{2.1}$$



where  $f(x)$  is the objective function,  $x$  are the design variables and  $x_i^L$  and  $x_i^U$  are lower and upper bound on the design variables. The lower and upper bound of design variables are obtained from mechanics based study to enable faster convergence. To obtain maximum repair efficiency, SCF should be minimized which is considered as an objective function. The patch thickness, diameter and adhesive thickness are the design variables. The optimization scheme implemented in the present study is represented by a flowchart as given in Fig. 2.3. The optimization study is carried out by developing an interface between optimization tool box in MATLAB and FEA software ANSYS 13. The optimization process starts with assigning the initial value of the variables. These parameters are read in APDL (Ansys Parametric Design Language) and then stress analysis is performed to evaluate SCF. The SCF value is read back into optimization algorithm and then solution optimality and convergence criteria are checked. If the solution is optimal and convergence criteria are met the program exit out of the loop and the design variables and convergence history are plotted. Otherwise it keeps repeating until convergence is obtained.

## **2.5 Experimental Study**

### **2.5.1 Specimen Fabrication**

The CFRP laminated sheets (300mm x 350 mm) are fabricated in house using hand-layup molding technique. Unidirectional carbon fiber of weight 200 g/m<sup>2</sup> supplied by Golbond® is used. The epoxy resin system is of LY556 and hardener is HY951 (supplied by Huntsman). The resin and hardener is taken in the proportion of 10:1 by weight. The resin and hardener is mixed at room temperature for about 25 minutes with precaution taken to avoid formation of any air bubbles. The mylar film is placed on the top of the mold to obtain highly finished CFRP sheets. The mixture is then poured onto the mold and layer of carbon fiber is then placed in required direction and squeezed in fiber direction with the help of teflon roller for removing excess resin for achieve its the required thickness. The composite panel is then left to cure for 24 hours at room temperature. The fiber volume fraction in the laminate is about 35%. Initially specimens are cut from the molded sheets to over dimensions using abrasive cutoff wheel mounted on hand-held saw. Finally, all the specimens are machined to the exact dimensions using milling machine with carbide coated end mill cutter to avoid delamination and having good surface finish. The geometry of the test specimen is shown in Fig. 2.1. To simulate the damage removal process, a circular hole of diameter ( $D = 10$  mm) is drilled at the center of the specimens using diamond coated drill at a speed of 500 rpm. A wooden backing plate is used to prevent the delamination from the back side of the specimens. The

circular patches are also fabricated from parent panel material with a stacking sequence of  $[45/-45]_s$ . The sequence is obtained on the basis of optimization. The patches are first cut into octagon shape slightly over dimension and finally polished into circular shape of 40 mm diameter, giving an overlap length of 15 mm. The bonding area of panel and patch are roughened using 220 grid sand paper and cleaned thoroughly with isopropyl. The panel and patch is bonded together using adhesive (Araldite 2011 from Huntsman) and it is then allowed to cure in room temperature for 24 hours with some dead weight over the patch. It is two part adhesive system and it is applied by an applicator gun to ensure through mixing and uniform mixing. Aluminum tabs of dimensions (50 x 50 x 2 mm) are bonded symmetrically on each end of the specimen. The specimen fabrication process is shown in Fig. 2.4.

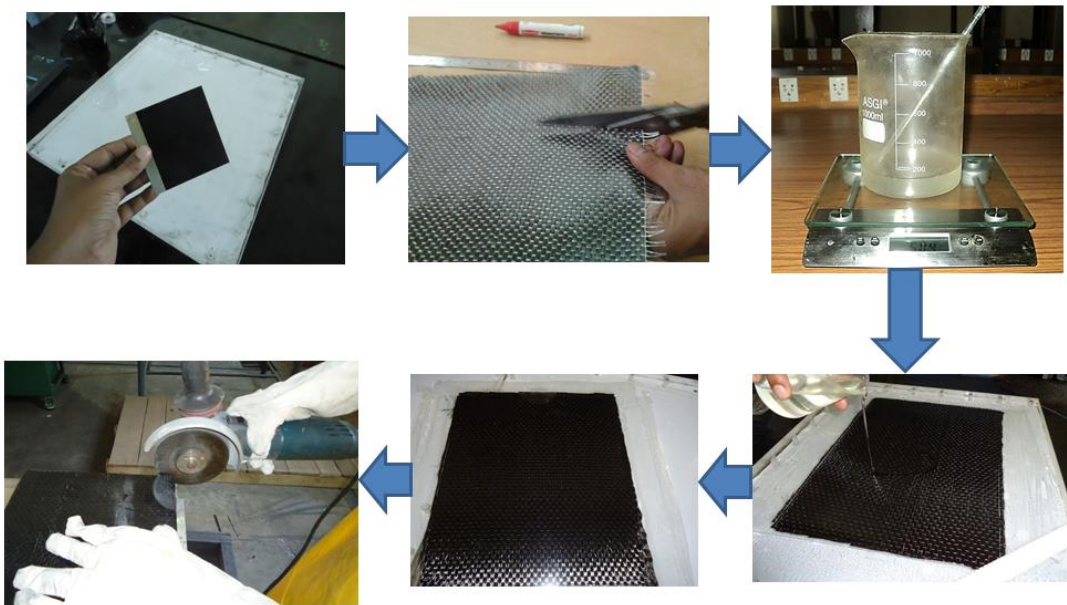


Fig. 2.4 Specimen fabrication process

## 2.5.2 Experimental Setup and Procedure

The typical experimental setup used in the present study is shown in Fig. 2.5. It consists of a computer-controlled MTS Landmark® servo-hydraulic cyclic testing machine of 100 kN capacity and a 3D DIC setup (supplied from Correlation Solutions, Inc.). The 3D DIC system comprises of a pair of CCD cameras having a spatial resolution of 2448 x 2048 pixels coupled with Schneider Xenoplan lenses of 35 mm focal length. Light emitting diode of 20 watt is used as the light source and a portable laptop with image grabbing card is employed for image acquisition. Prior to the testing, the surface of the test specimens are coated with thin layer of white acrylic paint and over sprayed with carbon black paint using air brush to obtain a random speckle pattern. The specimen is fixed into the self-adjusting

hydraulic grips at a pressure of 4 MPa. The stereo vision system is then calibrated using planar dot grid pattern plate for its position and orientation. Uniaxial tensile load is applied on the specimens in displacement control mode at a rate of 0.5 mm/min and images are continuously grabbed at a rate of 5 frames per second using the image acquisition system Vic-Snap got from Correlated Solutions. In order to ensure one-to-one correspondence between the grabbed image and applied load, an additional data acquisition card is employed providing an interface between MTS controller and image grabbing system. The images acquired by the stereo vision system are analyzed using the Vic-3D software to obtain whole field surface strain of the specimen.

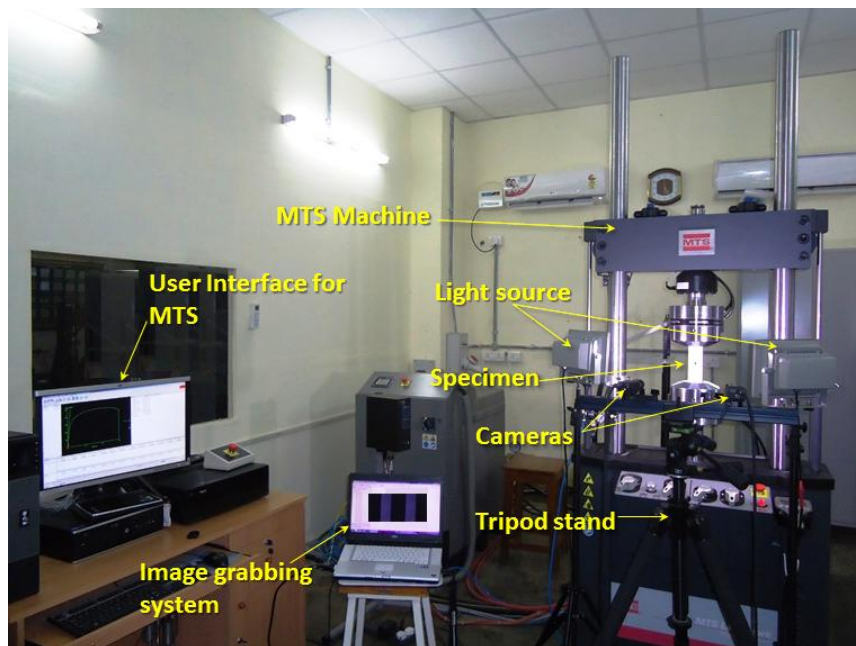


Fig. 2.5 Experimental setup comprising of MTS equipment along with 3D DIC system

## 2.6 Results and Discussion

### 2.6.1 Numerical Results

#### 2.6.1.1 Mesh Convergence Study

Firstly, a mesh convergence study is performed for the circular cutout panel to arrive at appropriate number of elements. The variation of maximum longitudinal stress with respect to number of elements along the circumference of hole is shown in Fig. 2.6. The number of elements around the circumference of hole is varied from 16 to 192. It can be observed from the figure that the magnitude of longitudinal stress increases initially and then steadily decreases with increasing number of elements along hole periphery. After 96 elements there

is not much change in the magnitude of longitudinal stress. Based on the convergence 96 elements around the hole periphery is considered for further analysis. As mentioned in the previous section the models are built with this number.

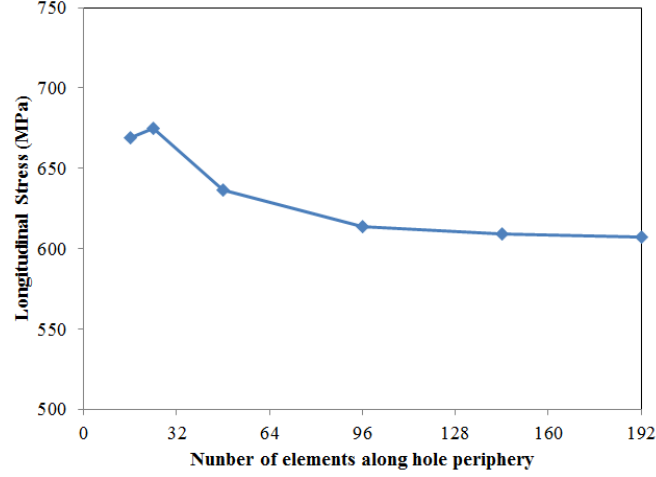


Fig. 2.6 Longitudinal stress ( $\sigma_{xx}$ ) versus number of elements along the hole periphery for mesh convergence study

### 2.6.1.2 Comparison between Theoretical and Numerically obtained SCF in a Circular Cutout panel

At first a comparison between the theoretical value and the stress estimated from the FE model is carried out to validate the FE Model. Longitudinal stress ( $\sigma_{xx}$ ) at any point on y-axis along the net-section of circular cutout panel having infinite width is given by Lekhnitskii's and is taken from Ref. [53]:

$$\sigma_{xx}(0, y) = \frac{\sigma_0}{2} \left\{ 2 + \left(\frac{r}{y}\right)^2 + 3\left(\frac{r}{y}\right)^4 - (1+n-3) \left[ 5\left(\frac{r}{y}\right)^6 - 7\left(\frac{r}{y}\right)^8 \right] \right\} \quad (2.2)$$

( $y > r$ ) where  $n$  is obtained by,

$$n = \sqrt{2 \left( \frac{E_{11}}{E_{22}} - 2\nu_{12} \right) + \frac{E_{11}}{G_{12}}} \quad (2.3)$$

At the hole boundary ( $y = r$ ) stress concentration factor is given by,

$$k_t = \frac{\sigma_{xx}(0, r)}{\sigma_o} = 1 + n \quad (2.4)$$

Fig. 2.7 shows the comparison of analytically obtained longitudinal stress versus FEA value along the net-section of open cutout panel for pure UD configuration. Looking at the plot, one can see that normal stress peaks at the hole edge as expected and it subdues as one moves away from the hole towards the panel edge. It can also be observed from the figure that stresses from both analytical and finite element have a similar trend and they are in good agreement. The SCF value obtained from the FE model is 7.32 whereas from analytical it is 7.30 thereby confirming the adequacy of the mesh considered. Such high SCF values are reported in case of pure UD panel [54]. For the FE model SCF is evaluated using Eq. (2.5) and it is the ratio of maximum stress near the hole to the applied stress as given below:

$$SCF = \frac{(\sigma_{xx})_{\max}}{\sigma_0} \quad (2.5)$$

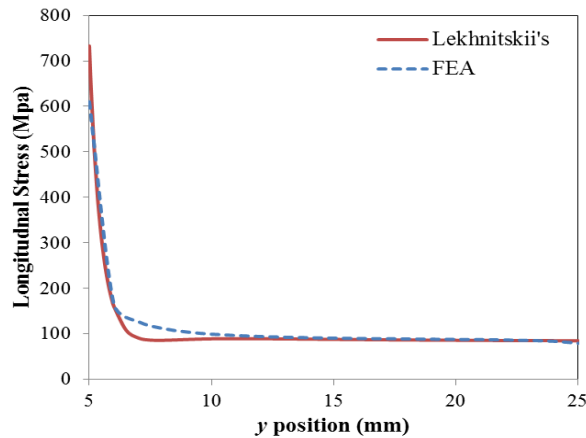


Fig. 2.7 Comparative plot of analytically obtain longitudinal stress versus finite element values along the net-section of circular cutout panel

### 2.6.1.3 Damage prone locations in Externally Bonded Patch Repair

In this sub-section, high stress locations in panel, patch and adhesive are located using FEA. The stress distribution in open cutout and repaired panel reveals that stress along the loading direction ( $\sigma_{xx}$ ) is the primary stress component inducing damage. Fig. 2.8 shows the stress variation in panel, patch and adhesive layer for the repaired configuration at a load of 10 kN (83.33 MPa). From Fig. 2.8(a), it can be observed that at two critical locations (A, B) high

stress levels are present in the panel. Zone A is the transverse edge of the hole and zone B is the longitudinal edge of the patch. By closely observing Fig. 2.8(b), it is found that zone C (overlap edge) is one of the most critical location on the adhesive layer from which damage could initiate in the form of patch debonding. Fig. 2.8(c) reveals that  $\sigma_{xx}$  stress component in the patch is higher at the hole edge (Zone D). These locations are always referred in the subsequent sections for a quantitative study.

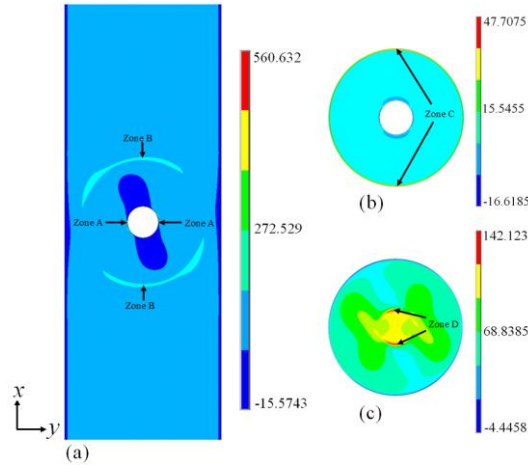


Fig. 2.8 Whole field stress contour plots of various components in externally bonded double sided repair from 3D FEA (a) longitudinal stress ( $\sigma_{xx}$ ) in repaired panel (b) peel stress ( $\sigma_{zz}$ ) in adhesive (c) longitudinal stress ( $\sigma_{xx}$ ) in patch

#### 2.6.1.4 Mechanics Based Design Approach

In this section, mechanics based design approach is studied elaborately involving FEA. The damaged panel with circular cutout is repaired with a double sided circular patch having different patch stacking sequence, patch thickness, patch diameter and adhesive thickness. The effect of these parameters on SCF of the repaired panel is analyzed before and after the repair and then suitable recommendations are given. Also the shear stress levels in the adhesive layer are included as part of this study.

##### 2.6.1.4.1 Effect of Patch Stacking Sequence on Repaired Panel

The variation of SCF at Zone A and normalized shear stress ( $\tau_{xz}$ ) in adhesive layer for the panel containing a circular cutout repaired with double and single sided patch having different stacking sequences are presented in Table 2.2. In this study adhesive thickness, patch thickness and patch diameter are 0.1, 1.2 and 40 mm respectively and they are kept fixed. In case of double sided repair, it is found that the SCF is lower while normalized shear stress is maximum for the patch stacking sequence of  $[0]_4$ . In case of  $[45/-45]_s$  layup, SCF is intermediate but shear stress is comparatively minimum and for  $[45/-45/0/90]$  configuration

SCF is minimum but shear stress is intermediate. Therefore patch layup of  $[45/-45]_s$  and  $[45/-45/0/90]$  are considered for double sided repair. Similar observation is made in the experimental study given in Ref. [23]. In case of single sided repair, SCF is minimum but shear stress is higher for the patch configuration  $[90]_4$  but in contrast to this SCF is intermediate and shear stress is minimum for a patch stacking sequence of  $[0]_4$ . Therefore, patch configuration of  $[45/45]_s$  and  $[45/-45/0/90]$  are considered for double sided repair and  $[90]_4$  lay up is considered for the single sided repair case.

Table 2.2 SCF and normalized shear stress values obtained for models different patch stacking sequences

Name	Patch stacking sequence	Stress concentration factor		Normalized shear stress	
		Single sided	Double	Single sided	Double
A	$[0]_4$	5.7207	2.6143	0.2391	0.3530
B	$[90/0/-45/45]$	5.8870	2.6143	0.2505	0.2530
C	$[0/90/45/-45]$	5.7340	2.6143	0.26	0.2859
D	$[45/-45/0/90]$	5.9622	2.6143	0.2693	0.2594
E	$[45/-45]_s$	6.1749	3.7934	0.2575	0.2000
F	$[90]_4$	5.5515	4.2345	0.2614	0.2074

#### 2.6.1.4.2 Effect of Patch Thickness on Repaired Panel

Figure 2.9 shows the variation of SCF at zone A and B on the first layer ( $45^\circ$  to loading direction) in the panel for different patch thickness in the case of double sided repair. The patch stacking sequence used here is  $[+45/-45]_s$ . Initially most severe location is zone A but on increasing patch thickness it shifts towards zone B which may lead to skin damage on the panel. For a minimum SCF at both the locations, corresponding patch thickness is obtained as shown in Fig. 2.9. The thickness of the patch is found to be 1.3 mm. Also, the variation of SCF (at zone A in  $0^\circ$  layer) and normalized shear stress (in the adhesive layer) for a double sided repair model with the patch thickness is shown in Fig. 2.10. Looking at the plot, one could see that SCF decreases with patch thickness but shear stress in adhesive layer increases. On close observation of the plots, patch thickness of 1.3 mm leads to a lower SCF and an intermediate level of shear stress in the adhesive layer.

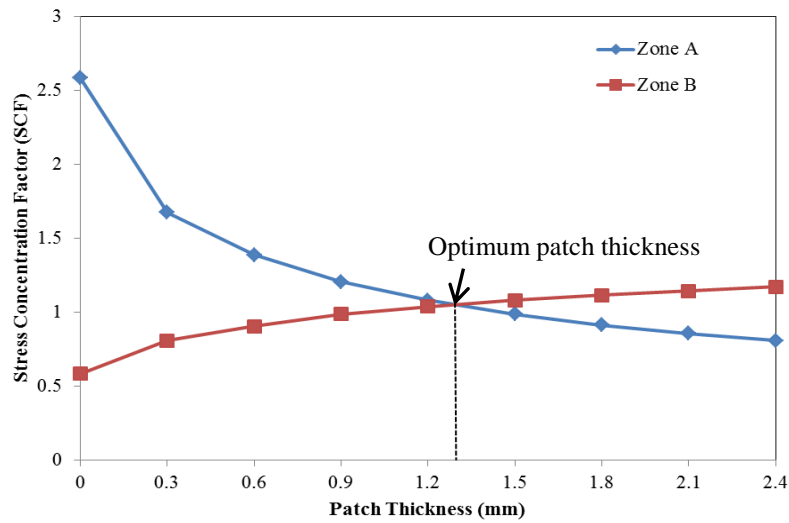


Fig. 2.9 Variation of SCF in Zone A and B of panel with varying patch thickness

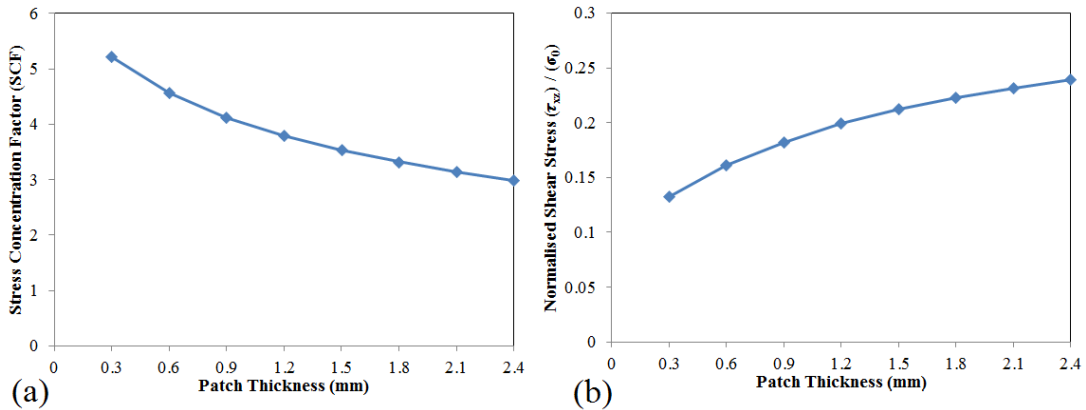


Fig. 2.10 Variation of SCF and normalized shear stress with different patch thickness (adhesive thickness 0.15 mm) (patch diameter 40 mm)

### 2.6.1.4.3 Effect of Adhesive Layer Thickness on Repaired Panel

Adhesive layer plays an important role in the structural integrity of a repaired panel. The peel ( $\sigma_{zz}$ ) and shear ( $\tau_{xz}$ ) stress in the adhesive layer are the primary stress components responsible for patch debonding from the panel. In this section, the effect of adhesive thickness on shear stress as well as SCF is studied because the thickness of adhesive layer influences its behaviour. In case of higher adhesive thickness it becomes porous weakening the interface. However, for lower adhesive thickness it becomes more stiff and brittle [55]. The variation of SCF at zone A and normalized shear stress in adhesive layer for a double sided patch repaired panel ([45/45]<sub>s</sub> layup) with adhesive thickness is shown in the Fig. 2.11. From the plot, it can be observed that with increase in thickness adhesive shear stress decreases but SCF increases. Higher adhesive thickness strengthens adhesion but it weakens



the load transfer towards the patch thereby decreasing the beneficial effect of the patch resulting in increase of SCF. On the other hand, lower adhesive thickness supports the load transfer towards the patch but increases the risk of adhesive layer failure [56]. Figure 2.12 shows the variation of adhesive shear stress with overlap length for different adhesive thickness of 0.05, 0.1, 0.15, 0.2, 0.25 (all are in mm). From the graph it can be observed that shear stress distribution in thin and thick adhesive is almost same but there is a drastic reduction of shear stress at the overlap edge (zone C) with increasing adhesive thickness. At this zone load transfer occurs from the panel to patch and therefore it gets highly stressed while rest of the layer is of low stress. By looking at the plots, an adhesive thickness of 0.15 mm gives an intermediate SCF as well as shear stress level.

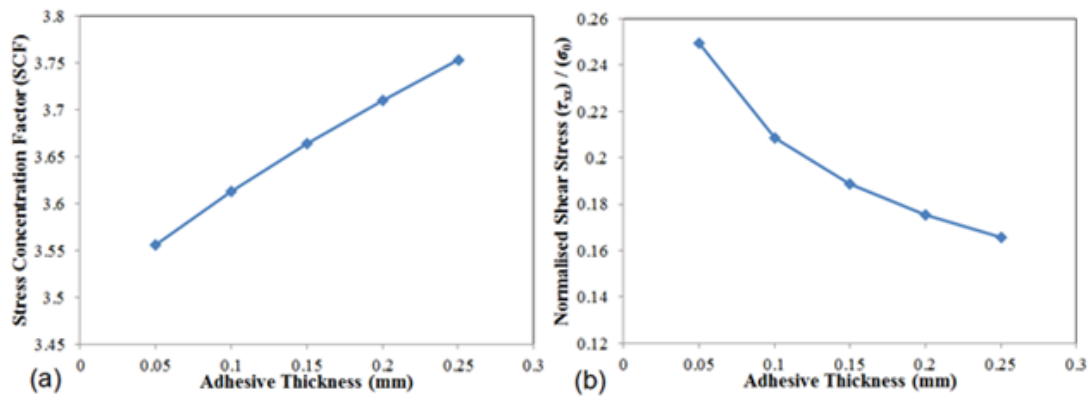


Fig. 2.11 Variation of stress SCF and normalized shear stress with adhesive thickness for double sided repair (patch diameter 40 mm)

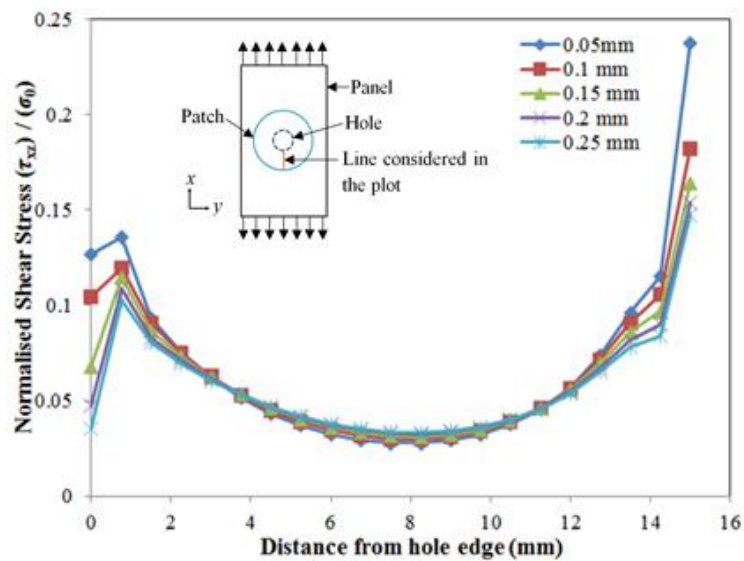


Fig. 2.12 Variation of shear stress ( $\tau_{xy}$ ) along the longitudinal axis repaired with different adhesive thickness

### 2.6.1.4.4 Effect of Patch Diameter on Repaired Panel

Fig. 2.13a shows the SCF variation at the transverse edge of the hole with patch diameter and Fig. 2.13b shows variation of normalized shear stress in the adhesive layer with patch diameter. Patch stacking sequence considered here is  $[45/45]_s$ . It is evident that SCF and shear stress levels are inversely proportional to patch diameter. As the patch diameter increases, the SCF and shear stress reduces. Load transfer area from panel to patch increases with increase in patch area and therefore higher load is transferred by the patch leading to significant reduction in SCF. This trend is observed up to the patch diameter of 40 mm and it remains same beyond it. A similar trend is also seen in case of shear stress in the adhesive layer. Fig. 2.14 shows the distribution of normalized shear stress in adhesive layer with respect to the overlap length for different patch diameters. On careful observation, the patch with larger diameter shows greater reduction of shear stress along the overlap length but after 40 mm diameter there is not much reduction in shear stress at patch overlap edge. Therefore, one can conclude from Fig. 2.13 and 2.14 that over stiff patches are dangerous as they will induce high peel and shear stresses in the adhesive layer. Therefore, a patch diameter of 40 mm is chosen to reduce both SCF and shear stress in the adhesive layer towards an integral repair system.

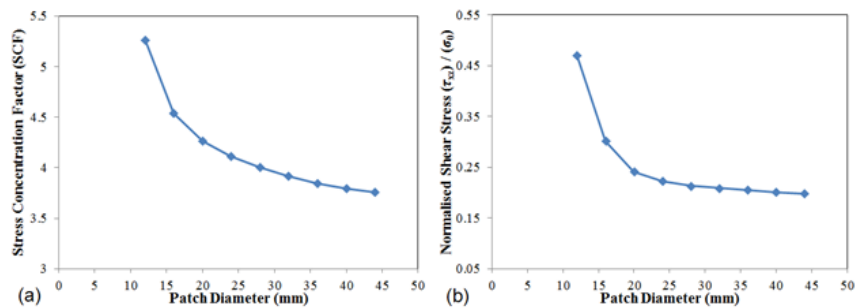


Fig. 2.13 Variation of SCF and normalized shear stress with varying patch diameter

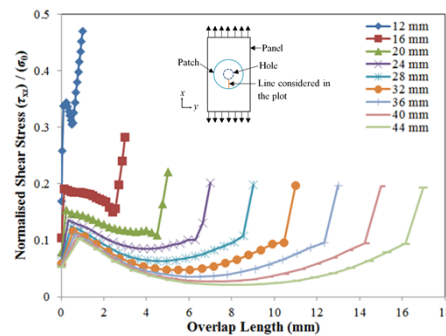


Fig. 2.14 Variation of normalized shear stress  $(\tau_{xz})$  along the longitudinal axis for different patch diameter

#### 2.6.1.4.5 Comparison of Open Cutout and Repaired Panel

Comparison of SCF values between open cutout and repaired (single and double sided) panel is shown in Table 2.3. The mesh morphology for open cutout, single sided and double sided repaired panel is retained same for quantitative comparison. The patch stacking sequence is  $[45/-45]_s$ . From the table one can observe that, in case of double sided repair there is a drastic reduction in SCF as compared to single sided repair. This is because there is a slight shift in neutral axis towards the patch in case of single sided repair, leading to bending effect in addition to in-plane loading. For quantitative comparison same patch dimensions are considered for both single and double sided repair panels. The SCF is reduced from 6.33 to 3.70 in case of double sided repair whereas for single sided repair it is 5.94. Based on SCF reduction one can emphasize that double sided repair is more efficient as compared to single sided repair.

Table 2.3 SCF comparison between open cutout, single sided and double sided repair model

Design Parameters	Open cutout panel	Single sided repair	Double sided repair
SCF	6.33	5.94	3.71

#### 2.6.2 Optimization using Genetic Algorithm Approach

The influence of patch geometry and adhesive strength on repair performance of quasi-isotropic laminate is investigated using mechanics based approach in the previous section. Based on the study it is found out that patch thickness, diameter and adhesive thickness have more influence on repair efficiency than any other factors. Determined patch parameter values from mechanics based design approach are not optimum and in reality one has to obtain the optimum value of all these parameters in one go using a regular optimization technique so that the maximum performance can be achieved. In this section, GA in conjunction with FEA is used for arriving at the optimum patch dimension as well as adhesive thickness applied to repair of quasi-isotropic laminate of  $[45/-45/0/90]_s$  configuration. The recommended patch layup is  $[45/-45]_s$  configuration for the circular shape. To obtain maximum repair efficiency, SCF should be minimized and it is considered as an objective function in the present study. The patch thickness ( $t_p$ ), adhesive thickness ( $t_a$ ) and diameter of patch ( $D_p$ ) are three different design variables considered. The lower and upper bound of design variables obtained from FEA and the GA parameters used in

optimization algorithm are summarized in Table 2.4. In this study convergence is attained when the average change in the fitness value is less than the function tolerance ( $1e-4$ ). The convergence history of fitness value (objective function) with number of generation is shown in Fig. 2.15. It is observed here that the convergence is achieved after fifty one generations. The SCF for panel with optimized patch geometry is found to be 3.652 as compared to 6.33 when unrepaired. The optimum patch parameters obtained from GA approach are given in Table 2.5. It is found that the optimum value of the repair parameters obtained from GA approach is closer to the ones predicted from mechanics based approach.

Table 2.4 Parameters used in the GA optimization scheme

<b>GA-parameters</b>		
Population size		20
Elite size		2
Crossover fraction		0.8
Selection scheme		Tournament
Crossover scheme		Heuristic
Mutation scheme		Adaptive feasible
<b>Design Parameters</b>		
	<b>Lower bound</b>	<b>Upper bound</b>
Patch thickness ( $t_p$ ) in mm	0.4	2
Patch diameter ( $D_p$ ) in mm	11	46
Adhesive thickness ( $t_a$ ) in mm	0.05	0.25

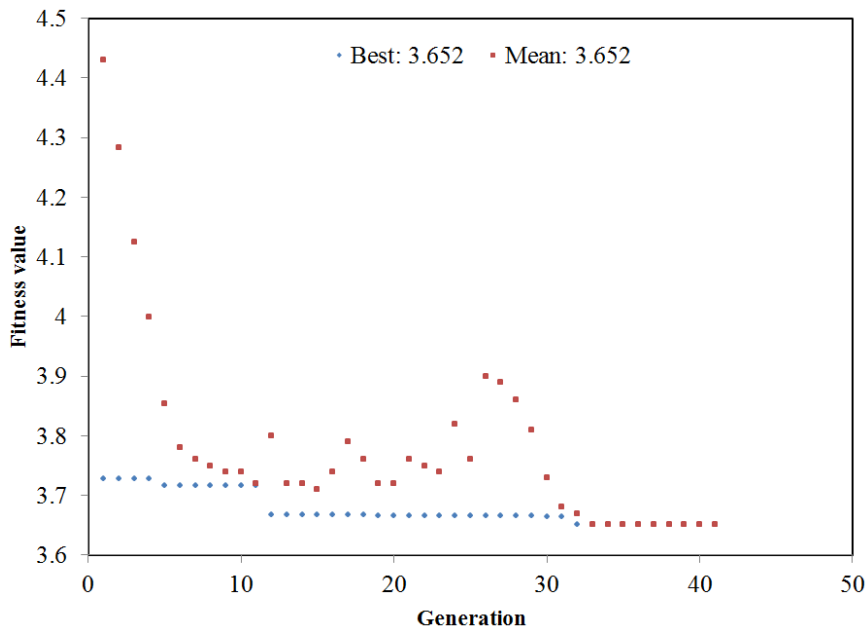


Fig. 2.15 Convergence plot for GA algorithm

Table 2.5 Optimized repair parameters from genetic algorithm

<b>Design Parameters</b>	<b>Optimum value</b>
Patch thickness ( $t_p$ )	1.36 (mm)
Patch diameter ( $D_p$ )	40.8 (mm)
Adhesive thickness ( $t_a$ )	0.13 (mm)

### 2.6.3 Experimental Results

Experimental results obtained from the tensile test of circular cutout panel, single sided repair and double sided repair panel obtained using DIC is presented in this section.

#### 2.6.3.1 Whole Field Strain Pattern Obtained from 3D DIC

##### 2.6.3.1.1 Circular Cutout Panel

The circular cutout panel having a stacking sequence of  $[45/-45/0/90]_s$  subjected to uni-axial tensile load is analyzed using whole-field experimental technique of digital image correlation. For the DIC study, a rectangular area of size 46.8 mm x 134 mm around the hole is chosen as the region of interest (ROI). A subset size 27 x 27 pixels is chosen along with a grid step size of 7 pixels for performing DIC estimation. Fig. 2.16 shows the whole field strain distribution over damaged panel at different load levels. It can be observed from figure that the  $\varepsilon_{xx}$  distribution is not perfectly symmetrical about central axis. The asymmetry in the strain distribution is mainly due to asymmetrical damage accumulation around the hole because of 45° surface ply. The damage development in circular cutout panel starts with 90° matrix cracking from the highly strained zone at the hole boundary as well as matrix crack in 45° surface ply across the width of specimen. The final failure in circular cutout panel involves 0° fiber splitting along with local delamination and fiber pullout. The final failure is at load of 32.57 kN and it is very sudden and it corresponds to a strength of 271.42 MPa. The corresponding tensile strength of the virgin panel measured at an equivalent displacement rate is 437.5 MPa (52.5 kN). The reduction in tensile strength due to circular cutout in panel is 38.74 %.

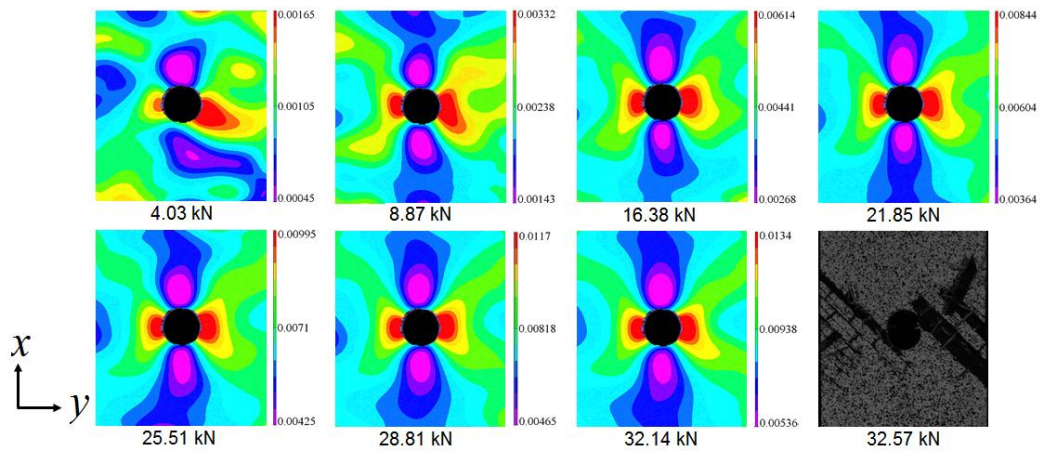


Fig. 2.16 Whole field strain ( $\epsilon_{xx}$ ) distribution of a circular cutout panel under tensile load

### 2.6.3.1.2 Single Sided Repair Panel

The circular cutout panel of stacking sequence  $[45/-45/0/90]_s$  repaired with single sided patch having layup  $[45/-45]_s$  subjected to uni-axial tensile load is analyzed here. Uncorrelated region is observed around the patch edge due to shading and sudden change in depth between patches and panel planes. Fig. 2.17 shows the whole field strain distribution ( $\epsilon_{xx}$ ) over single sided repair panel at different load levels. From the figure, one can observe that the maximum strain value is at upper and lower edge of the patch along loading direction. The strain field predicted by DIC for the single sided repair panel under tensile loading is similar to that described by Caminero et al. [24]. Highly localized strain at the patch edge induces the skin damage to the panel as well as initiates the patch debonding due to peeling effect. As load increases, localized strain zone shifts towards the upper patch edge and patch debonding initiates from this zone. The patch debonding occurs at a load of 35.50 kN corresponding to 295.83 MPa. After patch debonding, final failure of the panel involves complex fracture mechanism involving matric cracking, delamination and fiber fracture.

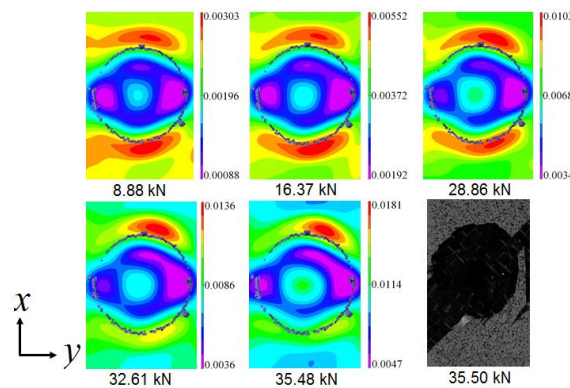


Fig. 2.17 Whole field strain ( $\epsilon_{xx}$ ) distribution of a single sided repair panel under tensile load

### 2.6.3.1.3 Double Sided Repair Panel

The circular cutout panel of stacking sequence  $[45/-45/0/90]_s$  repaired with double sided patch having layup  $[45/-45]_s$  subjected to uni-axial tensile load is analyzed using DIC to assess the damage till final failure. Fig. 2.18 shows the whole field strain distribution ( $\epsilon_{xx}$ ) over double sided repair panel at different load levels. From the figure, one can observe that maximum strain value ( $\epsilon_{xx}$ ) is at upper and lower edge of the patch along  $x$ -direction and at center of the patch over the hole at a load value of 8.9 kN. As the load increases high strain zone gets shifted to the upper edge of the patch. It can be seen from the figure that damage initiates from the highly strained zone at the upper edge of the patch. Complete failure of double sided repair panel happens at a load of 42.23 kN corresponding to 351.92 MPa. Patches are partially separated from the panel but it doesn't completely debond unlike single sided repair. The damage mechanism for the double sided repair panel is very similar to that described by Pencheng et al. [23]. Final failure of the panel predominantly involves matrix cracking and delamination from both transverse sides of the hole.

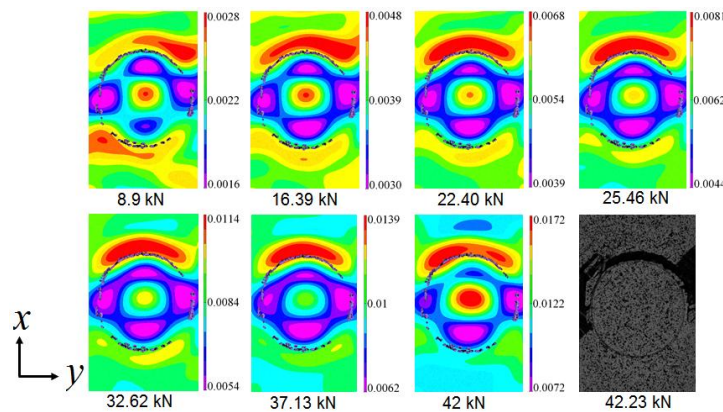


Fig. 2.18 Whole field strain ( $\epsilon_{xx}$ ) distribution of a double sided repair panel under tensile load

### 2.6.3.2 Failure Mechanism of Open Cutout and Repaired Panel

The final failure mechanism observed in open cutout and repaired panel (single and double sided repair) is shown in Fig. 2.19. It can be confirmed that various failure modes are present in open cutout and repaired panel such as matrix cracking, fiber splitting and fiber fracture etc. Both  $90^\circ$  and  $45^\circ$  matrix cracking initiate from highly strained zone around the transverse edge of the hole. It is evident from the figure that the failure mechanism in single and double sided repair is similar to open cutout panel. In single sided repair panel, debonding of the patch initiates from the overlap edge of patch due to adhesive layer breakdown at this zone due to high peel stress development. This is because of additional bending stress coming in the case of single sided repair. The final failure of single sided repair panel takes place with

complete debonding of patch from parent panel followed by panel failure identical to that of open cutout panel. It can be observed that some of the parent panel material remains bonded with the patch after failure. In double sided repair panel, failure gets initiated from transverse edges of the hole in the parent panel and partially detaching of patches from the top overlap edge. It happens as the damage accumulates at the transverse edge of the hole and then propagates across the panel. The patches remain intact with the parent panel.

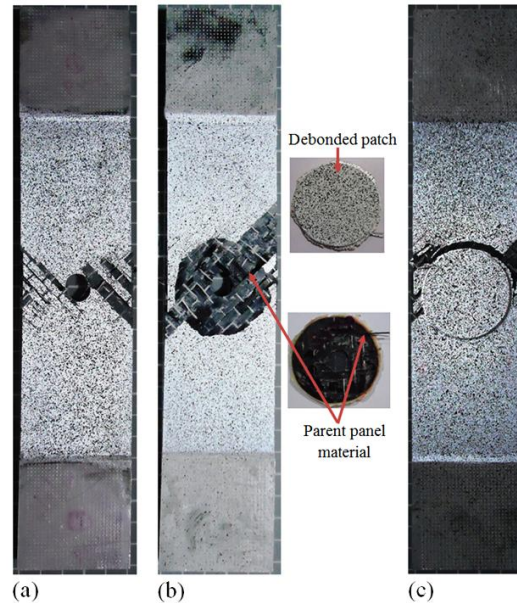


Fig. 2.19 Failure mechanism in  $[45/-45/0/90]_s$  panel under tensile load (a) open cutout panel (b) single sided repaired panel (c) double sided repaired panel

### 2.6.3.3 Comparison of DIC Results with FEA Analysis

A 3D finite element analysis is also carried out to compare the strain values with those obtained from the DIC. Both qualitative and quantitative strain comparison is done between DIC and FEA result.

#### 2.6.3.3.1 Circular Cutout Panel

The full-field strains on the specimen surface (+45 ply) corresponding to a load of 10 kN (83.33 MPa) predicted from DIC and FEA are compared in Fig. 2.20. For the illustrative purpose, the FEA plots are shown with adjusted scale similar to DIC. Looking at the strain plot, it is clear that the normal strain field ( $\epsilon_{xx}$ ) obtained from FEA is consistent with those from DIC experiment. Also the magnitude of strain is very high near the transverse edge of the hole (zone A) similar to that of DIC result. The contour plot of shear strain  $\epsilon_{xy}$  obtained from both DIC and FEA is compared in Fig. 2.20(d)-(f). There exists a good correlation



between DIC and FEA results. A similar observation has been reported in Ref. [25]. Fig. 2.21 shows the variation of  $\epsilon_{xx}$  value on the surface (+45 ply) obtained from both DIC and FEA along the net-section of the panel for a load of 10 kN. It is maximum at hole edge and subdues as one goes away from hole towards panel edge. Besides small difference in magnitude,  $\epsilon_{xx}$  distribution from both DIC and FEA has a similar trend and relatively shows a good agreement.

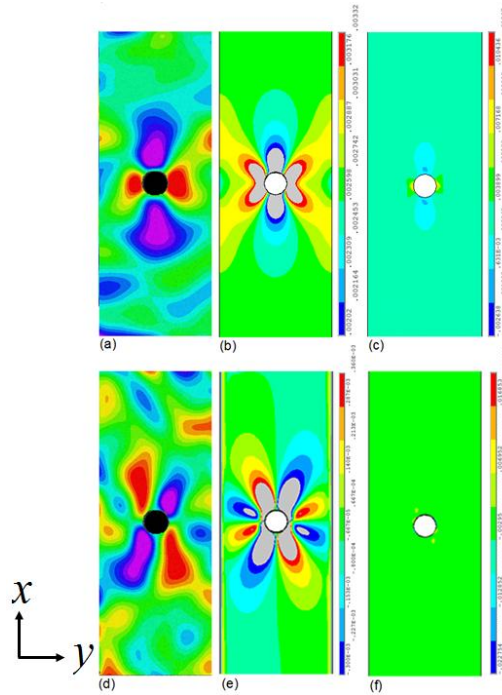


Fig. 2.20 Comparison of whole field strain contour obtained from DIC and FEA for open cutout panel under tensile load of 10 kN (a) DIC (b) FEA (ADS) (c) FEA (AS) -  $\epsilon_{xx}$  plot (d) DIC (e) FEA (ADS) (f) FEA (AS) -  $\epsilon_{xy}$  plot (ADS – adjusted scale of FEA with DIC scale, AS - Actual scale of FEA plot)

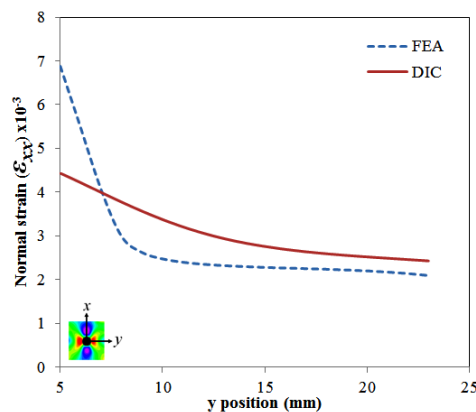


Fig. 2.21 Comparative line plot of  $\epsilon_{xx}$  between DIC and FEA along the net-section of open cutout panel

### 2.6.3.3.2 Single Sided Repair Panel

Comparison of contour plots of  $\varepsilon_{xx}$  and  $\varepsilon_{xy}$  for the single sided repaired panel corresponding to a load of 10 kN obtained from FEA and DIC are shown in Fig. 2.22. The DIC plot of  $\varepsilon_{xx}$  strain field (as shown in Fig. 2.22(a)) possess highly strained zone around the upper and lower patch edge. But, contour plot from FEA shows highly strained zone along the unpatched edge of the hole. This is because unpatched side is at back side in case of DIC experiment and hence cannot be estimated. The magnitude of strain at patch edge predicted by FEA is lower than the experimental value. The contour plot of  $\varepsilon_{xy}$  obtained from DIC and FEA is shown in Fig. 2.22(d)-(f). It is found that a similar trend exists between DIC and FEA plots.

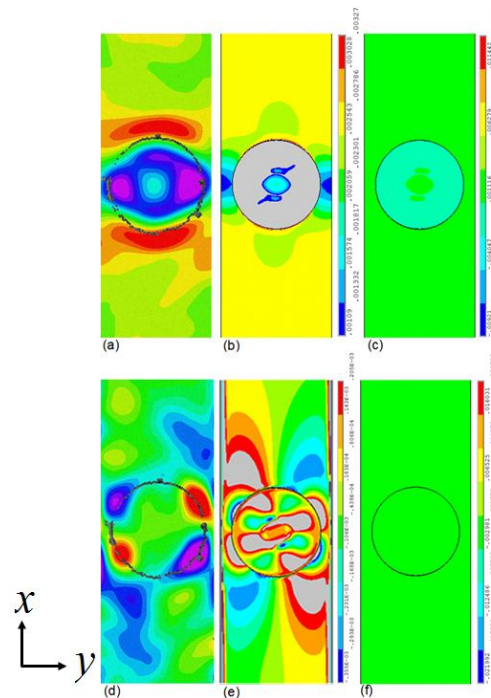


Fig 2.22 Comparison of whole field strain contour obtained from DIC and FEA for single sided repair panel under tensile load of 10 kN (a) DIC (b) FEA (ADS) (c) FEA (AS) -  $\varepsilon_{xx}$  plot (d) DIC (e) FEA (ADS) (f) FEA (AS) -  $\varepsilon_{xy}$  plot (ADS – adjusted scale of FEA with DIC scale, AS - Actual scale of FEA plot)

### 2.6.3.3.3 Double Sided Repair Panel

Comparison of contour plots of  $\varepsilon_{xx}$  and  $\varepsilon_{xy}$  for the double sided repaired panel corresponding to load 10 kN obtained from DIC and FEA are shown in Fig. 2.23. Strain  $\varepsilon_{xx}$  (as shown in Fig. 2.23(a)) possess highly strained zone around the upper patch edge. However, contour

plot from FEA shows highly strained zone around the hole edge (Fig. 2.23(b)). This deviation exists as DIC measures only surface the strain and it can't access anything below the patch. The contour plot of  $\epsilon_{xy}$  obtained from DIC and FEA is shown in Fig. 2.23(d)-(f) and they are found to be in good agreement.

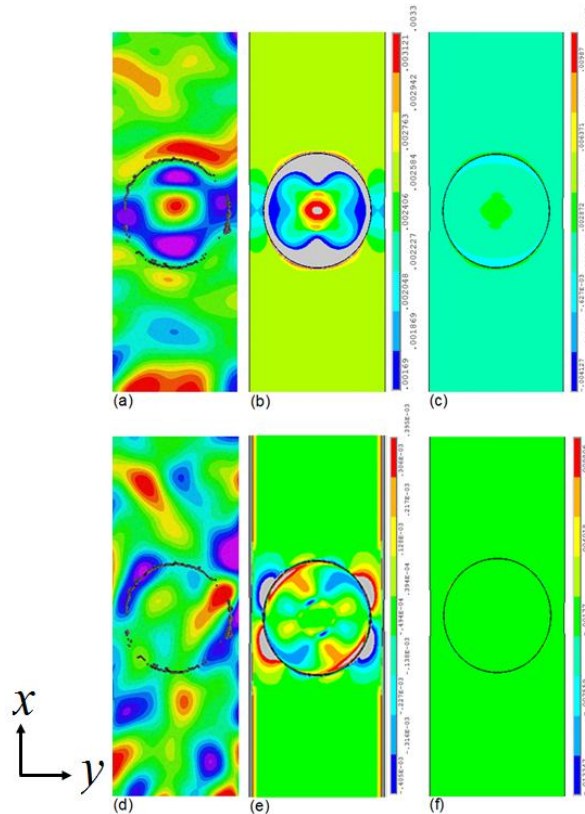


Fig. 2.23 Comparison of whole field strain contour obtained from DIC and FEA for double sided repair panel under tensile load of 10 kN (a) DIC (b) FEA (ADS) (c) FEA (AS) -  $\epsilon_{xx}$  plot (d) DIC (e) FEA (ADS) (f) FEA (AS) -  $\epsilon_{yy}$  plot (AS – adjusted scale of FEA with DIC scale, AS - Actual scale of FEA plot)

#### 2.6.3.4 Strength of Open Cutout and Repaired Panel

The ultimate strength of the virgin, open cutout and repaired panel obtained from experiment is given in Table 2.6. The ultimate tensile strength is estimated as failure load upon gross cross sectional area of the specimens. The tensile strength for virgin panel is 437.5 MPa whereas for circular cutout panel it is 271.42 MPa. In case of single and double sided repair panel it is 295.83 MPa and 351.92 MPa respectively. The percentage gain in ultimate strength in case of single and double sided repaired panel with respect to open cutout panel is 8.9 and 29.6 respectively. Therefore double sided repaired panel has got a higher strength as compared to single sided one and therefore it is recommended for repair applications.

Table 2.6 Maximum, mean and standard deviation in maximum load for open cutout and repaired specimen

<b>Design Parameters</b>	<b>Virgin panel</b>	<b>Open cutout panel</b>	<b>Single sided repair</b>	<b>Double sided repair</b>
Maximum load (kN)	53.1	33.25	36.33	42.92
Mean (kN)	52.5	32.57	35.50	42.23
Standard deviation(kN)	0.79	0.69	0.54	0.32
Standard deviation (%)	1.50	2.12	1.52	0.75

## 2.7 Closure

In this chapter, a finite element based study is carried out to understand the mechanics of composite patch repair on damaged CFRP panel of configuration [45/-45/0/90]<sub>s</sub> under tensile load. The panel is repaired with circular patch. The influence of various parameters such as patch stacking sequence, patch thickness, overlap length and adhesive thickness is investigated in case of double sided repaired panel. Design value of these parameters is arrived at for a given damaged panel to improve the repair performance using mechanics based design approach involving FEA. Later, a genetic algorithm based optimization scheme in-conjunction with FEA is then implemented for arriving at an optimized patch and adhesive dimension. Interestingly, it is found that the optimum value of the patch and adhesive parameter in case of double sided repair obtained from GA approach is closer to the mechanics based prediction. Also the same dimensions are retained for single sided repair for a quantitative comparison. Finally, a 3D DIC based experimental study is carried out with the same optimized patch geometry for comparing it with FEA results. The whole field strain pattern over open cutout and repaired panel obtained using DIC technique is compared with FEA results and they are found to be consistent.

# Chapter 3

## Study of Matrix Crack Interaction on Inclusion Using DIC and FEA

### 3.1 Introduction

The excellent properties of composite materials (high strength to weight ratio, resistance to corrosion and easy formability) have rapidly increased its application in various engineering fields like aerospace, automobile and marine. During the service life of an aircraft, it is subjected to severe structural and aerodynamic loads which results from repeated landings and take off, fatigue, ground handling, bird strikes and environmental degradation. The damage in composite material is in the form of matrix cracking, fibre breakage and debonding. The composite materials have orthotropic property which leads to complex mechanical behavior from those of conventional isotropic materials. Composite materials are very brittle in nature and while in use catastrophic structural failure may occur and can result in loss of life.

The increasing use of composites in the design of structural parts requires a special understanding; especially in the presence of a matrix crack interacting with a second phase inclusion. The stress and strain field around the crack-tip is modified due to interaction between matrix crack and inclusion. The intrinsic failure process under the influence of a pre-existing or a service induced flaw (such as a crack) can be explained by studying a simplified problem of a matrix crack interacting with the second phase which can be a fibre or a particle. Some of these variations include (a) the geometry and the size of the inclusion, (b) the orientation of the inclusion with respect to the crack, (c) the mismatch between elastic properties of the matrix and the inclusion like young's modulus and poisons ratio, (d) effects of bond strength between the inclusion and the matrix and (e) a crack interacting with multiple inclusions. The SIF can be evaluated analytically, numerically and experimentally. Most of the analytical solutions are based on highly idealized models of the component geometry and give the basic relations between the parameters affecting the fracture. Analytical closed-form solutions are available for various simple configurations. But analytical techniques are rigorous and mostly applicable for complex geometries. For complex configurations, SIF need to be extracted by experimental or numerical analysis.

The numerical methods especially FEM require precise knowledge about the boundary conditions and are required to be compared against analytical or experimental results for possible errors. The experimental methods are particularly well suited for determining SIF for specific geometry / loading conditions in situations where analytical or numerical methods fail to provide acceptable answers. Many researchers have developed and applied methodologies for estimating SIF's for crack inclusion interaction problem using different experimental techniques. These experimental techniques include whole field non-contact optical methods such as moiré interferometry, photoelasticity. Now days, digital image correlation (DIC) have become the most popular ones for SIF determination because of their relatively simple specimen preparation, ease of use and requirement of less complicated optics. Thus, digital image correlation (DIC) has been considered in this work for SIF estimation.

In this chapter, both experimental and numerical based study is carried out to evaluate mixed-mode SIF's of crack inclusion interaction specimen under tensile loading. As well as matrix inclusion debonding in the presence of a nearby crack is also addressed using 3D DIC and FEA. Figure 3.1 summarizes the general steps involved in the evaluation of fracture parameters using digital image correlation (DIC). In the present work, SIF's are estimated for three different configurations - Single edge notched (SEN) panel with single inclusion in front of crack tip, edge slant crack (ESC) panel with single inclusion in front of crack tip and Single edge notched (SEN) panel with two eccentric inclusion. In this study, a code developed using MATLAB by (Veerkar [48]) is used to estimate the SIF's from displacement field data obtained from DIC. The experimentally evaluated SIF's are compared with FE value.

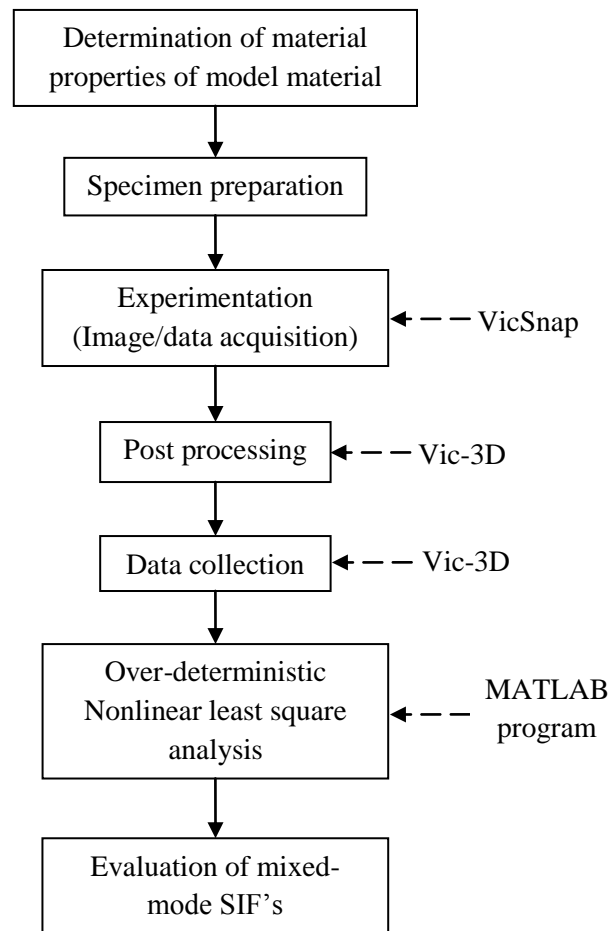


Fig. 3.1 General steps involved in the determination of mixed-mode SIF's using DIC [48]

### 3.2 Problem Description

In this study, three different specimen configurations are considered - single edge notched (SEN) panel with single inclusion, edge slant cracked (ESC) panel with single inclusion and single edge notched (SEN) panel with two eccentric inclusion. The length, width and the thickness of the panel are 200 mm, 45 mm and 6 mm respectively. Diameter of the glass inclusion is 6 mm. Epoxy specimens with three different configurations are shown in Fig. 3.2. Configuration SEN with single inclusion contains crack length of 8 mm and distance from crack tip to edge of inclusion is 6.5 mm. In case of ESC with single inclusion configuration crack length is 11.3 mm and crack angle with edge of the panel is  $45^\circ$ . Distance between crack tip to edge of inclusion is kept constant as that of SEN with single inclusion case. Configuration SEN with two inclusions contain crack length of 8 mm and distance from crack tip to edge of inclusions is 6.5 mm but they are eccentrically placed. The distance between the crack plane and the inclusion center is defined as eccentricity and

it is 9 mm. Two symmetric inclusions are placed on either side of a crack plane. All the tests are carried out under uniform tensile loading.

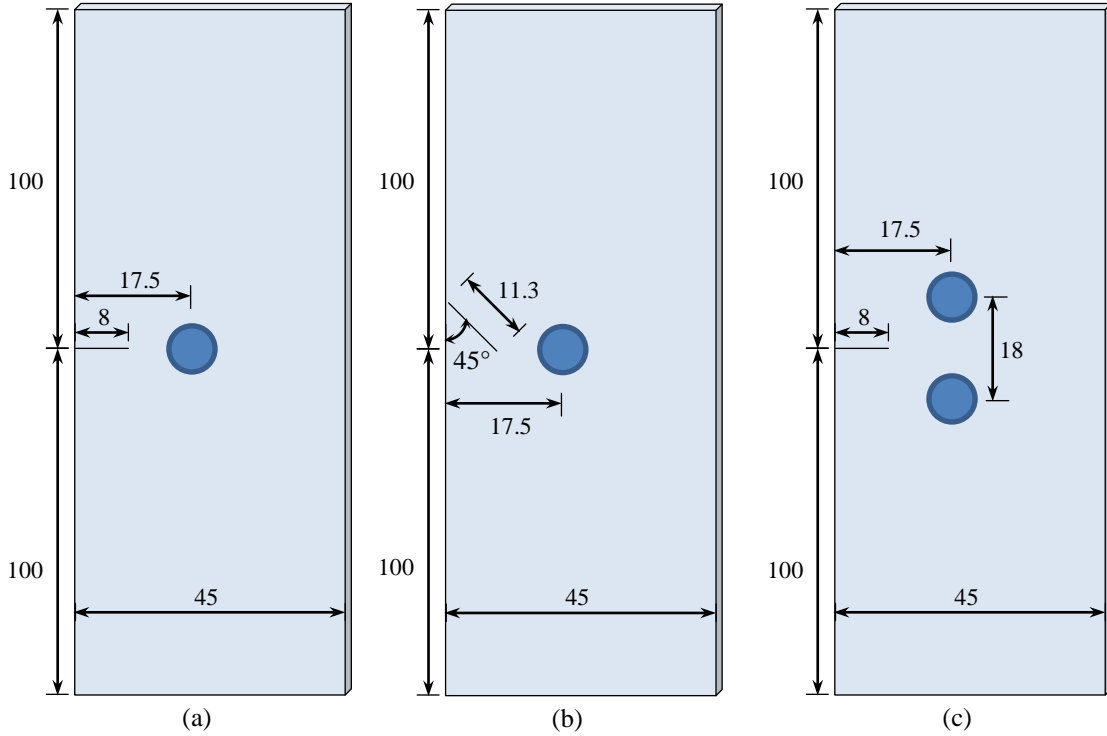


Fig. 3.2 Specimen geometries for various specimen configurations (all dimensions are in mm)

(a) SEN with single inclusion (b) ESC with single inclusion (c) SEN with two eccentric inclusions

### 3.3 Multi-Parameter Displacement Field Equations

Two dimensional stress field equations are used by O'Toole and Santare [43] to investigate the SIF of a straight crack near a rigid elliptical inclusion using photoelasticity Two-dimensional displacement field equations given by Atluri and Kobayashi [57, 58] for the general mixed mode case are given below and same equations have been used in the present work:

$$\begin{aligned} \begin{Bmatrix} u \\ v \end{Bmatrix} &= \sum_{n=1}^{\infty} \frac{A_n}{2G} r^{\frac{n}{2}} \begin{Bmatrix} k \cos \frac{n}{2} \theta - \frac{n}{2} \cos \left( \frac{n}{2} - 2 \right) \theta + \left\{ (-1)^n + \frac{n}{2} \right\} \cos \frac{n}{2} \theta \\ k \sin \frac{n}{2} \theta + \frac{n}{2} \sin \left( \frac{n}{2} - 2 \right) \theta - \left\{ (-1)^n + \frac{n}{2} \right\} \sin \frac{n}{2} \theta \end{Bmatrix} \\ &- \sum_{n=1}^{\infty} \frac{A_n}{2G} r^{\frac{n}{2}} \begin{Bmatrix} k \sin \frac{n}{2} \theta + \frac{n}{2} \sin \left( \frac{n}{2} - 2 \right) \theta + \left\{ -(-1)^n + \frac{n}{2} \right\} \sin \frac{n}{2} \theta \\ -k \cos \frac{n}{2} \theta - \frac{n}{2} \cos \left( \frac{n}{2} - 2 \right) \theta + \left\{ -(-1)^n + \frac{n}{2} \right\} \cos \frac{n}{2} \theta \end{Bmatrix} \end{aligned} \quad (3.1)$$



where,  $G$  is shear modulus,  $k = (3 - \nu)/(1 + \nu)$  for plane stress condition and  $k = (3 - 4\nu)$  for plane strain condition. Also,  $r$  and  $\theta$  are polar co-ordinates around the crack tip.  $A_I$  and  $A_{II}$  are the coefficients of displacement field representation. Initially data is collected from displacement pattern obtained from DIC that data contains  $x$ ,  $y$ ,  $u$  and  $v$  information. The cartesian co-ordinates  $x$  and  $y$  are converted to polar co-ordinates  $r$  and  $\theta$ . These  $r$  and  $\theta$ ,  $u$ , and  $v$  data are given as input to these equations which is obtained from DIC displacement fields.  $G$  and  $k$  are the material constants and  $n$  is a number of parameters which can be varied from 1 to  $\infty$ . These multi-parameter displacement field equations are solved to get vales of  $A_I$  and  $A_{II}$ . Once these values are known then using Equ. 3.2(a and b) it is possible to find out  $K_I$  and  $K_{II}$ .

$$K_I = A_{II}\sqrt{2\Pi} \quad (3.2a)$$

$$K_{II} = A_{III}\sqrt{2\Pi} \quad (3.2b)$$

where,  $K_I$  and  $K_{II}$  are stress intensity factors for modes I and II.

### 3.4 Over-deterministic Nonlinear Least Square Approach

Considering the rigid body motion (translation and rotation) the multi-parameter displacement field equations becomes:

$$u_x = \sum_{n=1}^{\infty} A_{In} f_I(r, \theta) - \sum_{n=1}^{\infty} A_{II n} f_{II}(r, \theta) + T_x - Ry \quad (3.3a)$$

$$u_y = \sum_{n=1}^{\infty} A_{In} g_I(r, \theta) - \sum_{n=1}^{\infty} A_{II n} g_{II}(r, \theta) + T_y + Rx \quad (3.3b)$$

Where,  $T_x$  is rigid body translation in  $x$ -direction,  $T_y$  is rigid body translation in  $y$ -direction and  $R$  is the rigid body rotation.

Error between theoretical and experimental values of  $u_x$  and  $u_y$  is calculated using Eq. (3.4).

$$h_{xk} = \sum_{n=1}^N A_{In} f_{In}(r_k, \theta_k) - \sum_{n=1}^N A_{II n} f_{II n}(r_k, \theta_k) + T_x - Ry_k - u_{xk} \quad (3.4a)$$

$$h_{yk} = \sum_{n=1}^N A_{In} f_{In}(r_k, \theta_k) - \sum_{n=1}^N A_{II n} f_{II n}(r_k, \theta_k) + T_y + Rx_k - u_{yk} \quad (3.4b)$$

Expanding Eq. 3.4 by Taylor's series method and neglecting higher order terms, it can be written in matrix form as;

$$h = b\Delta \quad (3.5)$$

Where,  $h$  = error between theoretical and experimental values of  $u_x$  and  $u_y$ ,  $b$  is the jacobian

of error function and  $\Delta$  is the difference between previous and current iteration. First initial guess is needed for  $A_{In}$ ,  $A_{IIIn}$ ,  $T_x$ ,  $T_y$ ,  $R$ ,  $x_c$  and  $y_c$ . To calculate  $h$  value, the values obtained from experiment and theoretical are subtracted for each and every iteration for values of  $u_x$  and  $u_y$ . Jacobian ( $b$ ) is calculated by taking differentiation of error function as shown in Eq.3.6.

$$h = \begin{bmatrix} -h_{x1} \\ \cdot \\ \cdot \\ -h_{xM} \\ -h_{y1} \\ \cdot \\ \cdot \\ -h_{yM} \end{bmatrix} \quad b = \begin{bmatrix} \frac{\partial h_{x1}}{\partial A_{I1}} & \cdot & \cdot & \frac{\partial h_{x1}}{\partial A_{II1}} & \cdot & \cdot & \frac{\partial h_{x1}}{\partial T_x} & 0 & \frac{\partial h_{x1}}{\partial R} & \frac{\partial h_{x1}}{\partial x_0} & \frac{\partial h_{x1}}{\partial y_0} \\ \cdot & \cdot & \cdot & \cdot & \cdot & \cdot & \cdot & \cdot & \cdot & \cdot & \cdot \\ \cdot & \cdot & \cdot & \cdot & \cdot & \cdot & \cdot & \cdot & \cdot & \cdot & \cdot \\ \frac{\partial h_{xM}}{\partial A_{I1}} & \cdot & \cdot & \frac{\partial h_{xM}}{\partial A_{II1}} & \cdot & \cdot & \frac{\partial h_{xM}}{\partial T_x} & 0 & \frac{\partial h_{xM}}{\partial R} & \frac{\partial h_{xM}}{\partial x_0} & \frac{\partial h_{xM}}{\partial y_0} \\ \frac{\partial h_{y1}}{\partial A_{I1}} & \cdot & \cdot & \frac{\partial h_{y1}}{\partial A_{II1}} & \cdot & \cdot & 0 & \frac{\partial h_{y1}}{\partial T_y} & \frac{\partial h_{y1}}{\partial R} & \frac{\partial h_{y1}}{\partial x_0} & \frac{\partial h_{y1}}{\partial y_0} \\ \cdot & \cdot & \cdot & \cdot & \cdot & \cdot & \cdot & \cdot & \cdot & \cdot & \cdot \\ \cdot & \cdot & \cdot & \cdot & \cdot & \cdot & \cdot & \cdot & \cdot & \cdot & \cdot \\ \frac{\partial h_{yM}}{\partial A_{I1}} & \cdot & \cdot & \frac{\partial h_{yM}}{\partial A_{II1}} & \cdot & \cdot & 0 & \frac{\partial h_{yM}}{\partial T_y} & \frac{\partial h_{yM}}{\partial R} & \frac{\partial h_{yM}}{\partial x_0} & \frac{\partial h_{yM}}{\partial y_0} \end{bmatrix} \quad \Delta = \begin{bmatrix} \Delta A_{I1} \\ \cdot \\ \cdot \\ \Delta A_{II1} \\ \cdot \\ \cdot \\ \Delta T_x \\ \Delta T_y \\ \Delta R \\ \Delta x_0 \\ \Delta y_0 \end{bmatrix} \quad (3.6)$$

In this methodology, the non-linear least square technique is used to reduce the error among theoretical and experimental value to obtain optimal parameters like  $A_{In}$ ,  $A_{IIIn}$ ,  $T_x$ ,  $T_y$ ,  $R$ ,  $x_c$  and  $y_c$ .

$$\Delta = (b^T b)^{-1} b^T h \quad (3.7)$$

Solving Eq. 3.7 it is possible to get the  $\Delta$  value. These values are updated to the respective variable for next iteration as shown below in Eq. 3.8.

$$(A_{I1})_{i+1} = (A_{I1})_i + \Delta A_{I1} \quad (3.8a)$$

$$(A_{II1})_{i+1} = (A_{II1})_i + \Delta A_{II1} \quad (3.8b)$$

$$(T_x)_{i+1} = (T_x)_i + \Delta T_x \quad (3.8c)$$

$$(T_y)_{i+1} = (T_y)_i + \Delta T_y \quad (3.8d)$$

$$(R)_{i+1} = (R)_i + \Delta R \quad (3.8e)$$

$$(x_0)_{i+1} = (x_0)_i + \Delta x_0 \quad (3.8f)$$

$$(y_0)_{i+1} = (y_0)_i + \Delta y_0 \quad (3.8g)$$

These new obtained values of  $A_{In}$ ,  $A_{IIIn}$ ,  $T_x$ ,  $T_y$ ,  $R$ ,  $x_c$  and  $y_c$  are replaced to earlier values in Eq. 3.4 for next iteration. The above procedure is continued till corrections become nearer to actual solution.

### **3.5 Specimen Preparation and Experimental Procedure**

#### **3.5.1 Crack Inclusion Specimen Preparation**

A rectangular epoxy sheets (300 mm x 120 mm) are fabricated in house using closed casting technique. Flat Perspex sheets of 6 mm thicknesses are used as a mold as shown in Fig.3.3. Pyrex glass rods of 6 mm diameter are cut to the exact length of 6 mm which is same as that of mold thickness. The surface of the mold and inclusion is cleaned thoroughly with isopropyl alcohol. The glass rods are then fixed in to the mold with care is taken that axis of glass rods should perpendicular to the flat Perspex sheets. The epoxy resin system is of CY230 and hardener is HY951 (supplied by Huntsman). The resin and hardener is taken in the proportion of 10:1 by weight. The resin and hardener is mixed at room temperature for about 30 minutes with precaution taken to avoid formation of any air bubbles. The resin-hardener mixture is then poured into the mold and left to cure for 24 hours at room temperature. The casted epoxy sheet is then checked in polariscope for the presence of any residual stresses. Finally, all the specimens are machined to the exact dimensions using milling machine.

During the machining, precaution is taken to avoid high cutting forces and excessive amount of heat generation. Figure 3.2 shows the specimen geometry and dimensions of the specimens used in the present study. It is not possible to pre-crack the epoxy specimens using fatigue loading due to very high brittle nature of epoxy, thin slits of thickness 0.3 mm are cut with the help of grinded hacksaw blades to simulate the real cracks. In order to reduce the effect of finite width and tip radius of the slit, the ends of the slits are extended with the help of toothed razor blade (thickness  $\approx 0.1$  mm) by an amount of 0.1 to 0.5 mm [47]. Then, the cracked test specimens are cleaned thoroughly with isopropyl alcohol. The surface of the specimens are coated with thin layer of white acrylic paint and over-sprayed with carbon black paint using an airbrush to obtain a random black-and-white speckle pattern (see Fig. 3.4 and Fig. 3.5).



Fig. 3.3 Mould used for preparing crack inclusion specimens

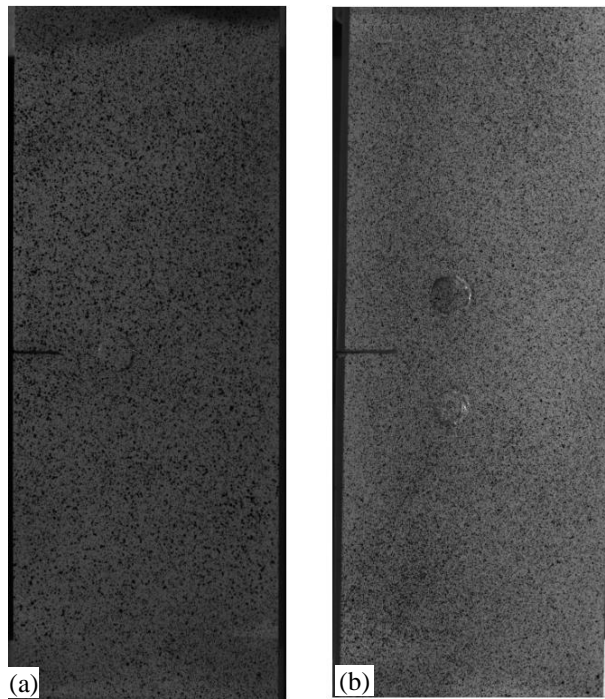


Fig. 3.4 Crack inclusion interaction Specimens with speckle (a) SEN with single inclusion (b) SEN with double inclusion

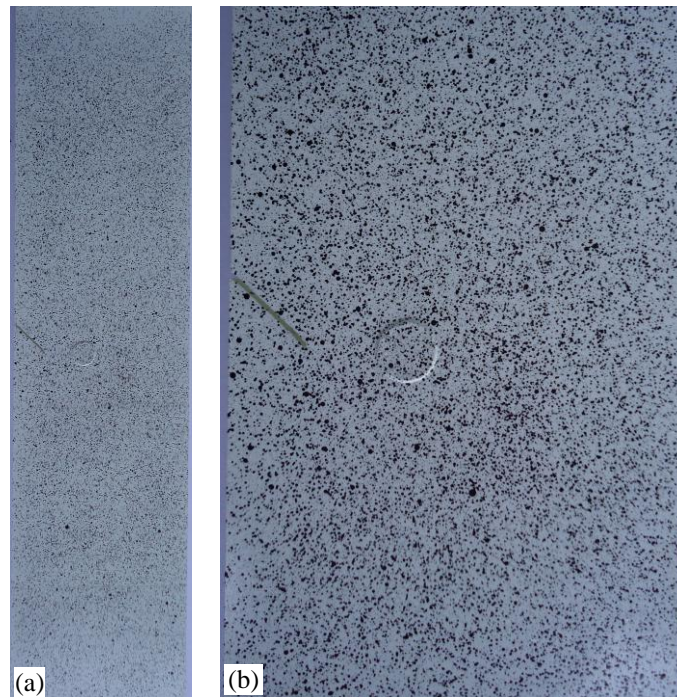


Fig. 3.5 (a) ESC with single inclusion full specimen (b) Zoomed speckle near crack inclusion

### 3.5.2 Material Characterization of Epoxy

Epoxy used in this work as the matrix material is initially characterized by performing uniaxial tension tests according to the ASTM D-638 [59]. The geometry of the dog-bone shaped specimens made up of epoxy resin system CY230 and HY951 hardener is shown in Fig.3.6.

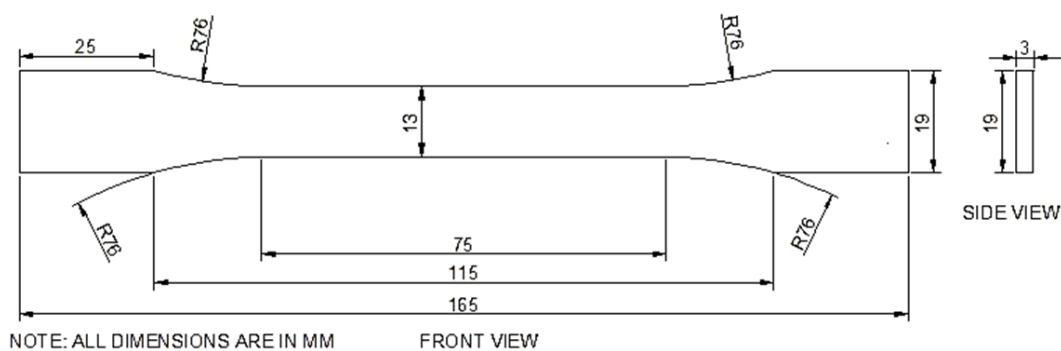


Fig. 3.6 Specimen geometry for tensile test according to ASTM D-638

The resin and hardener is taken in the proportion of 10:1 by weight. The resin and hardener is mixed at room temperature for about 25 minutes with precaution taken to avoid formation of any air bubbles. Material properties and strength parameters are determined using non-contact, full-field optical based technique namely digital image correlation (DIC). Minimum

five replicate specimens are tested and all tests are performed at a displacement control rate of 3.75 mm/min. The speckle pattern on specimen contains 110-130 black dots in the area of 100 mm<sup>2</sup> which is called as a speckle density of speckle pattern.

### **3.5.3 Experimental Procedure**

The experimental setup used for present study is shown in Fig. 3.7. It consists of a computer-controlled MTS Landmark® servo-hydraulic cyclic testing machine of 100 kN capacity and a 3D DIC setup (supplied from Correlation Solutions, Inc.). The 3D DIC system comprises of a pair of CCD cameras having a spatial resolution of 2448 x 2048 pixels coupled with Schneider Xenoplan lenses of 17 mm focal length. Light emitting diode of 20 watt is used as the light source and a portable laptop with image grabbing card is employed for image acquisition. The specimen is fixed into the self-adjusting hydraulic grips at a pressure of 4 MPa. The stereo vision system is then calibrated using planar dot grid pattern plate for its position and orientation. To carry out DIC experiments, specimen should contain speckle pattern. To do this speckle pattern, initially the surface of the specimens are coated with thin layer of white acrylic paint (manufactured from GOLDEN® (#8380-Series NA)) sprayed over the specimen. After drying this white paint, carbon black acrylic paint (manufactured from GOLDEN® (#8340-Series NA)) is over-sprayed over white paint using an airbrush of 0.5 mm nozzle diameter (iwata CM-B airbrush (manufactured by Iwata-Medea, Inc., Portland, Oregon, USA)) to obtain a random black-and-white speckle pattern. The air pressure is kept at 0.15 MPa to obtain satisfactory size of speckle and speckle density. Speckle density for different configurations of crack inclusion interaction specimens is shown in Table 3.1. Uniaxial tensile load is applied on these specimens in displacement control mode at a rate of 0.5 mm/min and images are continuously grabbed at a rate of 5 frames per second using the image acquisition system Vic-Snap got from Correlated Solutions. In order to ensure one-to-one correspondence between the grabbed image and applied load, an additional data acquisition card is employed providing an interface between MTS controller and image grabbing system. The images acquired by the stereo vision system are analyzed using the Vic-3D software to obtain whole field surface displacement and strain of the specimen. Figure 3.8 shows experimental setup for edge slant crack with inclusion specimen. In this case, cameras are tilted 45° with respect horizontal to coincide with the crack plane in the specimen.

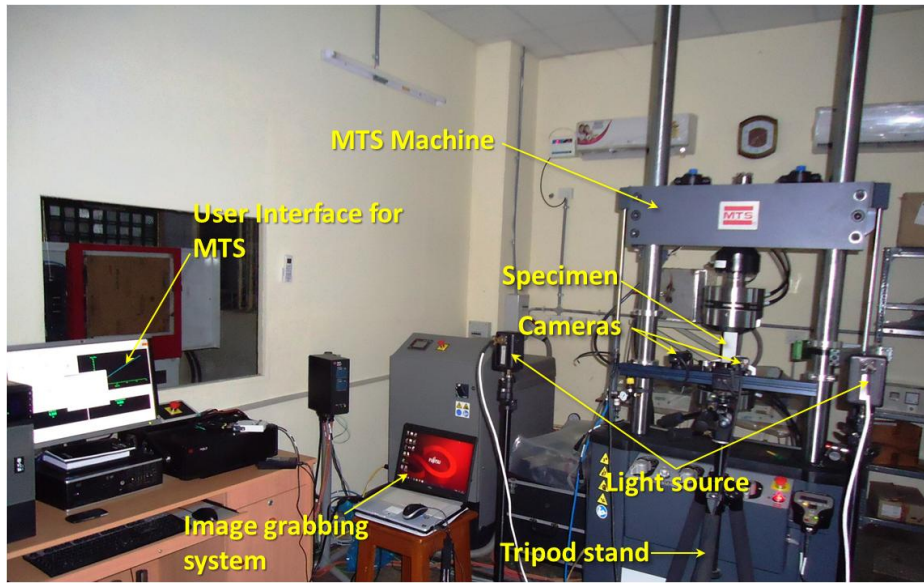


Fig. 3.7 Experimental setup comprising of MTS equipment along with 3D DIC system

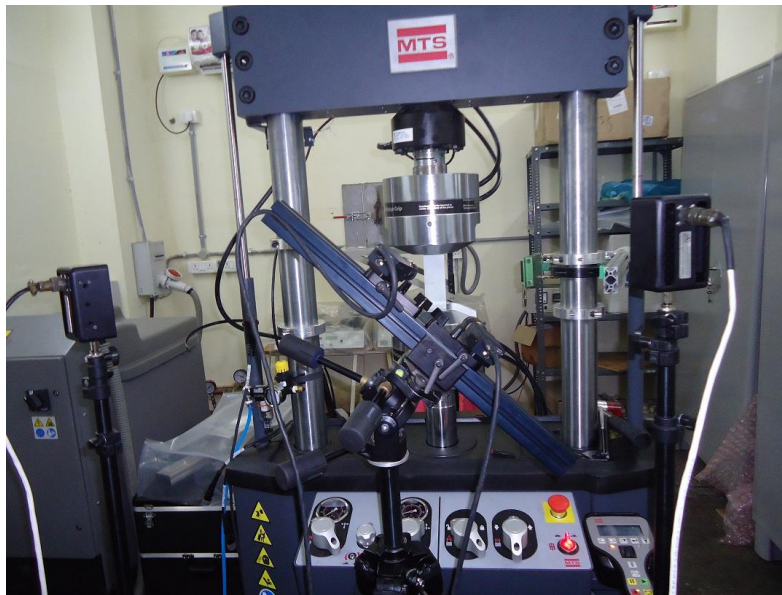


Fig. 3.8 Experimental setup for ESC with single inclusion specimen

Table 3.1 Speckle density for different configurations of crack inclusion interaction specimens

Specimen configuration	Speckle contains an area of 100 mm <sup>2</sup>
SEN with single inclusion	150-160
ESC with single inclusion	160-180
SEN with two eccentric inclusion	155-185

### 3.6 Numerical Computation of SIF's

#### 3.6.1 SIF Evaluation Methodology Using *J*-integral Approach

The finite element method is used for computing SIF in matrix crack inclusion interaction and to study the evolution of inclusion-matrix debonding in the presence of different orientations cracks. In this work 3D modeling and analysis of single edge notched (SEN) panel, edge slant cracked (ESC) panel having a circular inclusion ahead of the crack and single edge notched panel with two eccentrically placed inclusions is carried out using ANSYS 13 software. Computation of SIF's using FEA requires either a fine mesh around the crack tip or the use of 'special elements' with embedded stress singularity near the crack tip. In the present work, SIF's have been computed using *J*-integral approach [60]. During this estimation, linear elastic fracture mechanics (LEFM) behavior has been assumed for simplicity. The *J*-integral value evaluated using domain integral method as shown in Eq. 3.9 which path independent contour integral is defined as

$$J = \oint \left( W dx_2 - T_i \frac{\partial u_i}{\partial x_1} ds \right) \quad (3.9)$$

where,  $W$  is strain energy density;  $\sigma_{ij}$  are stress components;  $u_i$  are the displacements corresponding to local  $i$ -axis;  $s$  is the arc length of the contour;  $n_j$  is the  $j^{\text{th}}$  component of the unit vector outward normal to the contour  $C$ , which is any path of vanishing radius surrounding the crack tip.

The mixed-mode *J*-integral value is obtained from ANSYS directly by domain integral method. Using the assumption of linear elastic fracture mechanics,  $K_I$  and  $K_{II}$  are related to the *J*-integral as shown in Eq. 3.10 and taken from Ref. [13]:

$$J = K_I^2 / E' + K_{II}^2 / E' \quad (3.10)$$

Where,  $E'$  is modulus of elasticity,  $E' = E$  for plane stress conditions and  $E' = E / (1 - \nu^2)$  for plane strain conditions,  $\nu$  is Poisson's ratio. In case of three dimensional analyses, plain strain condition is considered for estimating SIF. In order to determine  $K_I$  and  $K_{II}$ , the ratio of  $K_I$  over  $K_{II}$  is obtained from the ratio of the normal distance to the horizontal distance of two closest nodes to the crack-tips which they have been coincided before loading as shown in Fig. 3.10.



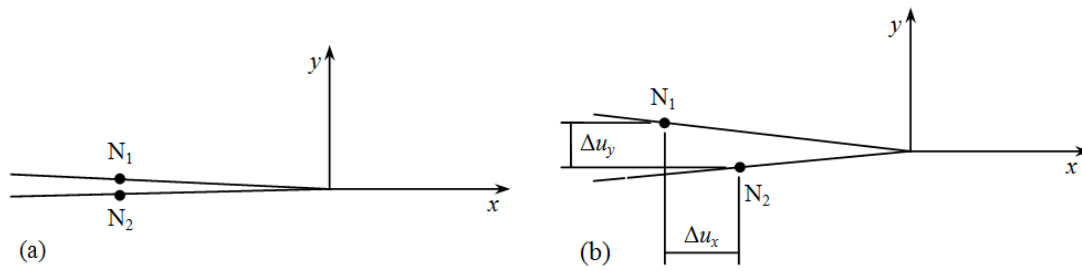


Fig. 3.9 Nodes nearer to crack tip (a) two coincident nodes near the crack tip before loading (b) two nearest nodes near the crack tip after loading

### 3.6.2 Finite Element Modeling

#### 3.6.2.1 Modeling of SEN with Single Inclusion Specimen

The commercially available finite element package ANSYS 13 is used in the current study. A general finite element code known as Ansys Parametric Design Language (APDL) is written specifically for this study. Initially two dimensional areas is created as per the model dimension and meshed with mesh 200 element having 8-nodes. Figure 3.10 shows the half symmetric finite element model of SEN with single inclusion. Very fine meshing is kept around the crack tip and inclusion pair for capturing very high stress gradient. Element size at the crack tip is kept as 0.001 mm. A different set of elements forming the interface between the inclusion and the matrix is generated as shown in Fig. 3.10 (b). This interfacial layer is modeled to have a thickness of 0.06 mm. Later, all the areas are extruded in thickness direction to generate volume. Finally, all the generated volumes are meshed with 20-noded solid 186 brick element. In the thickness direction, the panel is meshed with six elements. Isotropic epoxy material properties are assigned for the panel elements and glass material properties are assigned for the inclusion elements. The crack plane nodes are arrested in  $y$ -direction and crack tip nodes are arrested in  $x$  and  $z$ -directions and a tensile load are being applied on the bottom surface of the panel.

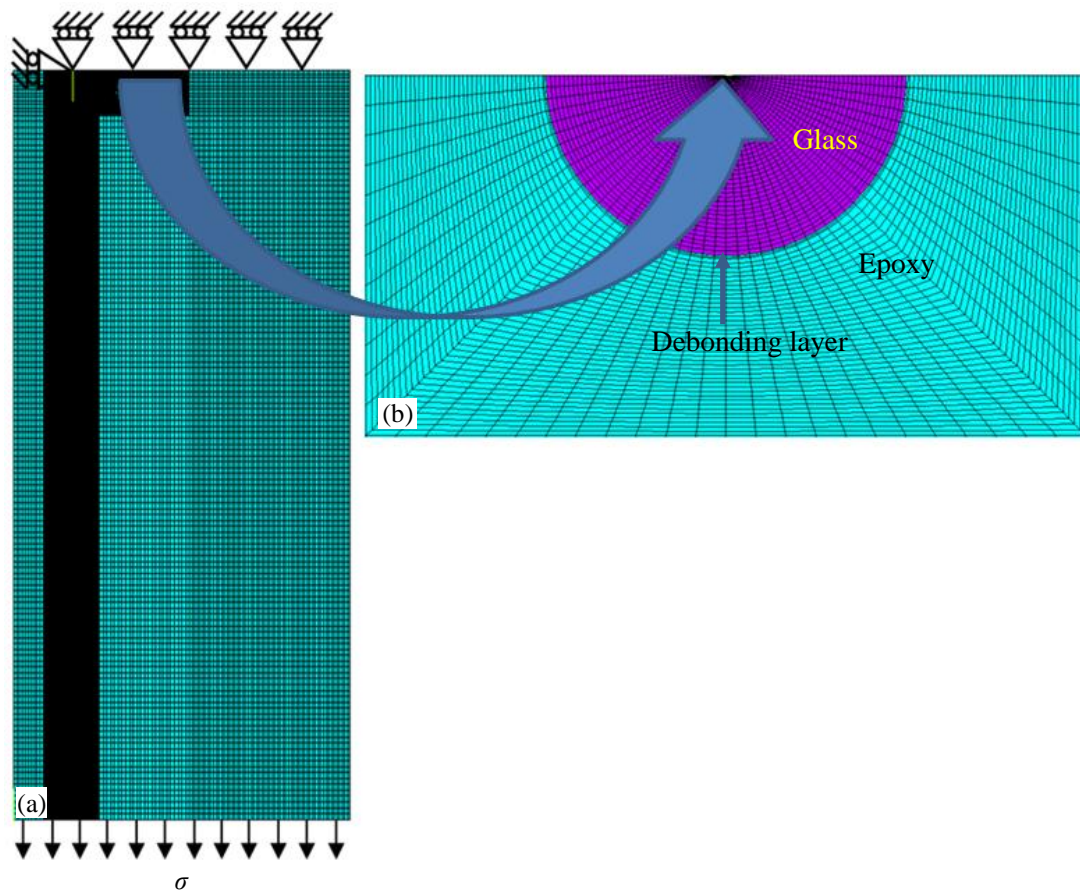


Fig. 3.10 Finite element model of SEN with single inclusion specimen (a) Front view of half symmetry model with boundary conditions (b) Zoomed view of interfacial debonding layer between glass and epoxy [47]

### 3.6.2.2 Modeling of Edge Slant Crack with Singular Inclusion

The geometry of edge slant crack (ESC) with singular inclusion is shown in the Fig. 3.11. Initially, two dimensional area is created as per required geometry. First crack tip is created and around it very fine meshed area is created. The meshing is done using 200 element having 8-nodes. Individual areas are created around the crack tip. In the present analysis, crack tip element size is 0.003 mm. The crack tip mesh has a total of 7128 elements (36 circumferential, 33 radial and 6 elements in thickness direction) around the crack tip region as shown in Fig. 3.11 (b). To create the 3D panel, the created areas are extruded along the thickness direction to create the panel volume. All lines along the thickness direction are divided into six segments. Then all the areas are meshed with 20-noded solid 186 brick element. On the bottom face of the panel tensile load is applied and on top face all degrees of freedom of all nodes are arrested.

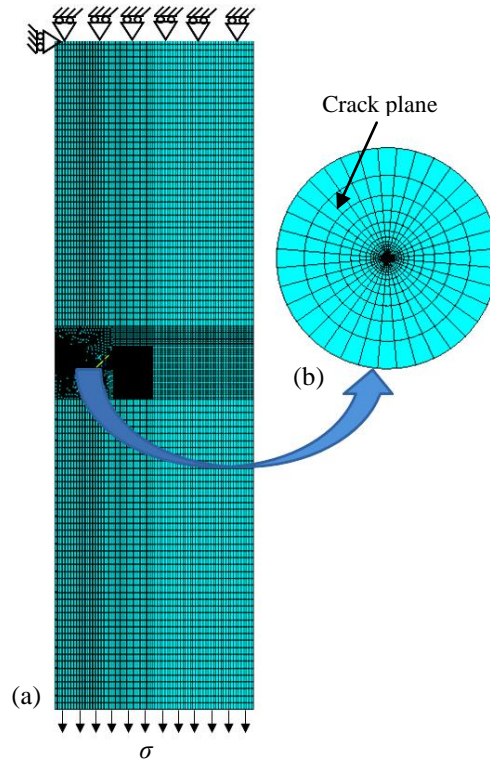


Fig. 3.11 Finite element model of ESC with single inclusion specimen (a) Front view of full model with boundary conditions (b) Meshing around crack tip

### 3.6.3 Interfacial Layer Debonding

A criteria based on the ultimate strength of epoxy is used to simulate debonding of the inclusion from matrix. A radial stress criterion is considered for debonding of inclusion from matrix interface. The implementation of macro-routine is as per the flow chart given in Fig. 3.12. A 3D finite element model is initially built by giving as input the initial material properties, dimension of the specimen, boundary conditions, initial load and the load increment value. Initially, a small initial load (200 N) is applied to the model and stresses in each element are estimated. The estimated stress values are checked for bond layer failure criterion to check for debonding initiation. The bond layer failure criteria occur when radial stress attains a fraction of the ultimate stress of the matrix material in these elements. The criteria proposed for deactivation of an element in bond layer is shown in Eq. (3.11) and taken from Ref. [45, 46]:

$$(\sigma_{rr}) = \beta \sigma_o \quad (3.11)$$

Where  $(\sigma_{rr})$  is the radial stress,  $(\sigma_o)$  is the ultimate strength of matrix material and  $\beta$  is the multiplication factor ranges from 0 to 1. The value of  $\sigma_o$  is 51 MPa for epoxy based material. If these criteria is not satisfied then none of the elements has failed in the bond

layer, then it will write  $J$  integral value and an incremental load is applied by a predefined value of 200 N. If any of the elements has failed, material properties of the failed element are degraded to a very small value. In this work a reduction factor of  $1 \times 10^{-8}$  is used. This deactivated element prevents from contributing to the overall stiffness of the structure. That is, the respective rows and columns of the stiffness matrix are made negligibly small without replacing them by zeros. When material properties are degraded in an element, the load redistributes to other elements, which could then fail at the same load. It is therefore necessary to iterate at the same load level when material properties are degraded to check if other elements undergo failure. As well as before incrementing the load, SIF value has to compare with critical stress intensity factor value ( $K_c$ ) which is a material property. If SIF value is more than fracture toughness value ( $K_c$ ) then crack has to be propagated by 0.5 mm along the crack plane and then it has to increment the load. If SIF value is less than fracture toughness ( $K_c$ ) value then directly it can increment the load. In this study, crack is assumed to be stationary.

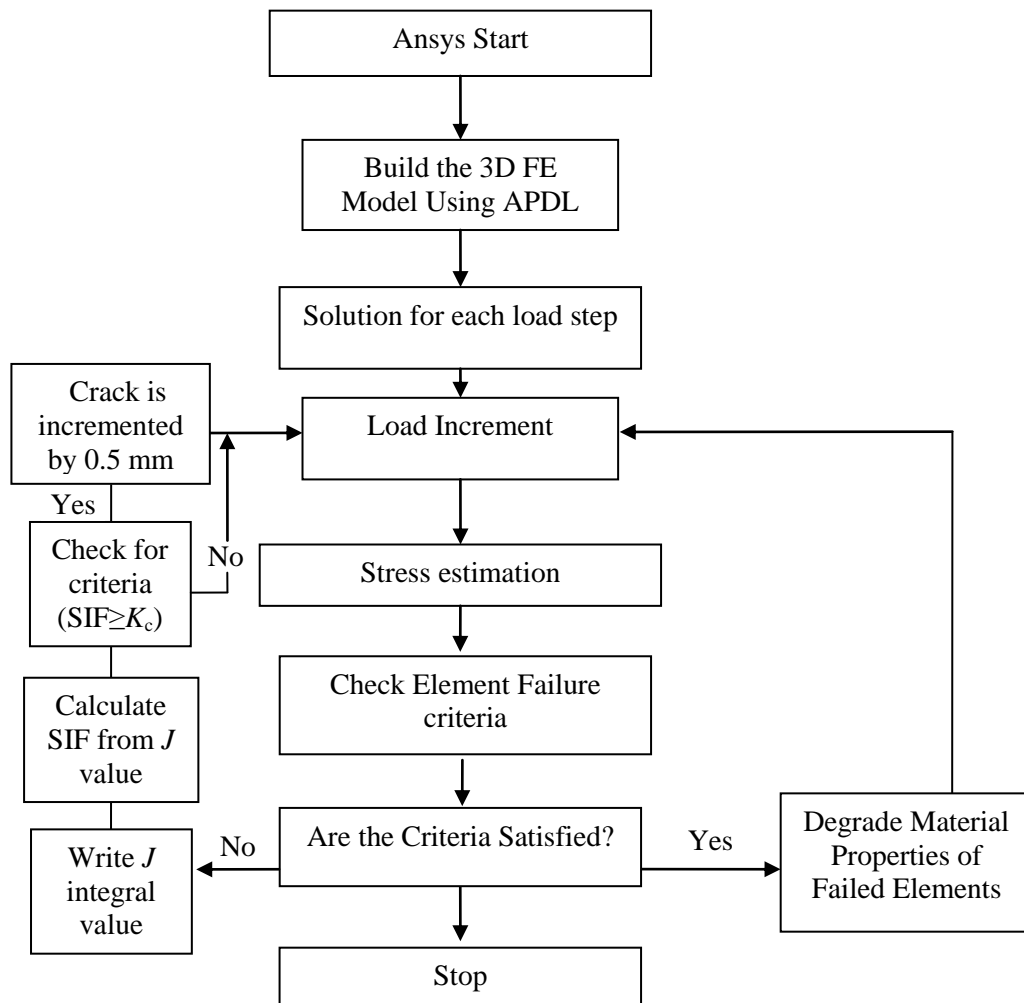


Fig. 3.12 Flow diagram for interfacial layer debonding using ANSYS APDL

### 3.7 SIF Estimation Using DIC

#### 3.7.1 Data Analysis Using DIC

The images acquired by the stereo vision system are analyzed using the commercially available Vic-3D software to obtain the whole field displacement distribution in the vicinity of crack inclusion. Along  $u$  displacement contour map and  $v$  displacement contour maps data  $x'$ ,  $y'$ ,  $u$  and  $v$  are collected. Data is collected from the annular region surrounding the crack-tip, the inner radius of which is chosen more than half of the specimen thickness to avoid the three-dimensional effects and non-linear process zone in the vicinity of the crack tip. The outer radius of the annular data collection region is limited such that  $r/a \leq 1$ . Then this collected data values of  $x'$ ,  $y'$ ,  $u$  and  $v$  are compiled into excel sheet and this file is given as an input for estimating SIF from DIC.

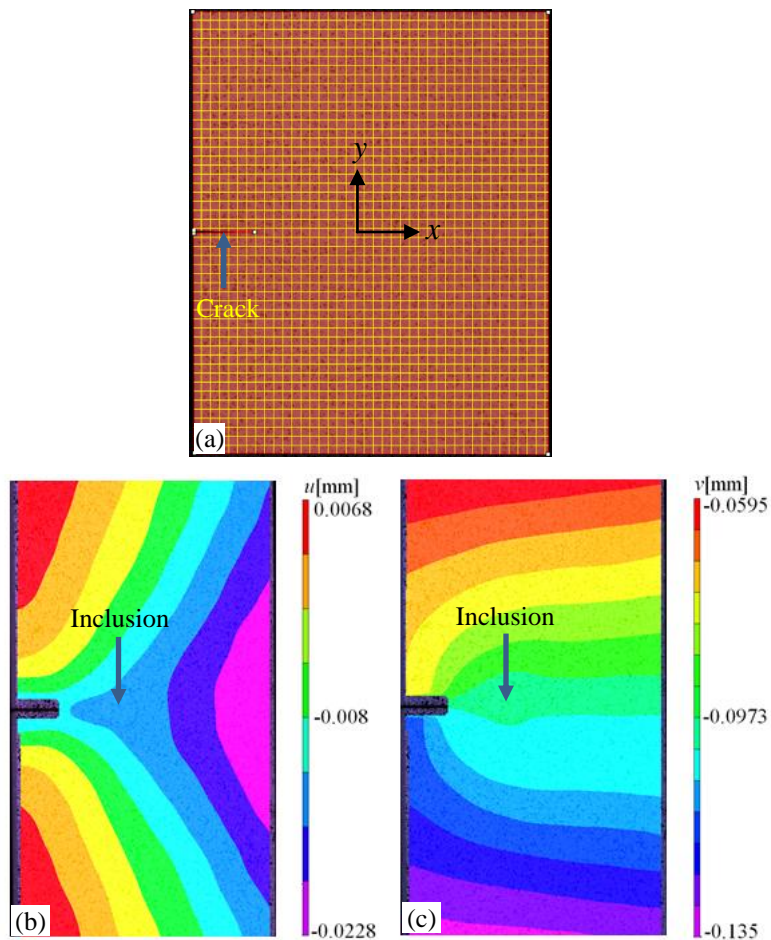


Fig. 3.13 showing the results of data analysis for SEN with single inclusion specimen  
(a) region of interest with subsets used for correlation (b)  $u$ -displacement contour map (c)  $v$ -  
displacement contour map (subset size:  $15 \times 15$ )

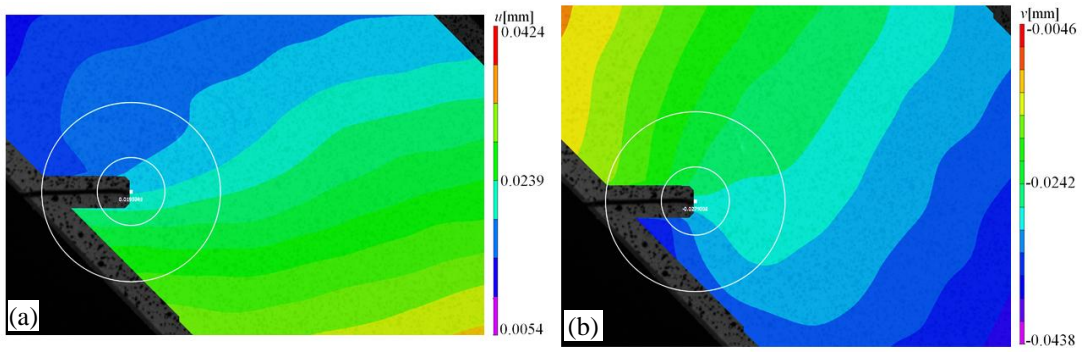


Fig. 3.14 showing the results of data analysis with subset size:  $15 \times 15$

(a)  $u$ -displacement contour map (b)  $v$ -displacement contour maps for ESC with single inclusion specimen

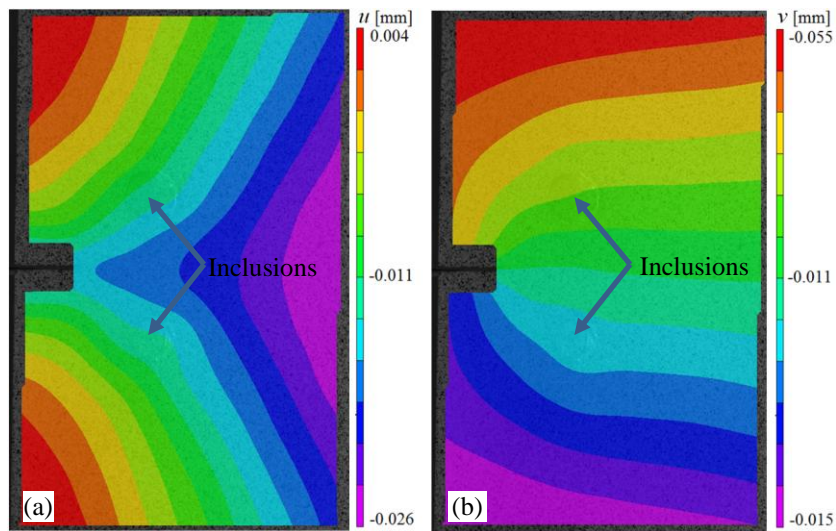
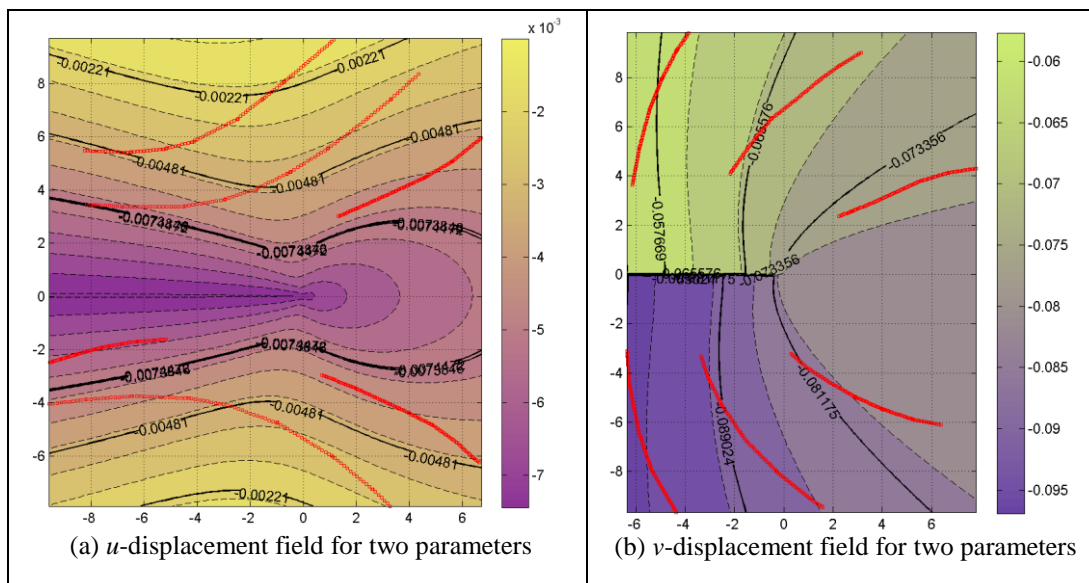
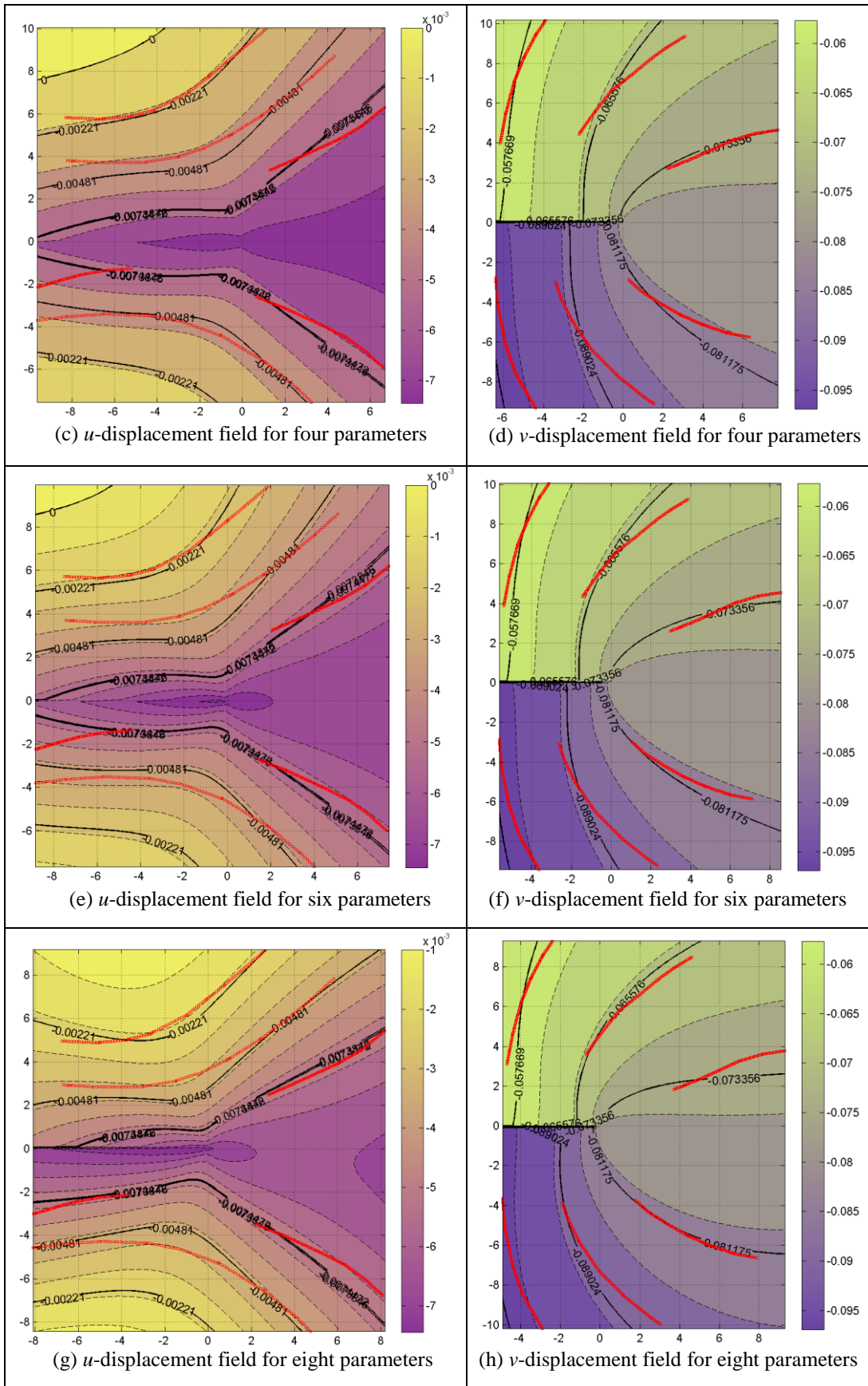


Fig. 3.15 showing the results of data analysis for SEN with double inclusion specimen (a)  $u$ -displacement contour map (b)  $v$ -displacement contour map (subset size:  $17 \times 17$ )





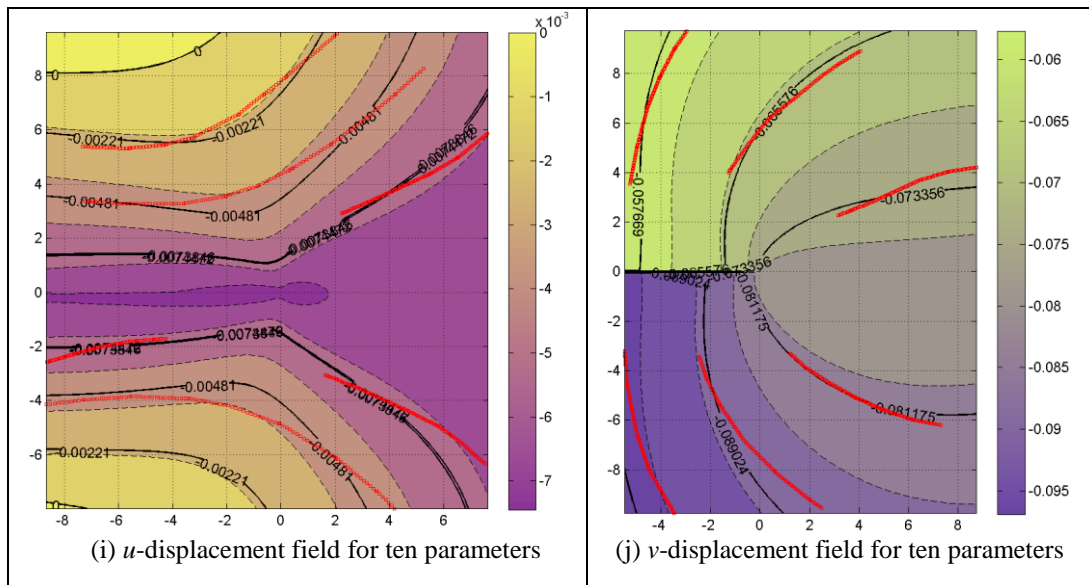


Fig. 3.16 Theoretically reconstructed displacement field for SEN with single inclusion specimen for various parameters with data points echoed back indicated by red marker points (all displacement values are in mm)

Figure 3.16 shows the theoretically reconstructed displacement field around the crack tip of SEN specimen with single inclusion in front of crack tip (subjected to a load of 399 N) obtained using various parameters with the data points echoed back (indicated by red colored marker dots). For 10 parameters, the data points coincide very well with reconstructed contours assuring the sufficiency of ten parameters. Comparison of  $K_I$  for the SEN with single inclusion specimen obtained from DIC and FEA as a function of number of parameters is shown in Fig. 3.17. From the graph, one can observe that DIC and FEA results are in good agreement besides small difference in  $K_I$  value (error is 2.4 %).



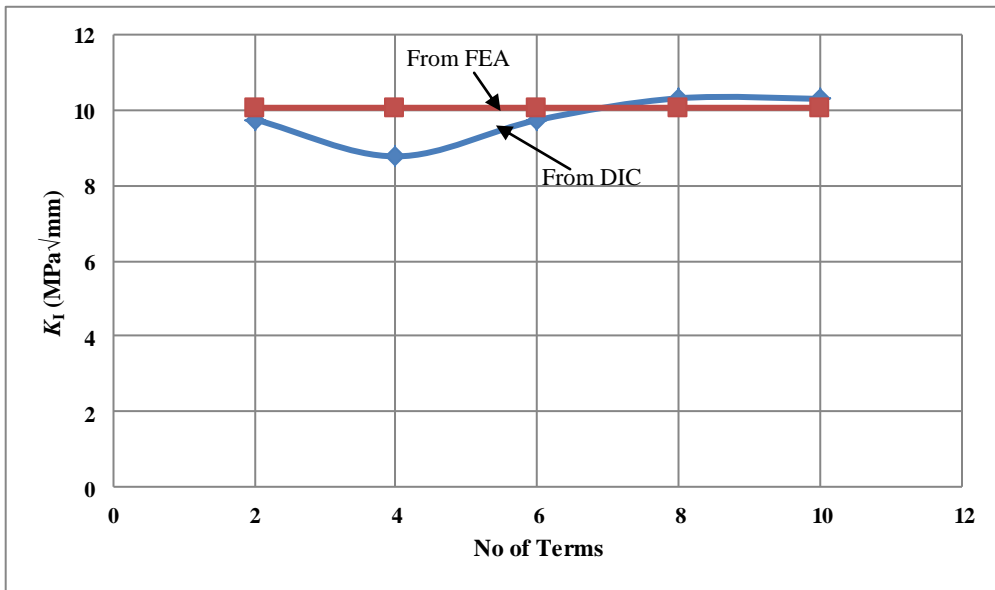
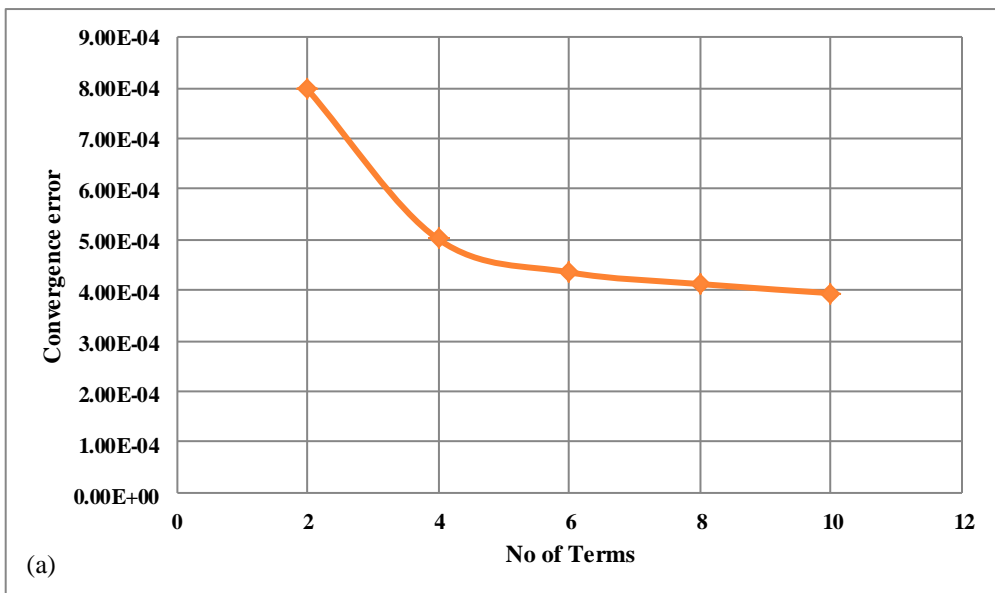


Fig. 3.17 Graph showing variation of  $K_I$  as a function of number of parameters

Figure 3.18 shows the graph of variation of convergence error achieved as well as calculated co-ordinates of the crack-tip location ( $x_c$  and  $y_c$ ) as a function of number of parameters for SEN with single inclusion specimen. The reference location for  $x_c$  and  $y_c$  is at the center of the post processed image of DIC. With the increase in number of parameters, the convergence error reduces and also, the co-ordinates of the crack-tip stabilize to constant value. It is to be noted that co-ordinates of the crack-tip are with respect to image co-ordinate system. The crack tip coordinates from DIC are  $x_c = -12.78$  mm and  $y_c = 1.41$  mm.



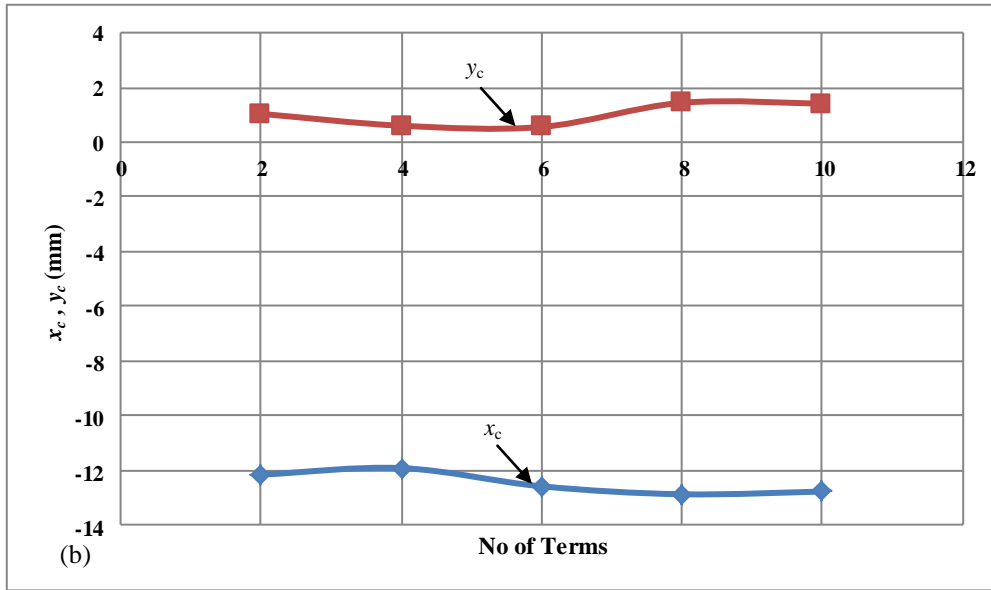


Fig. 3.18 Graph of (a) convergence error and (b) co-ordinates of the crack-tip location vs. number of parameters

Fig. 3.19 shows the  $v$  displacement field distribution obtained from FEA before debonding and after debonding of the inclusion in the crack inclusion region for half symmetry model of SEN with single inclusion. The displacement field before debonding is taken at a load of 399 N and after debonding it is at 1400 N. For this load of 1400 N inclusion is partially debonding from the matrix. From the plot, it can be observed that, before debonding contours of displacement are parallel to the inclusion and it is not interacting with inclusion shown in Fig. 3.19 (a). On careful observation, it is clear that after debonding of the inclusion displacement contours are interacting with inclusion as shown in Fig. 3.19 (b).

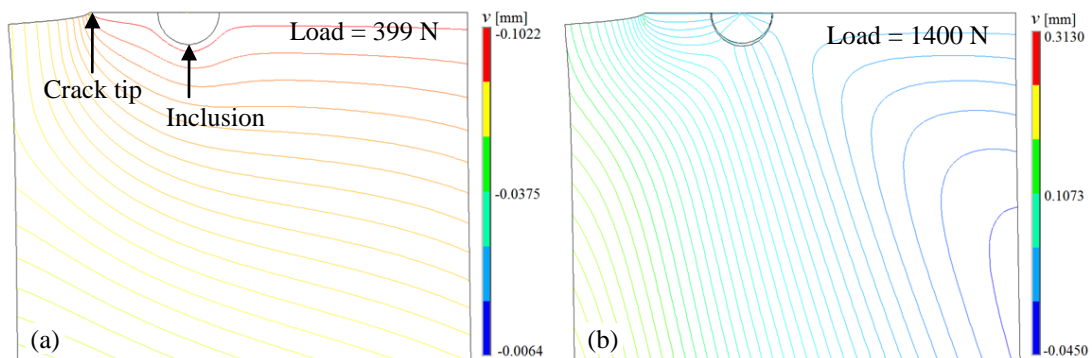


Fig. 3.19 Displacement field obtained from finite element analysis showing  $v$ -displacement in the crack inclusion region (a) before debonding of inclusion (b) after debonding of inclusion

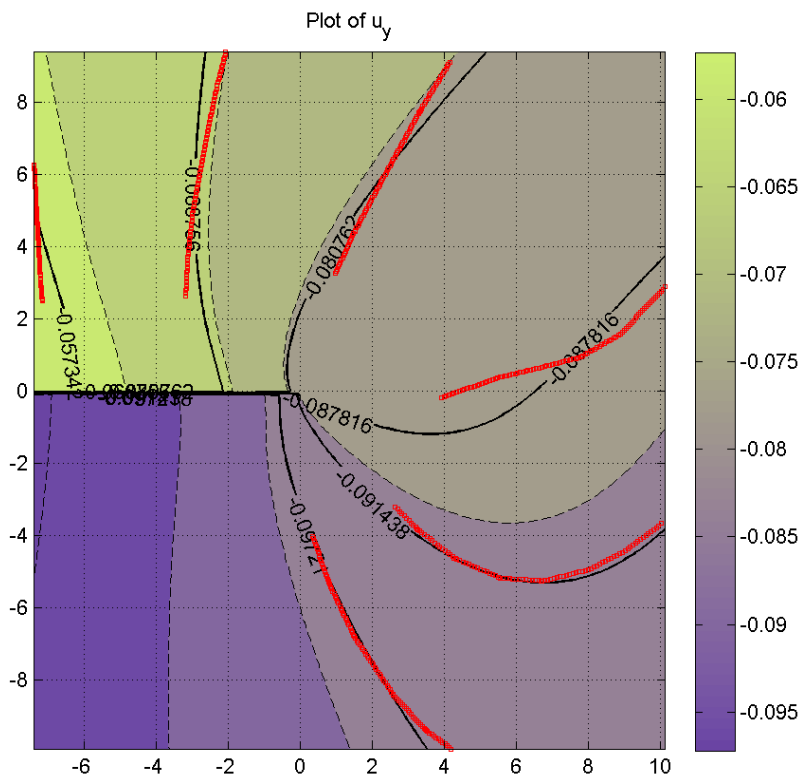
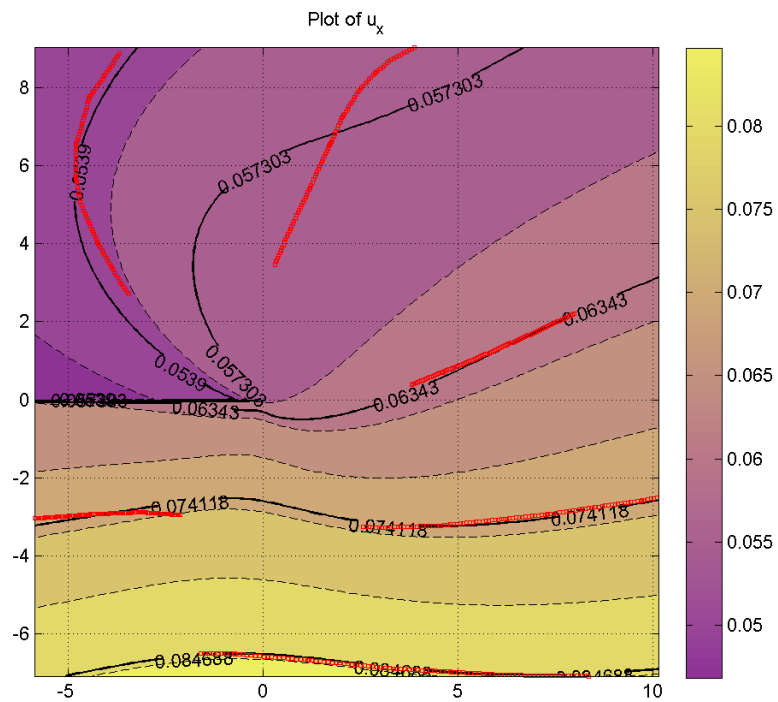


Fig. 3.20 Theoretically reconstructed displacement field for ESC with single inclusion specimen for 12-parameter solution (all displacement values are in mm)

Figure 3.20 shows the theoretically reconstructed displacement field around the crack tip of ESC specimen with single inclusion (subjected to a load of 417 N) obtained using various

parameters with the data points echoed back (indicated by red colored marker dots). For 12 parameters, the data points coincide very well with reconstructed contours assuring the sufficiency of ten parameters. Comparison of  $K_I$  and  $K_{II}$  for the ESC with single inclusion specimen obtained from DIC and FEA as a function of number of parameters is shown in Fig. 3.21. From the graph, one can observe that DIC and FEA results are in good agreement besides small difference in  $K_I$  value (error is 3.86 %) and  $K_{II}$  value (error is 6.05 %).

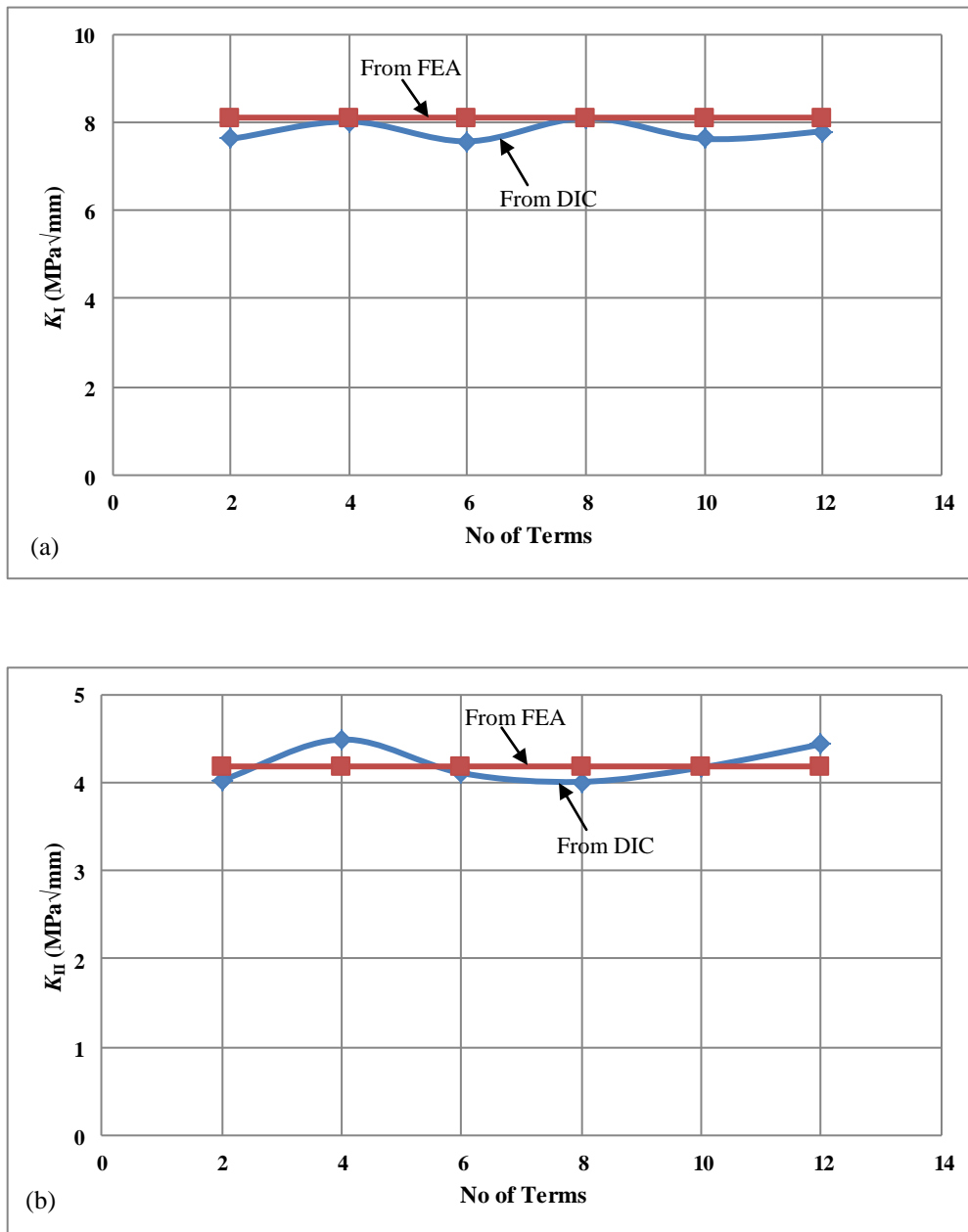


Fig. 3.21 Graph showing variation of mixed mode SIF's as a function of parameters (a)  $K_I$  (b)  $K_{II}$

Figure 3.22 shows the graph of variation of convergence error achieved as well as calculated co-ordinates of the crack-tip location ( $x_c$  and  $y_c$ ) as a function of number of parameters for ESC with single inclusion specimen. The reference location for  $x_c$  and  $y_c$  is at the center of the post processed image of DIC. With the increase in number of parameters, the convergence error reduces and also, the co-ordinates of the crack-tip stabilize to constant value. It is to be noted that co-ordinates of the crack-tip are with respect to image co-ordinate system. The crack tip coordinates from DIC are  $x_c = -9.53$  mm and  $y_c = -10.71$  mm.

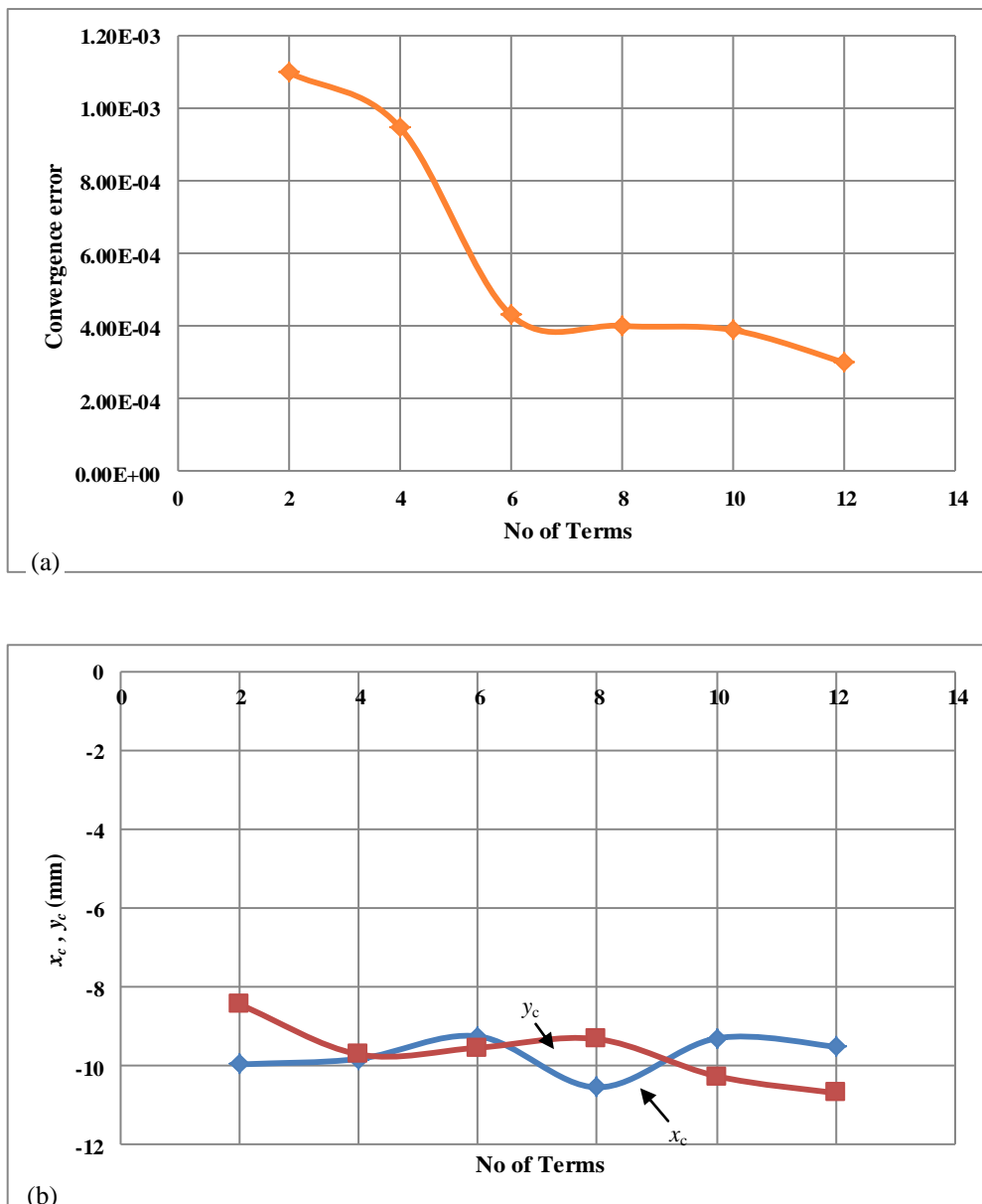


Fig. 3.22 Graph of (a) convergence error and (b) co-ordinates of the crack-tip location vs. number of parameters

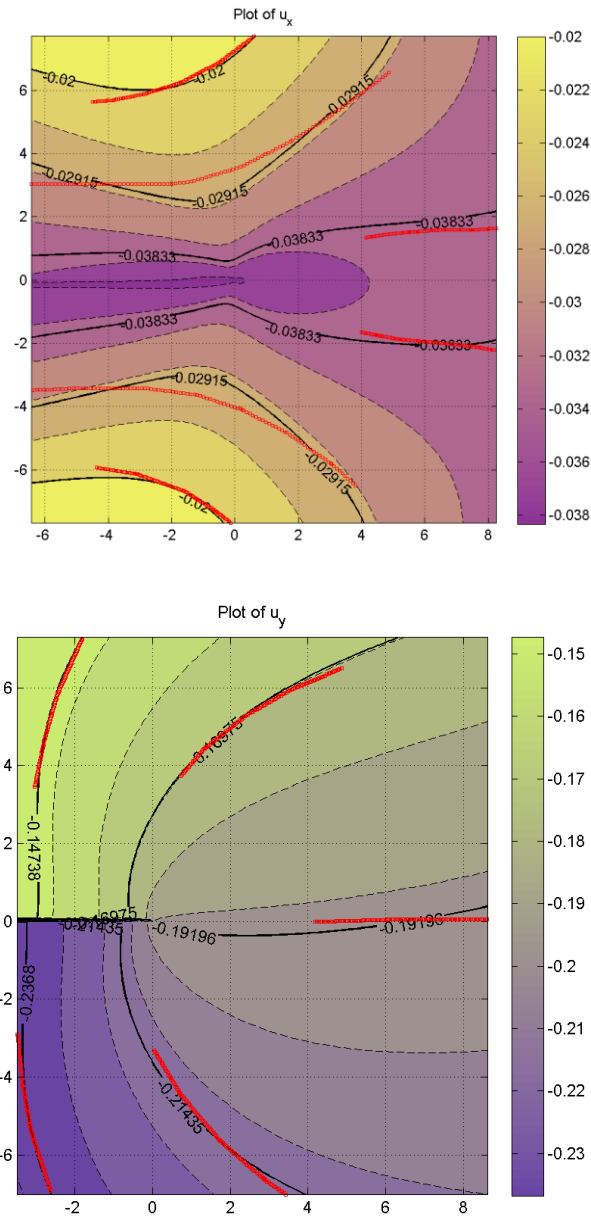


Fig. 3.23 Theoretically reconstructed displacement field for SEN with two eccentric inclusion specimen for various parameters (all displacement values are in mm)

Figure 3.23 shows the theoretically reconstructed displacement field around the crack tip of SEN specimen with two eccentric inclusion (subjected to a load of 804 N) obtained using various parameters with the data points echoed back (indicated by red colored marker dots). For 12 parameters, the data points coincide very well with reconstructed contours assuring the sufficiency of ten parameters. Comparison of  $K_I$  for the SEN with two eccentric inclusion specimen obtained from DIC and FEA as a function of number of parameters is

shown in Fig. 3.24. From the graph, one can observe that DIC and FEA results are in good agreement besides small difference in  $K_I$  value (error is 1.5 %).

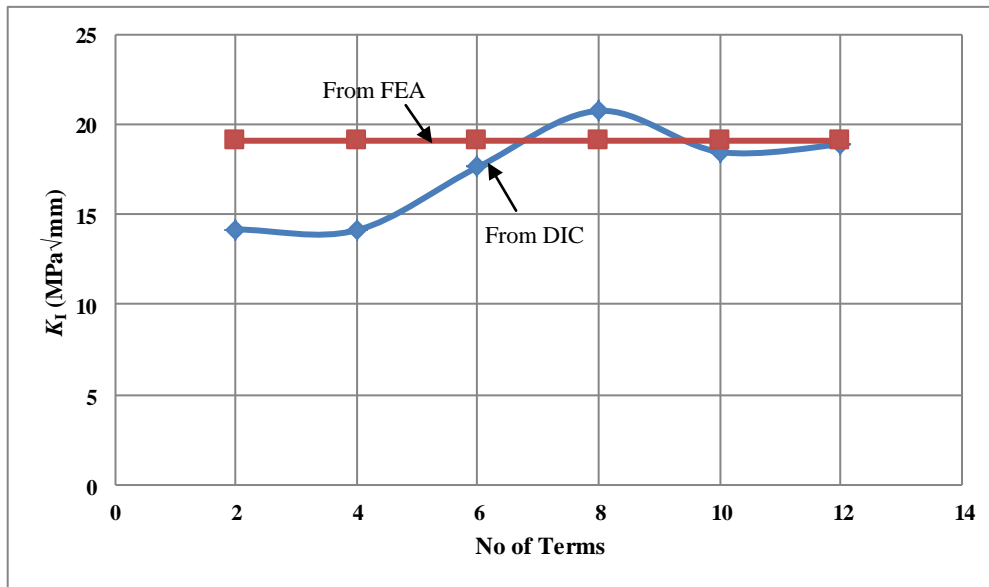


Fig. 3.24 Graph showing variation of  $K_I$  as a function of number of parameters

Figure 3.25 shows the graph of variation of convergence error achieved as well as calculated co-ordinates of the crack-tip location ( $x_c$  and  $y_c$ ) as a function of number of parameters for SEN with two eccentric inclusion specimen. With the increase in number of parameters, the convergence error reduces and also, the co-ordinates of the crack-tip stabilize to constant value. It is to be noted that co-ordinates of the crack-tip are with respect to image co-ordinate system it is at center of the post processed image. The crack tip coordinates from DIC are  $x_c = -13.87$  mm and  $y_c = 0.27$  mm.

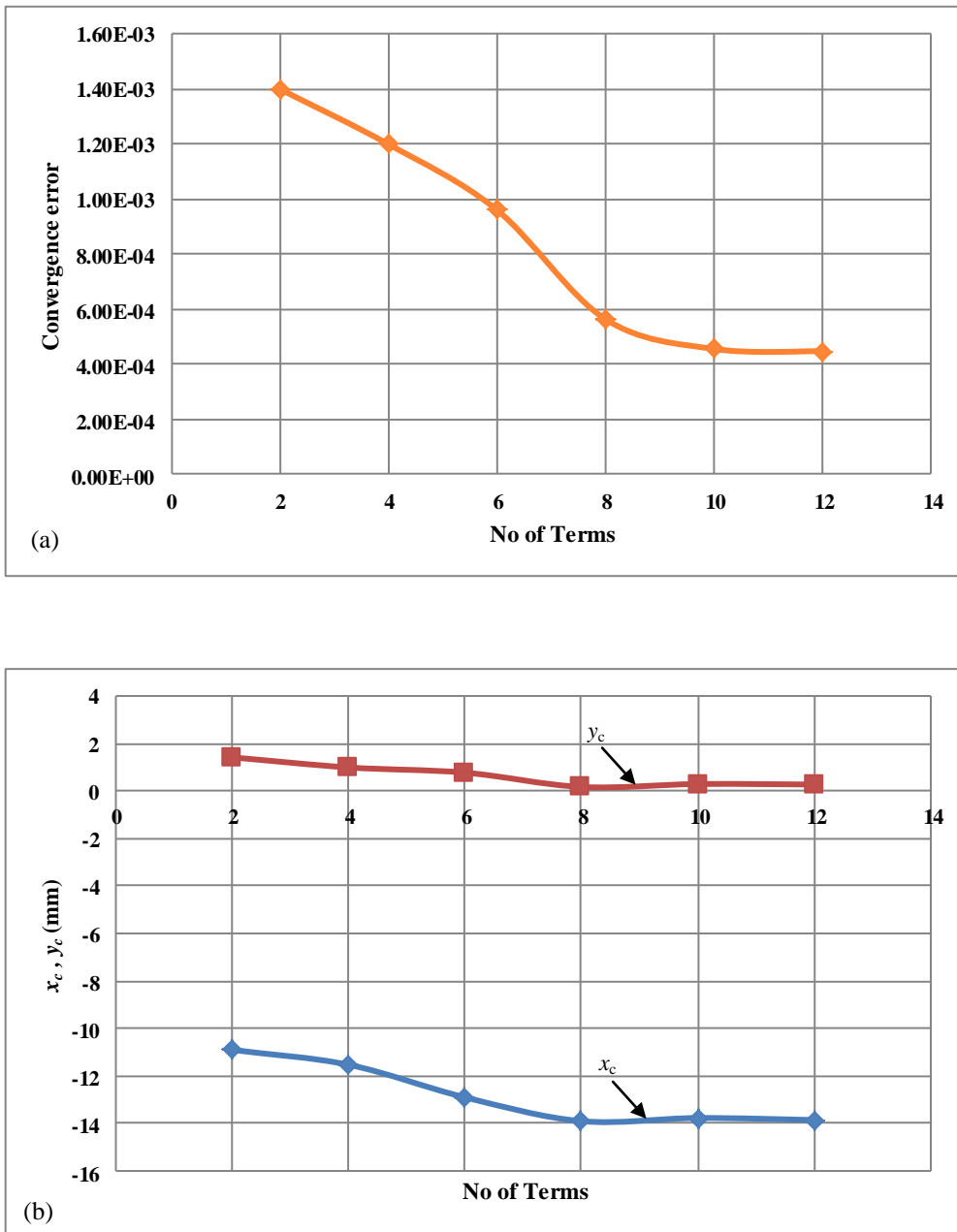


Fig. 3.25 Graph of (a) convergence error and (b) co-ordinates of the crack-tip location vs. number of parameters

### 3.8 Results and Discussion

#### 3.8.1 Material Characterization

The epoxy specimens as per ASTM D638 are characterized using whole-field experimental technique namely digital image correlation as shown in Fig. 3.26. To analyze images using DIC method, a region of interest (ROI) 13 mm x 20 mm is defined on the specimen surface



within the gauge length of extensometer. A subset size  $27 \times 27$  pixels ( $13 \times 20 \text{ mm}^2$ ) is chosen along with a grid step size of 7 pixels for discretization of region of interest. This small zone is named as zone of interest (ZOI). The stress-strain plot for tensile test obtained from DIC is shown in Fig. 3.27. The modulus of elasticity is calculated from initial slope of the stress-strain curve. The young's modulus, Poisson's ratio, yield stress and ultimate strength values obtained from the tests are given in Table 3.2. The maximum, minimum and average value of each property obtained from three independent measurements is reported in table and they are at room temperature.

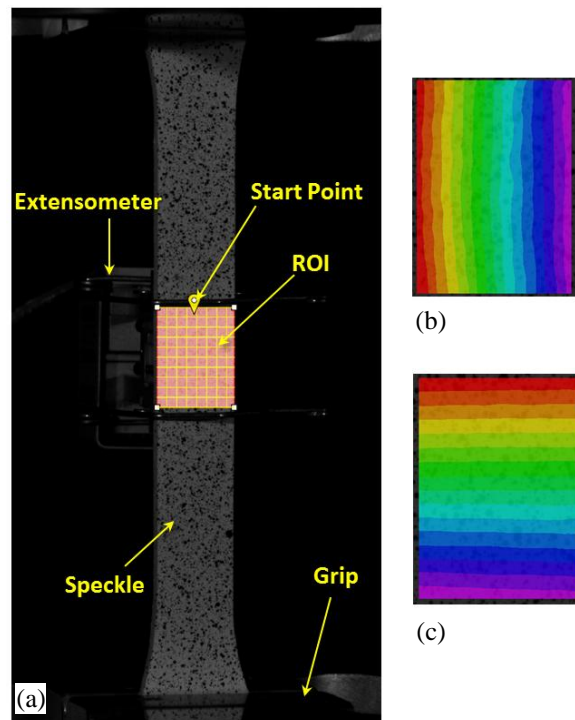


Fig.3.26 Material characterization using DIC (a) Specimen with extensometer and ROI (b)  $u$ -displacement contour map (c)  $v$ -displacement contour map

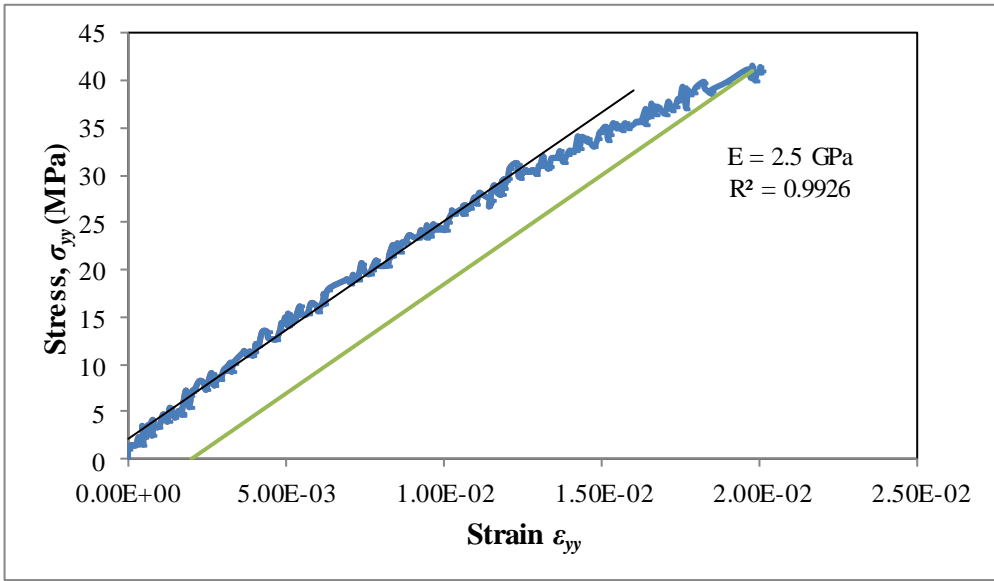


Fig. 3.27 Stress strain curve obtained from DIC

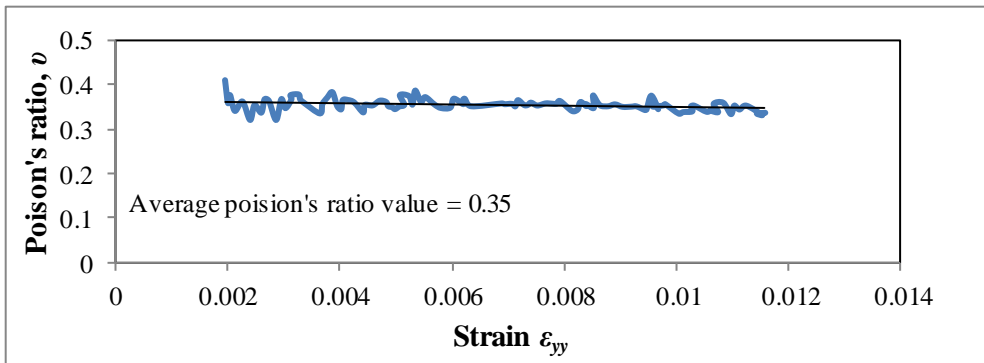


Fig. 3.28 Poisson's ratio obtained from DIC

Table 3.2 Material properties of epoxy (resin CY230 and hardener HY951)

Material type	Young's modulus $E$ (GPa)	Poisson's ratio $\nu$	Yield stress (MPa)	Ultimate Stress (MPa)
Epoxy	2.5	0.35	42	51
Glass	68	0.19	-	-

### 3.8.2 Crack Inclusion Interaction Study

Figure 3.29 shows the variation of SIF of edge slant crack specimen with single inclusion with load. From the plot one can observe that for initial load steps SIF variation is linear and there is sharp rise in the SIF value once the debonding is happened. After debonding, the variation of SIF is also linear. The inclusion debonding from matrix is captured from experimental study based on jump in the SIF values.

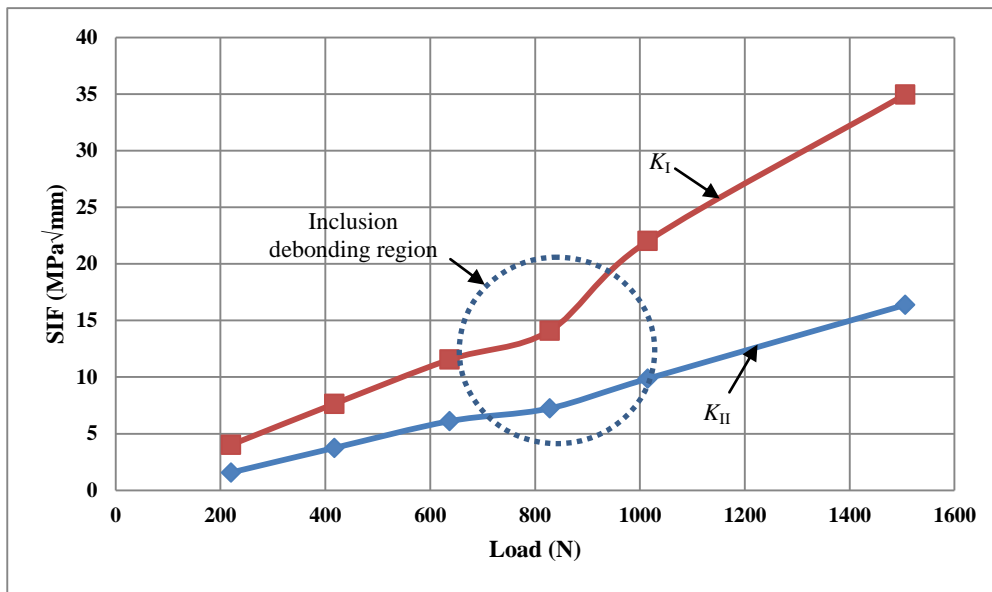


Fig. 3.29 Variation of SIF with load obtained from DIC for ESC with inclusion specimen

Table 3.3 summarizes the values of SIF's obtained using numerical (FEM) and experimental (DIC) method. For SEN with single inclusion specimen, results have compared for load of 399 N. From the Table 3.3, one can observe that there is good agreement of SIF value obtained from FEA and DIC. For edge slant crack with single inclusion specimen, error between FEA and DIC for load 417 N is 7.3 % in  $K_I$  value and 5.55 % for  $K_{II}$ . As well as SIF is evaluated for SEN with two eccentric inclusion specimens for load 659 N. Besides small difference in SIF value (error is 2.48 %) results are in good agreement.

Table 3.3 Comparison of SIF value obtained from FEA and DIC

Configuration	Load (N)	Numerical SIF (MPa√mm)		Experimental SIF (MPa√mm)		% of error between FEA and DIC results	
		$K_I$	$K_{II}$	$K_I$	$K_{II}$	$K_I$	$K_{II}$
SEN with single inclusion	399	10.066	---	10.39	---	3.22	---
ESC with single inclusion	417	7.12	3.96	7.64	4.18	7.3	5.55
SEN with two eccentric inclusion	659	15.69	---	15.30	---	2.48	---

### 3.8.3 Parametric Study

Fig.3.30 shows the SIF variation for different distances between crack tip and edge of the inclusion for SEN with single inclusion specimen. From the graph, it can be observed that SIF is directly proportional to distance between crack tip and edge of the inclusion. As the distance between crack tip and edge of the inclusion increases, the SIF increases. Fig. 3.31 shows the variation for different inclusion diameters. It is evident that SIF is inversely proportional to inclusion diameters. As the inclusion diameter increases, the SIF value decreases.

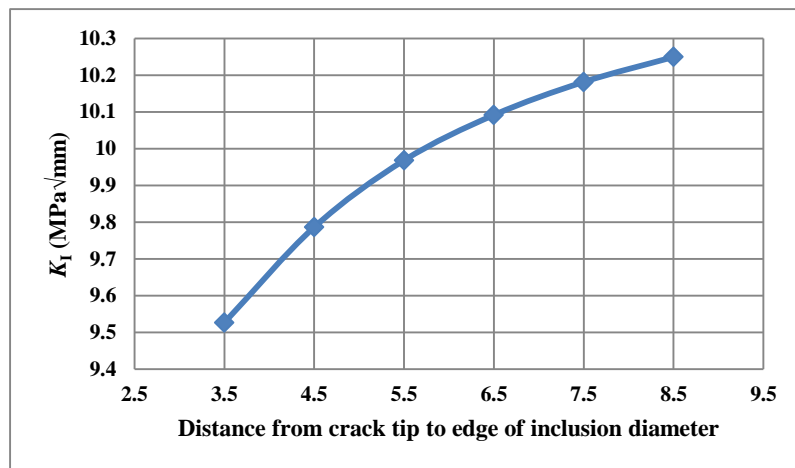


Fig.3.30 Variation of stress intensity factor (S.I.F) with varying distance from crack tip to edge of inclusion diameter (inclusion diameter 6 mm, young's modulus 2.5 GPa and Poisson's ratio 0.35)

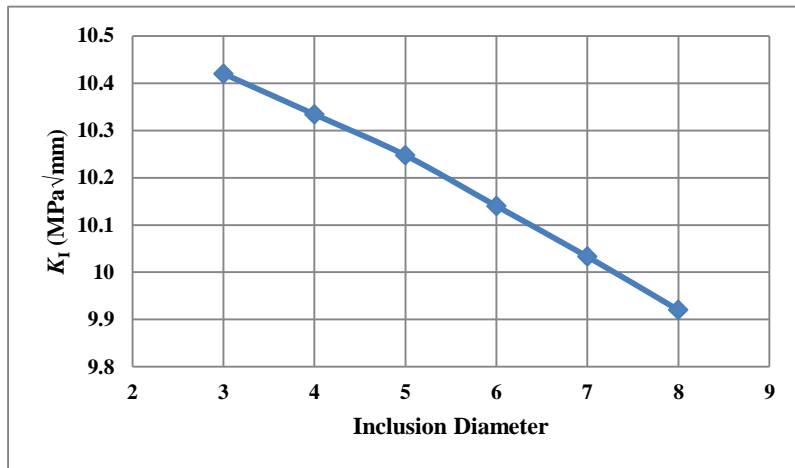


Fig.3.31 Variation of stress intensity factor (S.I.F) with varying inclusion diameter (distance from crack tip to edge of inclusion 6.5 mm, young's modulus 2.5 GPa and Poisson's ratio 0.35)

The variation of SIF with different young's modulus of inclusion is shown in Fig. 3.32. From the plot, it can be observed that with increase in Young's modulus of inclusion SIF is decreases. Also it is observed that, there is significant reduction up to young's modulus of 100 GPa but as compared to other two parameters (distance from crack tip to edge of inclusion and inclusion diameter) effect of young's modulus on SIF value is negligible. Fig.3.33 shows the SIF variation with different Poisson's ratio of inclusion. On careful observation, the inclusion with higher Poisson's ratio reduces SIF value but effect of these on SIF reduction is very less.

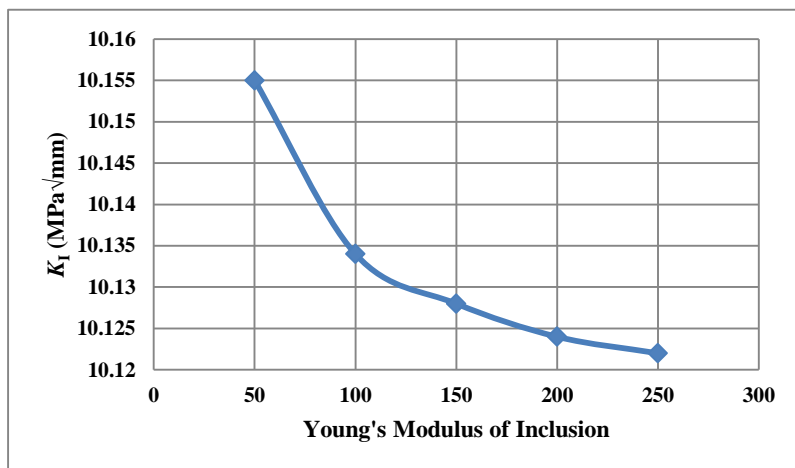


Fig.3.32 Variation of stress intensity factor (S.I.F) with varying Young's modulus of inclusion (inclusion diameter 6 mm and Poisson's ratio 0.35)

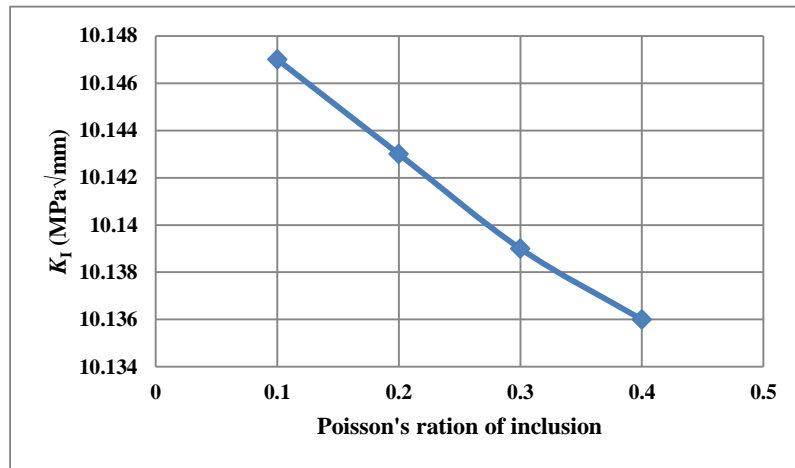


Fig.3.33 Variation of stress intensity factor (S.I.F) with varying Poisson's ratio of inclusion (inclusion diameter 6 mm and young's modulus 2.5 GPa)

### 3.9 Closure

In the present work, an experimental and numerical based study is carried out to estimate the SIF for crack inclusion interaction specimens. SEN, ESC and SEN with two eccentric inclusion (all with circular glass as inclusion) are the three different configurations examined in the present study. The full field technique namely DIC is used to map displacement field around the crack tip. Initially material characterization of epoxy is carried out using DIC technique. Following the characterization, SIF estimation using multi-parameter over-deterministic non-linear approach. The occurrence of debonding between matrix and the inclusion is successfully identified using the experimental technique. A change in SIF is clearly evident at the onset of debonding. Also, the experimentally obtained SIF are found to compare well with the FEA values. Finally, FEA based parametric study is carried out to study the influences of various parameters like inclusion stiffness, it's distance from crack tip. Lower the stiffness of inclusion is, lower is the crack tip SIF as well closer it is lower the SIF. The slight difference (maximum error 7.5 %) between the experimental and numerical results can be due to the difference between the actual crack length used in the experiments and the idealized model of crack used in numerical analysis.

## Chapter 4

# Conclusion and Recommendations for Future Work

In the second chapter, a finite element based study is carried out to understand the mechanics of composite patch repair on damaged CFRP panel of configuration [45/-45/0/90]<sub>s</sub> under tensile load. The influence of various parameters such as patch stacking sequence, patch thickness, overlap length and adhesive thickness is investigated in case of double sided repaired panel. Design value of these parameters is arrived at for a given damaged panel to improve the repair performance using mechanics based approach involving FEA. Also, a GA based approach in-conjunction with finite element analysis is implemented for arriving at an optimized patch dimension and adhesive layer thickness. Experimental study is then carried out with optimized geometry using DIC. The mechanics of double and single sided repair are discussed in detail and strain field from DIC have been compared with finite element estimate and they are found to be in good agreement. In this work, behaviour of adhesive is considered as linear elastic but in actual practice it may be viscoelastic. More study can be done with considering viscoelastic behaviour of an adhesive. Also the work can be extended to study the effect of tapered patch on repair performance.

In the third chapter, experimental and numerical based study is carried out to estimate mixed-mode SIF's for crack inclusion interaction specimens. Initially three different configurations are studied: SEN panel with single inclusion, ESC panel with single inclusion and SEN panel with two inclusions, ahead of the crack tip subjected to tensile load is being studied in the present work. An element stiffness degradation method in-conjunction with maximum radial stress criteria is used in FEA analysis to investigate the effect of debonding on SIF. The finite element model is initially validated using results obtained from DIC technique. They are found to be in good agreement. In the present study, stationary crack is considered for FEA analysis but in actual case crack would grow with increasing load. More study can be done with incrementing the crack along the crack plane with respect to load. Once SIF value is more than or equal to fracture toughness of material then crack has to be propagated. Using this phenomenon more elaborately study can be carried out for same configurations.

# References

- [1] R.M. Jones, *Mechanics of composite materials*, (Taylor and Francis, New York, 1999).
- [2] *The worldwide composite industry structure, Trends and innovations: New release*, JEC Composite, (2010).
- [3] G. Gardiner, *Primary structure repair: the quest of quality, high-performance composite*, Composite world, (2011).
- [4] A. Baker, L.R.F. Rose, R.M. Jones, *Advances in the bonded composite repair of metallic aircraft structure*, (Elsevier Science Ltd, Oxford, 2002).
- [5] <http://www.emeraldinsight.com/journals.htm?articleid=1454782>.
- [6] Q. Wang and N. Wu, A review on Structural enhancement and repair using piezoelectric materials and shape memory alloys, *Smart Material Structures*, 21, (2012).
- [7] Q. Wang, S.T. Quek and K.M. Liew, On the Repair of a cracked beam with a piezoelectric patch, *Smart Material Structures*, 11, (2002).
- [8] C.N. Duong and C.H Wang, *Composite repair – Theory and Design*, (Elsevier, Great Britain, 2007).
- [9] T.V.R.S. Umamaheswar and S. Ripudaman, Modeling of a Patch repair to a thin cracked sheet. *Engineering Fracture Mechanics*, 62, (1999) 267-289.
- [10] O.A. Chukwujekwu, S. Navdeep, U.E. Enemouh and S.V. Rao, Design, analysis and performance of adhesively bonded composite patch repair of cracked aluminum aircraft panels, *Composite Structures*, 71, (2005) 258-270.
- [11] M.L. Pastor, X. Balandraud, M. Grediac and J.L. Robert, on the fatigue response of aluminum specimens reinforced with carbon epoxy patches, *Composite Structures*, 83, (2008) 237-246.
- [12] H. Hosseini-Toudeshky, B. Mohammadi and H.R. Daghyani, Mixed mode fracture analysis of aluminium repaired panels using composite patches, *Composite Sci Technology*, 66, (2006) 188-198.
- [13] M. Ramji and R. Srilakshmi, Design of composite patch reinforcement applied to mixed mode cracked panels using finite element analysis, *Reinforced Plastics and Composites*, 39(9), (2012) 585-595.
- [14] M. Ramji, R. Srilakshmi and M. Bhanu Prakash, Towards optimization of patch shape on the performance of bonded composite repair using FEM, *Composites Part B: Engineering*, 45(1), (2013) 710-720.



- [15] R.A. Scott, H. Yi-Fei, S. George, Springer and L.H. Joo, Compressive strength of CFRP damaged and repaired composite plates, *Composite Materials*, 26(12), (1992) 1796-1825.
- [16] C. Soutis and F.Z. Hu, Design and performance of bonded patch repairs of composite structures, *Proceedings of the Institution of Mechanical Engineers, Part G: J of Aerospace Engg*, 211, (1997) 263-271.
- [17] C. Soutis, D. M. Duan and P. Goutas, Compressive behaviour of CFRP laminates repaired with adhesively bonded external patches, *Composite Structures*, 45(4), (1999) 289-301.
- [18] F.Z. Hu and C. Soutis, Strength prediction of patch-repaired CFRP laminates loaded in compression, *Composite Science and Technology*, 60(7), (2000) 1103-1114.
- [19] R.D.S.G. Campilho, M.F.S.F. de Moura, D.A. Ramantani, J.J.L. Morais and J.J.M.S. Domingues, Tensile behaviour of three-dimensional carbon-epoxy adhesively bonded single and double-strap repairs, *Adhesion & Adhesives*, 29, (2009) 678–686.
- [20] M.Y. Tsai and J. Morton, An investigation into the stresses in double-lap adhesive joints with laminated composite adherends, *Solids and Structures*, 47(24), (2010) 3317–3325.
- [21] J.D. Mathias, X. Balandraud and M. Grediac, Experimental investigation of composite patches with a full-field measurement method, *composites part A: applied science and manufacturing*, 37(2), (2006) 177–190.
- [22] N. Zehnder and P. Ermanni, Optimizing the shape and placement of patches of reinforcement fibers, *Composite Structures*, 77(1), (2007) 1–9.
- [23] C. Pengcheng, G. Xiao-Jing, H. Donald and A. Shahram, Tensile behaviour of patch-repaired CFRP laminates, *Composite Structures*, 93(2), (2011) 582–589.
- [24] M.A. Caminero, S. Pavlopoulou, M. Lopez-Pedrosa, B.G. Nicolaisson, C. Pinna and C. Soutis, Analysis of adhesively bonded repairs in composites: Damage detection and prognosis, *Composite Structures*, 95, (2013) 500-517.
- [25] M. Kashfuddoja and M. Ramji, Experimental investigation of repaired CFRP laminates using 3D-DIC, *Proceedings of 2<sup>nd</sup> International Symposium on Experimental Mechanics*, Taipei, Taiwan (2012).
- [26] M. Kashfuddoja and M. Ramji, Whole-field strain analysis and damage assessment of adhesively bonded patch repair of CFRP laminates using 3D-DIC and FEA, *Composites Part B: Engineering*, 45(1), (2013) 710-720.
- [27] K.J. Callahan and G.E. Weeks, Optimum design of composite laminates using genetic algorithms. *Composites Engineering*, 2(3), (1992) 149-160.

- [28] N.R. Ball, P.M. Sargent and D.O Ige, Genetic algorithm representations for laminate layups, *Artificial Intelligence in Engineering*, 8(2), (1993) 99-108.
- [29] L.R. Riche and R.T. Haftka, Optimization of laminate stacking sequence for buckling load maximization by genetic algorithm, *AIAA Journal*, 31(5), (1993) 951-956.
- [30] K. Sivakumar, N.G.R. Iyengar and K. Debb, Optimization of composite laminates with cutouts using genetic algorithm, variable metric and complex search methods, *Engineering Project Organization Journal*, 32(5), (2000) 635-657.
- [31] J.D. Mathias, X. Balandraud and M. Grediac, Applying a genetic algorithm to the optimization of composite patches, *Computers and Structures*, 84(12), (2006) 823-834.
- [32] F.S. Almeida and A.M. Awruch, Design optimization of composite laminated structures using genetic algorithms and finite element analysis, *Composite Structures*, 88, (2009) 443-454.
- [33] L. Toubal, M. Karama and B. Lorrain, Stress concentration in a circular hole composite plate, *Composite Structures*, 68, (2005) 31-36.
- [34] R.L. Hastie, R. Fredell and J.W. Dally, A photoelastic study of crack repair, *Experimental Mechanics*, 38(1), (1998) 29-36.
- [35] O. Tamate, The effect of a circular inclusion on the stress around a line crack in a sheet under tension, *Fracture Mechanics*, 4, (1968) 257-266.
- [36] C. Atkinson, The interaction between a crack and an inclusion, *Engineering Science*, 10, (1972) 127-136.
- [37] F. Erdogan, G. D. Gupta and M. Ratwani, Interaction between a circular inclusion and an arbitrarily oriented crack, *Applied Mechanics*, 41, (1974) 1007-1013.
- [38] E.E. Gduotos, Interaction effects between a crack and a circular inclusion, *Fibre Science and Technology*, 15(1), (1981) 27-40.
- [39] E.E. Gduotos, Stable Crack Growth of a Crack Interacting with a Circular inclusion, *Theoretical and Applied Fracture Mechanics*, 3(2), (1985) 141-150.
- [40] N. Hasebe, M. Okumura and T. Nakumura, Stress-Analysis of a debonding and a crack Around a Circular Rigid Inclusion, *International Journal of Fracture*, 32(3), (1986) 169-183.
- [41] E.M. Patton and M.H. Santare, The effect of a rigid elliptical inclusion on a straight crack, *International Journal of Fracture*, 46, (1990) 71-79.
- [42] M. Bush, The interaction between a crack and a particle cluster, *International Journal of Fracture*, 88, (1997) 215-232.
- [43] B.J. O'Toole and M.H. Santare, Photoelastic Investigation of Crack-inclusion interaction, *Experimental Mechanics*, 30(3), (1990) 253-257.

- [44] T.C. Easley, K.T. Faber, S.P. Shah, Moiré interferometry analysis of fiber debonding, *Journal of Engineering Mechanics*, 127, (2001) 625-629.
- [45] P.C. Savalia and H.V. Tippur, A study of crack-inclusion interactions and matrix-inclusion debonding using moiré interferometry and finite element method, *Experimental Mechanics*, 47, (2007) 533–547.
- [46] P.C. Savalia, H.V. Tippur and M.S. Kirugulige, A numerical study of inclusion- matrix debonding in the presence of a nearby crack, *Engineering Fracture Mechanics*, 75, (2008) 926-942.
- [47] R.G.R. Prasath and M. Ramji, Study of matrix crack and inclusion interactions using digital photoelasticity and FEA, *Proceedings of 4<sup>th</sup> International Conference on Structural Stability and Dynamics*, Jaipur, India (2012).
- [48] V.V. Veerkar, A study on experimental determination of mixed-mode SIF's using digital photoelasticity and DIC, *Master's Thesis*, IIT Hyderabad, (2012).
- [49] MATLAB R2010a, (MathWorks Inc., Natick, 2000).
- [50] M.A. Sutton, J-J. Orteu and H.W. Schreier, *Image correlation for shape, motion and deformation measurements*, (Springer publishers, New York, 2009).
- [51] Araldite® 2011, *Structural Adhesive*, Technical Data Sheet, Huntsman, (2009).
- [52] D.E. Goldberg, *Genetic algorithms in search, optimization and machine learning*, (Addison-Wesley Publishing, New York, 1989).
- [53] G. Lekhnitskii's, W.S. Tsai and T. Cheron, *Anisotropic plates*, (Gordon and Breach Science Publishers, New York, 1968).
- [54] A. Baker, S. Dutton and D. Kelly, *Composite material for aircraft structures*, (AIAA Publishers, Reston, 2004).
- [55] C. Soutis and F.Z. Hu, Design and performance of bonded patch repairs of composite structures, *Aerospace Engineering*, 211, (1997) 1-9.
- [56] V.R.S. Turanga, Umamaheswarar. and S. Ripudaman, Modelling of a patch repair to a thin cracked sheet, *Engineering Fracture Mechanics*, 62, (1999) 267:289.
- [57] S. Yoneyama, Y. Morimoto and M. Takashi, Automatic Evaluation of Mixed-mode Stress Intensity Factors Utilizing Digital Image Correlation, *Strain*, 42, (2006) 21–29.
- [58] S. Yoneyama, T. Ogawa and Y. Kobayashi, Evaluating mixed-mode stress intensity factors from full-field displacement fields obtained by optical methods, *Engineering Fracture Mechanics*, 74(9), (2007) 1399-1412.
- [59] Standard test method for tensile properties of plastics. ASTM D638.
- [60] P. Kumar, *Elements of fracture mechanics*, (Tata McGraw-Hill, New Delhi, 2009).

# List of Papers Submitted on the Basis of This Thesis

1. Vishwajeet S. Bhise, Mohammad Kashfuddoja and M. Ramji, Optimization of circular composite patch reinforcement on damaged CFRP laminate involving both mechanics based and genetic algorithm in-conjunction with 3D FEA, Journal of Composite Materials, (Accepted for publication).
2. Vishwajeet S Bhise and Ramji M, Optimization of Composite Patch Reinforcement to Damaged CFRP Laminates: A Numerical and Experimental Investigation, International Conference on Advancements in Polymeric Materials (APM 2013), March 1-3, Lucknow, India, 2013.
3. Vishwajeet S. Bhise, Mohammad Kashfuddoja, C.P.Vyasarayani and M. Ramji, Optimization of Composite Patch Reinforcement to Damaged CFRP Laminates, 4th International Congress on Computational Mechanics and Simulation (ICCMS 2012), December 9-12, Hyderabad, India, 2012.